International Journal of Dentistry

Advanced Digital Dentistry

Lead Guest Editor: Vahid Rakhshan
Guest Editors: Chiarella Sforza, Predrag Vucinic, Anca M. Vitalariu, and Márcio De Menezes

Advanced Digital Dentistry

International Journal of Dentistry

Advanced Digital Dentistry

Lead Guest Editor: Vahid Rakhshan
Guest Editors: Chiarella Sforza, Predrag Vucinic, Anca M. Vitalariu, and Márcio De Menezes

Editorial Board

Contents

Hindawi
International Journal of Dentistry
Volume 2018, Article ID 7540954, 2 pages
https://doi.org/10.1155/2018/7540954

Editorial

Advanced Digital Dentistry

Vahid Rakhshan,[1,2] **Chiarella Sforza**,[3] **Predrag Vucinic**,[4] **Anca M. Vitalariu**,[5] **and Márcio De Menezes**[6]

[1]*Department of Cognitive Neuroscience, Institute for Cognitive Science Studies, Tehran, Iran*
[2]*Department of Dental Anatomy, Faculty of Dentistry, Islamic Azad University, Tehran, Iran*
[3]*Department of Biomedical Sciences for Health, Università degli Studi di Milano, Milano, Italy*
[4]*Department of Orthodontics, Clinic of Dentistry, Faculty of Medicine, University of Novi Sad, Novi Sad, Serbia*
[5]*Department of Implantology, Removable Restorations and Technology, Universitatea de Medicina si Farmacie Grigore T. Popa Iasi, Iaşi, Romania*
[6]*Department of Operative Dentistry, School of Health Sciences, State University of Amazonas, Manaus, Brazil*

Correspondence should be addressed to Vahid Rakhshan; vahid.rakhshan@gmail.com

Received 12 November 2018; Accepted 15 November 2018; Published 26 December 2018

Advanced digital technology is rapidly changing the world, as well as transforming the dental profession. The adoption of digital technologies in dentistry allied with efficient processes, and accurate high-strength materials are replacing outdated techniques to improve overall patients' experiences and outcomes. A variety of digital devices such as laser scanners, holography, intraoral and face scanners, cone beam computed tomography (CBCT), software for computer-assisted design/computer-assisted manufacturing (CAD/CAM), and 3D printing provide new potential alternatives to replace the manual tasks and improve the quality of care and patient experiences. This technology has several advantages, including accurate measurements, storage, and time-saving as well as online consultation and presentation, providing information exchange with different centers for planning and appraising medical procedures and treatments. Even teaching and research tools greatly benefited from these innovations, with software for teaching dentistry (such as 3D software for learning anatomy or 3D simulation programs for surgical procedures), digital archiving of patient records and convenient/rapid sharing of them over the Internet, digital bibliographic assistance in dental research, or other utilities.

This special issue is a representative sampling of this literature on the use of digital technologies in dentistry. With the generous support of the respective editors, these papers cover an intentionally broad range of topics that include investigations of intraoral scanning accuracy, CBCT technology, 3D accuracy of digital impressions, 3D finite element models, and applications to orthodontics. Out of 25 manuscripts received in this issue, six were published: both technical aspects dealing with digital impressions ("Three-Dimensional Accuracy of Digital Impression versus Conventional Method: Effect of Implant Angulation and Connection Type" by M. Alikhasi et al. and "Trueness and Precision of Three-Dimensional Digitizing Intraoral Devices" by H. Mutwalli et al.) and imaging techniques ("Assessing the Correlation between Skeletal and Corresponding Soft-Tissue Equivalents to Determine the Relationship between CBCT Skeletal/Dental Dimensions and 3D Radiographic Soft-Tissue Equivalents" by D. I. Kim and M. O. Lagravere and "Accuracy of Periapical Radiography and CBCT in Endodontic Evaluation" by R. L. Giudice et al.) had been investigated. All these papers employed novel technologies to help answering clinical questions that may dictate different treatment plans.

Additionally, finite element studies ("Development and Validation of 3D Finite Element Models for Prediction of Orthodontic Tooth Movement" by U. Likitmongkolsakul et al.) and longitudinal assessments ("Three-Dimensional Changes of the Auditory Canal in a Three-Year Period during Adolescence Using CBCTs" by A. Woods and M. O. Lagravere) during growth and development have been performed. In both investigations, proper instruments and

software were employed to offer quantitative information to the clinicians.

In synthesis, this special issue wants to give some examples of the current solutions that technology offers to dental practitioners and provide the bases for future investigations bringing essential ingredients for patient care, dental research, education, and daily practice.

Conflicts of Interest

The editors declare that they have no conflicts of interest.

Vahid Rakhshan
Chiarella Sforza
Predrag Vucinic
Anca M. Vitalariu
Márcio De Menezes

Hindawi
International Journal of Dentistry
Volume 2018, Article ID 5189761, 10 pages
https://doi.org/10.1155/2018/5189761

Research Article

Trueness and Precision of Three-Dimensional Digitizing Intraoral Devices

Hussam Mutwalli,[1] **Michael Braian**,[1] **Deyar Mahmood**,[1] **and Christel Larsson**[2]

[1]*Department of Prosthodontics, Faculty of Odontology, Malmö University, Smedjegatan 16, 214 21 Malmö, Sweden*
[2]*Department of Materials Science and Technology, Faculty of Odontology, Malmö University, Smedjegatan 16, 214 21 Malmö, Sweden*

Correspondence should be addressed to Hussam Mutwalli; dr.mutwalli@gmail.com

Received 13 June 2018; Revised 25 September 2018; Accepted 30 October 2018; Published 26 November 2018

Guest Editor: Vahid Rakhshan

Aim. To measure the trueness and precision under repeatable conditions for different intraoral scanners (IOSs) when scanning fully edentulous arch with multiple implants. *Materials and Methods*. Three IOSs and one industrial scanner were used to scan one edentulous master cast containing five implant scan bodies and three spheres. The cast was scanned thirty times with each scanner device. All scans were analyzed in the inspect software, and three-dimensional locations of the implants and the interarch distance between the spheres were measured. The values were compared to measurements made with one coordinate measuring machine (true value). One-way ANOVA was used to calculate the differences between IOSs and in comparison with the true value. *Results*. Significant differences were found between all IOSs. For the implant measurements, Trios 3 had the lowest trueness (≤114 μm), followed by Trios 3 mono (≤63 μm) and Itero element (≤−41 μm). Trios had the lowest precision (≤135 μm), followed by Itero element (≤101 μm) and Trios 3 mono (≤100 μm). With regard to the interarch distance measurements, Trios 3 had the lowest trueness (≤68 μm), followed by Trios 3 mono (≤45 μm) and Itero element (≤40 μm). Trios 3 had the lowest precision (≤206 μm), followed by Itero element (≤124 μm) and Trios 3 mono (≤111 μm). *Conclusion*. The results from this in vitro study suggest that precision is low for the tested IOS devices when scanning fully edentulous arches with multiple implants.

1. Introduction

One of the most recent techniques introduced to dentistry is the ability to digitize the oral cavity and create a three-dimensional virtual model; this device is known as an intraoral scanner (IOS). The first appearance of the IOS was in 1980. Few years later, a Swiss dentist and an Italian electrical engineer developed and introduced CEREC by Sirona Dental Systems in 1987 [1]. Over the past few years, several commercial IOS systems have been introduced to the market. Preferably, the IOS device should have high trueness and high precision. Both trueness and precision describe the accuracy of the specific digital device (ISO 12836:2015) [2]. High trueness means that the device provides a result that is close to or equal to the true dimension of the object being scanned. A device with higher precision has more repeatable and consistent scans or measurements. This is however not always achieved in all scanners at all clinical conditions. Several studies have shown that IOS devices have difficulty in scanning full dental arch or edentulous arch with multiple implants and generating accurate virtual models [3–8]. The sources that could generate errors are scanning software process, oral environment, scanning protocol, and user's experience. The main reason for enhanced errors on longer span scans could be the scanning method found in most IOS devices. The scanners acquire single images that are stitched with other images to produce a virtual 3D model of the object being scanned. The technique is referred to as stitching; software process known as the best fit algorithm, can introduce errors into large scan distance such as the full-arch situation [6, 9, 10]. To achieve a proper stitching, the scanned object needs a suitable structure. Typically, occlusal

surfaces on molars and premolars present structures with many anatomical geometries making these areas simpler to stitch compared to edentulous areas or the incisal edge of the mandibular front teeth [11]. The oral environment contains saliva, blood, and artificial reflective surfaces in the oral cavity that can introduce errors during the digitizing process [12]. The scanning protocol refers to the scanning path for digitizing the object. A study reported that an accurate scanning strategy minimizes the inaccuracies in the digital fabrication workflow and creates precise virtual 3D datasets [13]. Therefore, it is crucial to apply the right scanning path in order to obtain a usable virtual 3D model [14]. In addition to the scanning protocol, the learning curve or user's scanning skill has an impact on generating accurate virtual models. Studies report that experienced operators can perform better scans than nonexperienced operators [9, 10]. After scanning, restorations are designed in computer-aided software and then milled or additively manufactured from materials ranging from polymers to monolithic ceramics. In order to control errors in this digital workflow, it is important to study each process in the production.

The current study focused on assessing the trueness and precision of three different intraoral scanners on the scanning edentulous jaw with multiple implants. Two terms are central to understanding metrology: accuracy and precision. Accuracy relates to the closeness of a measured value to a standard or a known (true) value, whereas precision pertains to the closeness of measured values to each other. Figure 1 illustrates the correlation between these two terms; if the center of the target would be referred to as the true value or the standard, then Figure 1(a) shows a result that has both low accuracy and precision. In contrast, Figure 1(d) illustrates results that are both accurate and precise. When conducting research, it is normal to calculate the standard deviation (SD) and the mean value of a measurement (mean). Relating these two terms to the metrological nomenclature would correlate the mean value as accuracy and the standard deviation to precision. The authors have utilized the recently updated recommendation from the International Organization for Standardization (Dentistry—Digitizing devices for CAD/CAM systems for indirect dental restorations—Test methods for assessing accuracy, ISO 12836:2015) as reference for describing the terms accuracy, trueness, and precision [2]. ISO 12836:2015 uses two terms to describe accuracy; the first is precision and the second is trueness. Trueness is closeness of agreement between the mean obtained from repeated measurements and a true value. If ISO 12836:2015 is used as reference, then all accuracy legends in Figure 1 would change to trueness, and Figure 1(d) would be regarded as accurate and Figure 1(a) as not accurate; meanwhile, Figure 1(b) would be described as having a low trueness; the shooter is precise but not accurate. Precision is the closeness between the independent results of measurement obtained under specific conditions. Precision is divided into two different groups: in the first group, the subject is tested in the same way by the same operator and measuring equipment under the same conditions. This first version of precision tests repeatability. The first version was tested in this current study. According to ISO, the measurement should be repeated thirty times under the same condition to assess the precision under repeatable condition. The precision would be obtained by calculating the standard deviation of the thirty measurements. In the second version of precision, the conditions change. Thus, this part tests reproducibility.

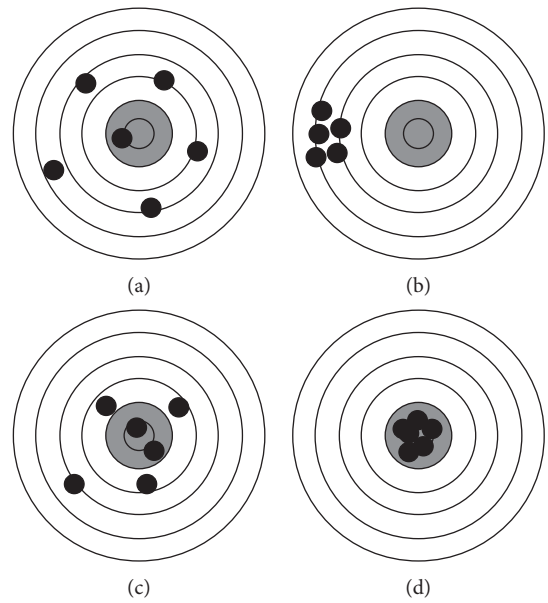

Figure 1: Illustration of the correlation between accuracy and precision. (a) Low accuracy, low precision. (b) Low accuracy, high precision. (c) High accuracy, low precision. (d) High accuracy, high precision.

Different methods have been developed by researchers to assess the trueness and precision of IOS devices. Some of these studies have either compared the IOS device to the conventional impression technique or to other IOS devices [6–8, 15, 16]. Almost all of the researchers employed a master cast that has been measured either by tactile computer metric measurements (CMM) or by using an industrial optical scanner to obtain reference data as a virtual 3D file. The master cast is then scanned by the test scanners, obtaining virtual models. The virtual models are measured and compared to the reference date. Some studies employed the best fit alignment method to assess full-arch scans with teeth or implants [4, 7, 8, 16]. The method presents a color map data with threshold colors to visualize and measure differences between two scans. The current study used a different method: here, five cylinders (scan bodies) and three spheres were used as landmarks, making it possible to calculate only eight points in the scan, instead of comparing thousands of points from the scan data. The aim of this present study was to measure the trueness and precision under repeatable condition of different intraoral scanner devices on scanning a fully edentulous arch with multiple implants. The null hypothesis was that there would be no significant differences between the intraoral scanner devices in comparison with the true value (coordinate measuring machine).

2. Materials and Methods

2.1. Master Model. A cast of an edentulous maxilla with five implants (Brånemark system Mk IV TiUnite WP 5 × 10 mm). Five implant scan bodies (Elos Accurate Intraoral Brånemark WP 6A-C, Elos Medtech Pinol A/S, Gørløse, Denmark) were connected to the implants. The scan bodies were manufactured from polyether ether ketone (PEEK). The core structure of the model consisted of tungsten metal, and the edentulous areas were made by using dental stone material. The implants were placed in a nonparallel position in order to mimic the clinical situation. The implants were positioned in the area of the lateral incisor, canines, and second premolars, according to positions 1–5, as illustrated in Figure 2. Three spheres were used as fixed reference landmarks; the placement is shown in Figure 2.

2.2. Coordinate Measuring Machine (CMM). The master model was measured by a certified metrologic center (Elos Medtech Pinol A/S, Gørløse, Denmark) to obtain three-dimensional data of the master model components (Figure 3). A certified industrial coordinate measuring machine, CMM (Carl Zeiss Industrielle Messtechnik GmbH) was used with its corresponding software (Calypso 2015, Service Pack 3, Version 6.0.12). The master model was measured one time with the CMM using a high touch signal probe with a 1 mm ruby sphere (in three dimensions: x, y, and z axes). The accuracy of the CMM was certified by the national entity of accreditation with a maximum permissible error of length measurement of $1.9 \pm 3\,\mu m/1{,}000\,\mu m$ according to the appropriate standard published by the International Organization for Standardization [17]. The circumference of each scan bodies was measured to define its center point in the x, y, and z axes. Furthermore, the interarch distance between the center of spheres was determined. The CMM measurement was regarded as a true value in the present study.

2.3. GOM Optical 3D Metrology. The master model was sent to the manufacturer center (Kulzer GmbH Nordic AB, Helsingborg, Sweden) to scan the master model thirty times with an optical industrial blue light scanner (Atos core, GmbH Optical Metrology, Braunschweig, Germany) (Figure 3). The system technology of this optical scanner is based on emitting different light fringe patterns onto the model, while the reflected lights are recorded by means of two high-resolution video cameras. Atos scanner was used in this study as a reference scanner for comparison with IOS devices.

2.4. Intraoral Scanner Systems. Three different IOS systems were evaluated: Trios 3 and Trios 3 mono (3shape, Copenhagen, Denmark) and Itero (Align technology Inc., California, USA) (Table 1). The master model was scanned 30 times with each tested scanner device, resulting in 90 virtual 3D models in total (Figure 3). To reduce the risk of operator bias and different levels of operating experience

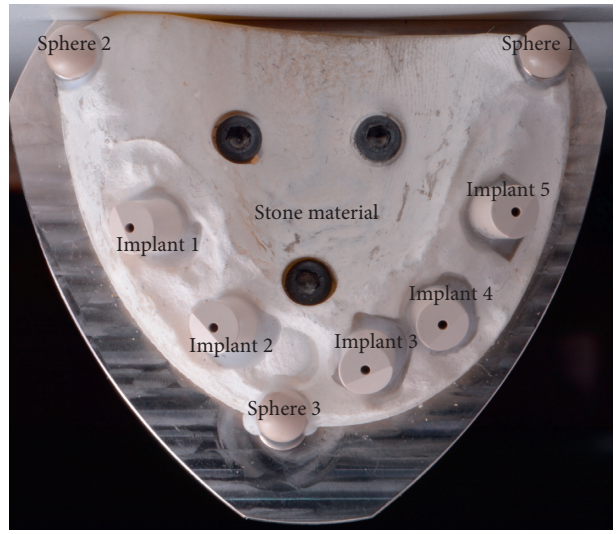

Figure 2: Master model.

that could influence the results, it was decided that all scanning procedures would be made by one dentist who was experienced and familiar with the three IOS systems. The calibration of all IOS systems was performed according to the manufacturer's recommendations in order to mimic the clinical situation.

2.4.1. Trios 3 Scanner. The Trios 3 scanner is based on confocal microscopy technology. The system has color software, and powder application is not required. Trios 3 is cabled (pod). The master model was scanned 30 times on the same day with approximately 10 to 15 minutes between each scan. The scanning procedure started first from the buccal surface of the right sphere (sphere 3), moving along the buccal surface toward the left sphere (sphere 1), and returning from the occlusal-palatal side of sphere 1. This technique was called buccal, occlusal, and palatal scanning strategy (BOP).

2.4.2. Trios 3 Mono Scanner. Trios 3 mono has the same features as Trios 3, except for its inability to register color. Trios 3 mono is cabled (pod). Trios 3 mono was utilized to repeatedly scan the master model 30 times on the same day with approximately 10 to 15 minutes between the scans. This was followed by a similar scanning strategy (BOP) to scan the master model.

2.4.3. Itero Element Scanner. The Itero element device is a powder-free system with color scan features. The Itero technology is based on parallel confocal microscopy to capture several images per second. In order to evaluate the repeatability of the Itero device, the master model was scanned 30 times during the same session with approximately 10 to 15 minutes between each scan. The scanning strategy for the Itero group was performed by zigzag movement from sphere 3 to sphere 1 (buccal to occlusal to palatal), all in one direction and without returning to the starting point. This

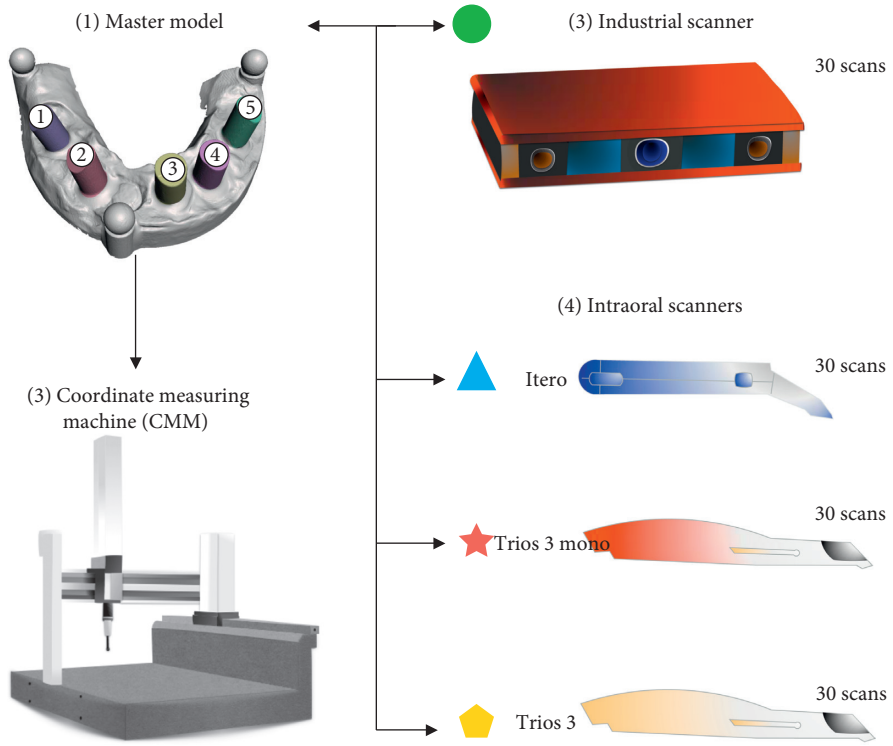

Figure 3: Study workflows. (1) Master model. (2) CMM measured the master model to obtain a true value. (3) Industrial Atos scanner digitized the master model 30 times. (4) Each intraoral scanner device (Trios 3, Trios 3 mono, and Itero) digitized the master model 30 times.

Table 1: Information about the intraoral scanner systems.

System	Manufacturer	Software	Scanning technology	Scan protocol	Acquisition	Powder application	Export
Trios 3	3shape	1.4.5.1	Conofocal microscopy	BOP	Video sequence	No	STL
Trios 3 mono	3shape	1.4.6.4	Conofocal microscopy	BOP	Video sequence	No	STL
Itero element	Cadent Inc.	1.4.0.318	Conofocal microscopy	Zig-zag	Video sequence	No	STL

B = buccal; O = occlusal; P = palatal.

strategy was chosen on account of fact that the Itero scanner tip is larger in width than the other dental scanner; therefore, it was almost impossible to scan the mesial and distal surface properly without rotating the camera tip.

2.5. Alignment and Measurement Procedures. A total of 120 scans were generated from the Atos and three IOS systems (30 virtual 3D models of the Atos and 30 virtual 3D models of each intraoral scanner). All 3D models were converted to standard tessellation language (STL) file format. Subsequently, each virtual 3D model was individually imported and measured once in a reverse engineering software program (GOM inspect software 2016, Rev. 95488). All scans were measured in the exact same way. The initial set after the virtual model had been imported into the software was the construction of the fitting element of the three spheres and then aligned the 3D model into the same x, y, and z CMM coordinate position (Figure 4(a)). Sphere 1 was used as anchorage or reference point. The linear distances between the center point of sphere 1 to sphere 2 (D1_D2), sphere 1 to sphere 3 (D1_D3), and sphere 2 to sphere 3 (D2_D3) were constructed and measured (Figure 4(b)). The distance between the spheres described the interarch distance between the posterior right, left, and anterior quadrants of the 3D model.

In order to measure the position and direction of all implants to reference sphere 1, the center point of each implant was located. Figure 4(c) illustrates the construction of fitting cylinders and fitting planes. The best Gaussian fit was utilized as the fitting algorithm for the cylinders and planes. The center point of each implant was installed by constructing the intersecting point between cylinders and planes (Figure 4(d)). The center point of each implant was measured in the x, y, and z axes of the space. The z-axis represented the vertical direction of each implant. The x and y axes described the horizontal orientation of each implant.

2.6. Measurement Parameters. The measurement of each virtual 3D model consisted of the five implant center points in the x, y, and z axes, and three linear distances between the center of the spheres. One virtual 3D model was divided into a total of 18 parameters. Each scanner system resulted in 540 parameters. In total, 2160 measurement parameters were a result from the Atos and the three dental scanner groups. All measurements of the 3D models were conducted by one operator.

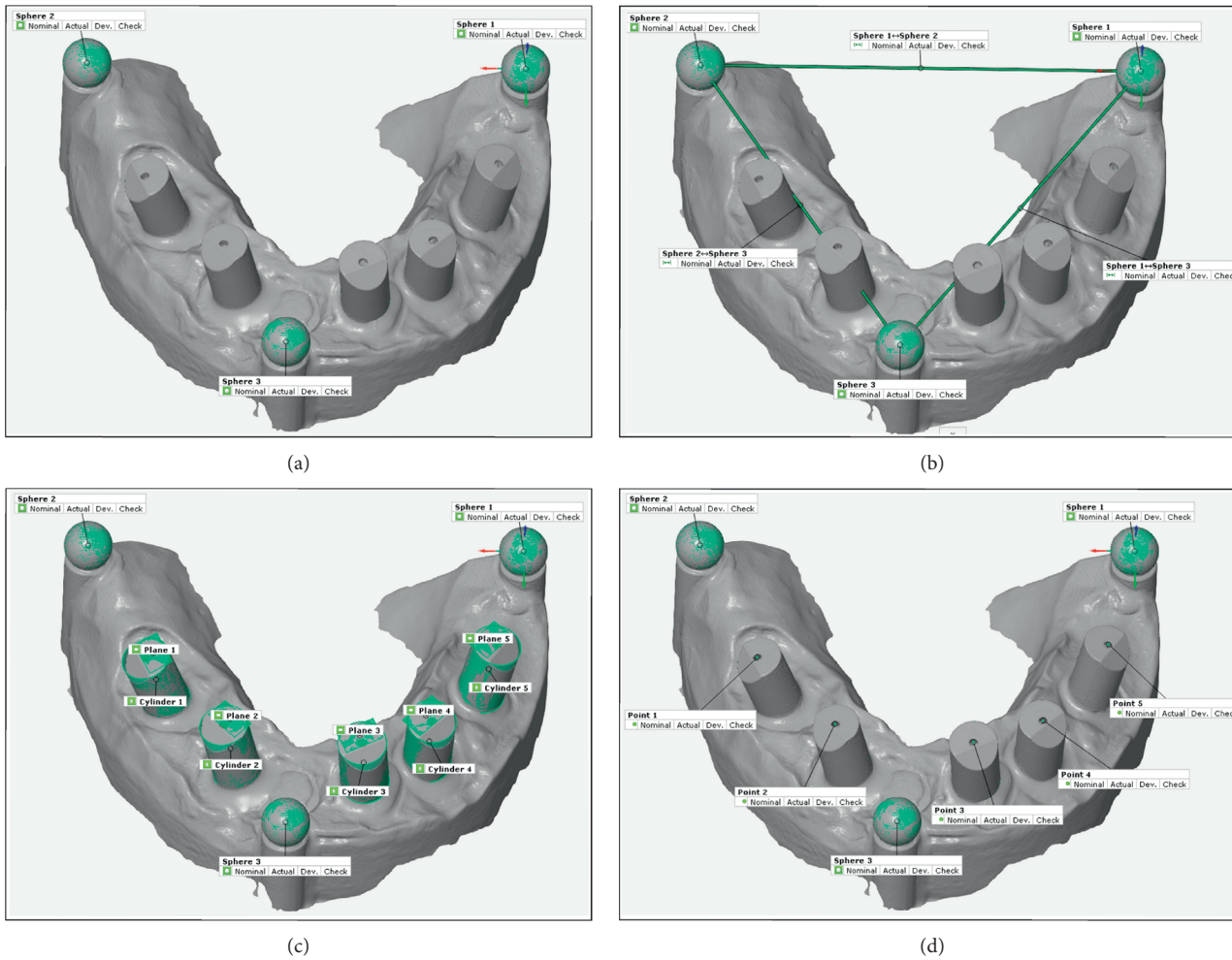

Figure 4: Four different measurement procedures. (a) Construction of the spheres and alignment of 3D model in the same CMM coordinate position. (b) Linear distances in between the center of the spheres. (c) Construction of planes and cylinders for all implants. (d) Installation of the center points of all implants.

2.7. Datasets and Statistical Analysis. The measurement datasets were exported to SPSS (IBM SPSS Statistics version 25) where calculations for mean, 95% confidence interval, standard deviation (precision) of all scanners, and the difference between the mean values of all scanners and the true value (trueness) were made. The Shapiro–Wilks test was used to examine the normal distribution. One-way ANOVA was carried out to test for the hypothesis ($P < 0.05$). Furthermore, the post hoc test using least significant difference (LSD) was carried out to identify difference in implants and interarch distance between two specific intraoral scanners at 0.05 significant level.

3. Results

In this study, normal distribution was found by Shapiro–Wilks test in all intraoral scanners except the Atos scanner. A summary of results of all measurements for precision, trueness, mean, and 95% confidence interval per group is presented in Tables 2–5 and Figure 5. The trueness displayed positive and negative values, depending on whether the mean for Trios 3, Trios 3 mono, Itero element, and Atos were above or below the true value.

3.1. Trueness of Dental Scanners and Atos Scanner

3.1.1. Trios 3. In the *y*-axis, Trios 3 showed least trueness when compared to the CMM value at ≤114 μm. In the *z*-axis, it had the highest deviation when compared to the CMM dimension at ≤76 μm. In the *x*-axis, it showed a trueness of ≤45 μm. With regard to interarch distance, D1_3 showed the highest deviation in comparison with true dimension at 68 μm.

3.1.2. Trios 3 Mono. In the *y*-axis, Trios 3 mono showed an overall trueness of ≤27 μm for all implants. In the *z*-axis, Trios 3 mono showed trueness when compared to the CMM dimension at ≤63 μm. In the *x*-axis, Trios 3 mono displayed trueness at ≤47 μm. The interarch measurements displayed an overall deviation of ≤45 μm.

3.1.3. Itero Element. In the *y*-axis, Itero presented trueness at ≤−41 μm. In the *z*-axis, Itero showed an overall trueness of ≤25 μm for all implants when compared to the CMM value. In the *x*-axis, Itero displayed deviation at ≤37 μm.

Table 2: Results of precision and trueness of all implants and interarch distances.

Parameters (mm)	n	Atos		Trios 3		Trios 3 mono		Itero elements	
		Precision	Trueness	Precision	Trueness	Precision	Trueness	Precision	Trueness
Implant 1 X	30	0.009	−0.001	0.135	0.042	0.100	−0.009	0.101	0.037
Implant 1 Y	30	0.004	−0.004	0.073	0.079	0.023	0.016	0.038	−0.034
Implant 1 Z	30	0.002	0.000	0.047	0.063	0.025	−0.006	0.040	0.025
Implant 2 X	30	0.018	0.000	0.127	0.054	0.095	−0.014	0.083	0.032
Implant 2 Y	30	0.006	−0.004	0.094	0.095	0.027	0.018	0.044	−0.041
Implant 2 Z	30	0.002	0.000	0.035	0.076	0.024	−0.003	0.029	0.015
Implant 3 X	30	0.014	−0.001	0.133	−0.047	0.097	0.015	0.081	0.032
Implant 3 Y	30	0.014	−0.007	0.097	0.114	0.033	−0.025	0.041	−0.025
Implant 3 Z	30	0.007	0.002	0.033	0.046	0.019	−0.025	0.025	0.021
Implant 4 X	30	0.016	0.000	0.129	−0.029	0.082	0.015	0.075	0.028
Implant 4 Y	30	0.019	−0.003	0.077	0.066	0.029	−0.027	0.034	−0.007
Implant 4 Z	30	0.008	0.001	0.049	0.031	0.027	0.056	0.039	0.015
Implant 5 X	30	0.018	−0.002	0.099	−0.018	0.059	0.047	0.055	0.010
Implant 5 Y	30	0.014	−0.008	0.039	0.018	0.026	−0.025	0.026	−0.012
Implant 5 Z	30	0.018	0.003	0.063	0.035	0.028	0.063	0.033	0.025
D1_D2	30	0.005	−0.003	0.206	0.003	0.111	−0.034	0.124	0.040
D1_D3	30	0.011	−0.001	0.046	0.068	0.052	−0.017	0.028	−0.009
D2_D3	30	0.026	−0.002	0.061	0.014	0.022	0.045	0.040	−0.033

n = number of scans; mm = millimeter; *n* = number; D1_D2 = distance from sphere 1 to sphere 2; D1_D3 = distance from sphere 1 to sphere 3; D2_D3 = distance from sphere 2 to sphere 3.

Table 3: Results of mean and 95% confidence interval for the mean of all implants and interarch distances.

Parameters (mm)	n	Atos			Trios 3			Trios 3 Mono			Itero elements		
			95% confidence interval for mean			95% confidence interval for mean			95% confidence interval for mean			95% confidence interval for mean	
		Mean	Lower bound	Upper bound	Mean	Lower bound	Upper bound	Mean	Lower bound	Upper bound	Mean	Lower bound	Upper bound
Implant 1 X	30	47.016	47.013	47.020	47.060	47.010	47.111	47.009	46.972	47.046	47.055	47.017	47.093
Implant 1 Y	30	19.870	19.869	19.872	19.953	19.926	19.980	19.891	19.882	19.899	19.840	19.826	19.854
Implant 1 Z	30	4.361	4.360	4.362	4.424	4.407	4.442	4.356	4.347	4.365	4.386	4.371	4.401
Implant 2 X	30	37.597	37.590	37.604	37.652	37.604	37.699	37.583	37.548	37.619	37.629	37.598	37.660
Implant 2 Y	30	31.030	31.028	31.032	31.129	31.093	31.164	31.052	31.042	31.063	30.993	30.977	31.009
Implant 2 Z	30	6.147	6.146	6.148	6.223	6.210	6.236	6.144	6.135	6.153	6.162	6.152	6.173
Implant 3 X	30	20.618	20.613	20.623	20.571	20.521	20.621	20.633	20.597	20.669	20.650	20.620	20.681
Implant 3 Y	30	35.667	35.662	35.672	35.788	35.752	35.824	35.649	35.637	35.661	35.649	35.634	35.664
Implant 3 Z	30	9.087	9.085	9.090	9.131	9.119	9.143	9.115	9.108	9.122	9.106	9.097	9.116
Implant 4 X	30	11.911	11.906	11.917	11.883	11.835	11.931	11.927	11.896	11.957	11.940	11.912	11.968
Implant 4 Y	30	30.751	30.743	30.758	30.820	30.791	30.849	30.727	30.716	30.738	30.747	30.734	30.759
Implant 4 Z	30	6.903	6.900	6.907	6.934	6.916	6.952	6.958	6.948	6.968	6.918	6.903	6.932
Implant 5 X	30	3.633	3.627	3.640	3.617	3.580	3.654	3.682	3.660	3.704	3.645	3.625	3.665
Implant 5 Y	30	18.106	18.101	18.112	18.133	18.118	18.147	18.090	18.080	18.099	18.103	18.093	18.113
Implant 5 Z	30	5.535	5.528	5.542	5.567	5.544	5.590	5.596	5.585	5.606	5.558	5.545	5.570
D1_D2	30	53.687	53.685	53.688	53.692	53.615	53.769	53.655	53.614	53.697	53.729	53.682	53.775
D1_D3	30	50.923	50.919	50.928	50.990	50.975	51.009	50.908	50.888	50.927	50.915	50.905	50.926
D2_D3	30	47.608	47.599	47.618	47.624	47.601	47.647	47.655	47.647	47.663	47.578	47.563	47.592

mm = millimeter; *n* = number; D1_D2 = distance from sphere 1 to sphere 2; D1_D3 = distance from sphere 1 to sphere 3; D2_D3 = distance from sphere 2 to sphere 3.

The interarch measurements displayed an overall deviation of ≤40 μm.

3.1.4. Atos Scanner. In the *y*-axis, it also showed highest trueness at ≤−8 μm for all implants. In the *z*-axis, the Atos scanner displayed highest trueness at ≤3 μm for all implants when compared to the true value. In the *x*-axis, it had highest trueness at ≤−2 μm. The interarch measurements for Atos showed highest trueness of ≤−3 μm.

3.2. Precision of Dental Scanners and Atos Scanner

3.2.1. Trios 3. In the *x*-axis, Trios 3 had lowest precisions of ≤135 μm and for the *y*-axis at ≤90 μm. In the *z*-axis, Trios 3 showed a precision of ≤61 μm. In the interarch measurements,

Table 4: The results of one-way ANOVA between all groups in comparison with the true value for implants and interarch distances.

	ANOVA				
	Sum of squares	df	Mean square	F	Sig.
Implant 1 X	0.062	4	0.016	1.614	0.175
Implant 1 Y	0.206	4	0.051	28.215	0.000
Implant 1 Z	0.088	4	0.022	19.774	0.000
Implant 2 X	0.086	4	0.021	2.654	0.037
Implant 2 Y	0.294	4	0.074	25.429	0.000
Implant 2 Z	0.122	4	0.030	46.979	0.000
Implant 3 X	0.104	4	0.026	3.057	0.020
Implant 3 Y	0.404	4	0.101	32.890	0.000
Implant 3 Z	0.030	4	0.008	14.418	0.000
Implant 4 X	0.053	4	0.013	1.827	0.128
Implant 4 Y	0.149	4	0.037	17.883	0.000
Implant 4 Z	0.051	4	0.013	10.865	0.000
Implant 5 X	0.069	4	0.017	4.176	0.003
Implant 5 Y	0.029	4	0.007	9.501	0.000
Implant 5 Z	0.058	4	0.014	9.420	0.000
D1_D2	0.081	4	0.020	1.160	0.332
D1_D3	0.135	4	0.034	23.715	0.000
D2_D3	0.094	4	0.024	14.637	0.000

D1_D2 = distance from sphere 1 to sphere 2; D1_D3 = distance from sphere 1 to sphere 3; D2_D3 = distance from sphere 2 to sphere 3; df = degree of freedom; F = analysis of variance; Sig. = significant.

Table 5: The result of post hoc test between the intraoral scanners in implants and interarch distances.

	Trios 3 vs. mono Sig.	Trios 3 vs. Itero Sig.	Mono vs. Itero Sig.
Implant 1 X	0.045	0.841	0.071
Implant 1 Y	0.000	0.000	0.000
Implant 1 Z	0.000	0.000	0.001
Implant 2 X	0.004	0.334	0.052
Implant 2 Y	0.000	0.000	0.000
Implant 2 Z	0.000	0.000	0.006
Implant 3 X	0.011	0.001	0.467
Implant 3 Y	0.000	0.000	0.991
Implant 3 Z	0.007	0.000	0.154
Implant 4 X	0.052	0.011	0.548
Implant 4 Y	0.000	0.000	0.096
Implant 4 Z	0.006	0.069	0.000
Implant 5 X	0.000	0.069	0.027
Implant 5 Y	0.000	0000	0.068
Implant 5 Z	0.005	0.364	0.000
D1_D2	0.282	0.29	0.034
D1_D3	0.000	0.000	0.439
D2_D3	0.003	0.000	0.000

D1_D2 = distance from sphere 1 to sphere 2; D1_D3 = distance from sphere 1 to sphere 3; D2_D3 = distance from sphere 2 to sphere 3; vs. = versus; mono = Trios 3 mono; Sig. = significant.

Trios 3 displayed a precision of 46 μm for D1_3 and 57 μm for D2_3, while D1_2 had a lowest precision of ≤206 μm.

3.2.2. Trios 3 Mono. In the z-axis, Trios 3 mono showed an overall precision of ≤28 μm and for the y-axis ≤33 μm. However, x-axis showed a low precision of ≤100 μm. In the interarch measurements, Trios 3 mono displayed a precision of 52 μm for D1_3 and 22 μm for D2_3. But, D1_2 presented a low precision of ≤111 μm.

3.2.3. Itero Element. In the z-axis, Itero showed an overall precision of ≤40 μm and for the y-axis ≤44 μm. However, x-axis showed a low precision of ≤101 μm. In the interarch measurements, Itero displayed a precision of 28 μm for D1_3

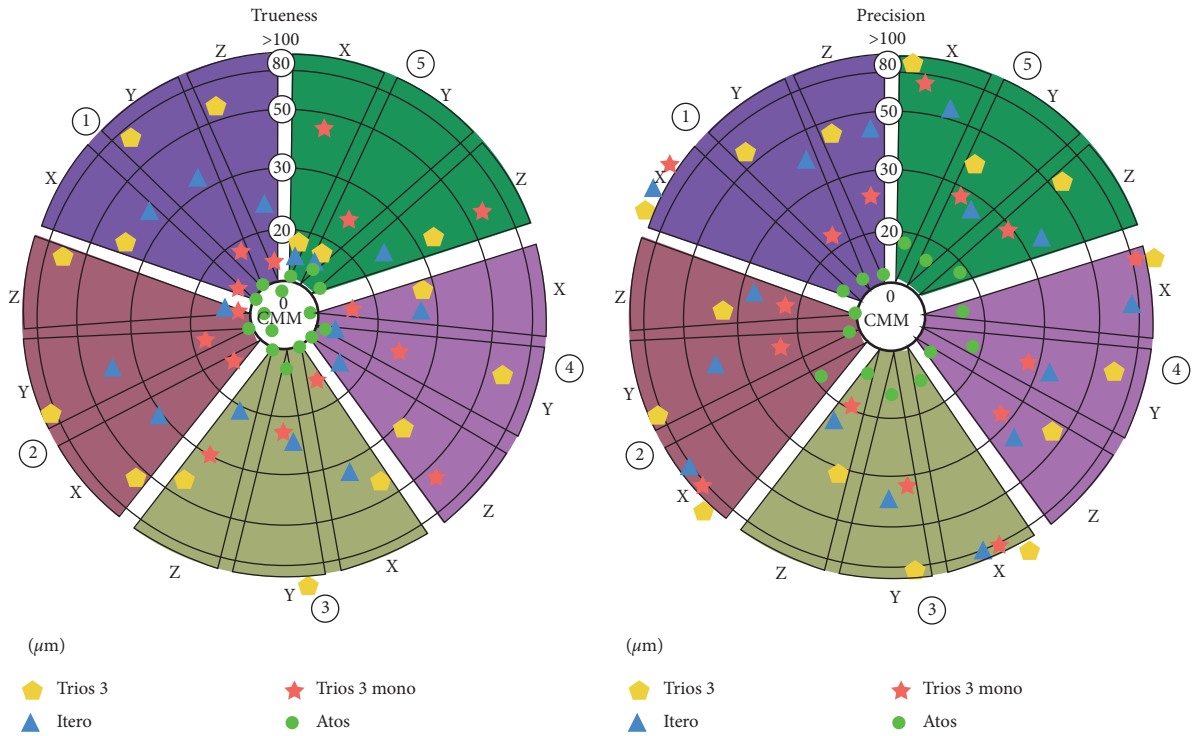

FIGURE 5: Bull's eyes chart showing the deviations between the mean of repeated measurements for all implant axes of all scanner devices and the true values (trueness) and the deviations between the results of independent measurements obtained within one scanner device under specific condition (precision). This chart is color-coded; each color represents the implant number (1–5) in the master model. μm = micron.

and 40 μm for D2_3. On the other hand, D1_2 was had precision of ≤124 μm.

3.2.4. Atos Scanner. Atos scanner displayed a highest precision of ≤19 μm for all implant parameters. Atos had a precision of ≤26 μm in all interarch measurements.

3.3. Results of Statistical Analysis between CMM, Atos, and the Dental Scanner Systems. According to the results of the ANOVA, significant differences were found between the mean of all IOS devices and in comparison with the true value for all implant points and interarch distances, except for implant 1 x-axis ($p = 0.175$), implant 4 x-axis ($p = 0.128$), and D1_D2 ($p = 0.332$). Table 5 displays the statistically significant difference in implants and interarch distances between two specific test groups.

4. Discussion

The aim of this study was to measure trueness and precision of different IOS systems when digitizing a fully edentulous cast with multiple implants. The results do not support the null hypothesis as statistically significant differences were found between the IOS devices in comparison with the true value. This in vitro study found variations in trueness and precision depending on the optical scanner systems utilized. On the basis of the x, y, and z parameters, Atos showed higher trueness and precision than all tested scanners. It would be preferable for the Atos system to be utilized by dentists; however, if the same scanning technology utilized by Atos was applied inside an intraoral device, the size of the hand-piece tip would be enormous and probably difficult to use intraorally. The authors of this study decided to use the Atos scanner as a reference scanner.

The material of the object surface being measured has an important influence on the scan result. The master model utilized in the current study consisted of stone material for the edentulous areas and tungsten metal for the implant positions (Figure 2). The stable metal part limits the movement or displacement of implant analogs in the master model to some extent and minimizes the risk of changes that could influence the results. However, the metallic parts could cause light reflective problems during the scanning process. Therefore, stone material was applied in the edentulous areas. The master model contained three spheres and five cylindrical scanning abutments, geometrical shapes that were used as fixed landmarks to assist the operator during scanning, making it possible to align and measure the virtual 3D model in a reliable way. In addition, the PEEK scanning abutment was selected because of its optical properties that produce good light dispersion.

The correlation between trueness and precision is a significant aspect in choosing a suitable IOS scanner for the intended application. The data that resulted from the current study on implant measurements for Trios 3 showed trueness data ≤114 μm and Trios 3 mono presented trueness data ≤63 μm. The same data from the Itero element showed trueness values ≤−41 μm. There is no consensus between

studies concerning the standard precision level for each intraoral scanner system. In this study, the reference Atos showed a precision of ≤19 μm in all implant dimensions. On the other hand, Trios 3 mono and Itero element presented precision of approximately <45 μm in the y and z direction, but the x-axis displayed low precision at ≤101 μm. Also, Trios 3 has the lowest precision of ≤135 μm in the x-axis. The precision of those IOS systems was not optimal enough to produce several virtual models that are closely comparable to each other in the x-axis. Thus, in the present study, the results from precision indicated that all tested IOS systems were not reliable enough for scanning fully edentulous arch with multiple implants.

The comparison of obtained values with the available literature is difficult; to our knowledge, there is no study using an identical measuring method to that of the present study. Some studies have utilized the best fit alignment method to assess direct digital impression of dentate arch or edentulous arch with multiple implants [4, 7, 8, 16]. The method refers to superimposing tested scans onto a reference scan of a physical model in different 3D software. The protocol can generate errors caused by alignment computing processes because of the deviations between the superimposed areas, especially in larger datasets such as full-arch scans [17, 18]. However, some studies have assessed accuracy of IOS devices by measuring only the horizontal linear distances between the reference landmarks [6, 9, 15, 19, 20]. The use of different IOS versions in the majority of the studies had an impact on the dissimilar results obtained. It can be assumed that the different materials and methods can lead to conflicting results in relation to the accuracy of IOS systems.

Intraoral scanners do not have the ability to scan the entire arch in one image. The small hand-piece unit has to move across the arch. The scanner's software stitches the images of the arch and implant and combines one image after another image; this seems to induce errors. The clear effect of the stitching processes producing errors proportional to the scan distance, as noted in this study, has also been documented in other studies [6, 9, 10]. The results indicated that the errors were increased if the interarch distance between the spheres is horizontally enlarged or reduced in width. The data found from the current study on interarch measurements for Trios 3 showed lowest trueness among other groups, but all tested scanners had low precision. Contradictory results can be found in the study that measured the trueness and precision of Trios (unclear version) and Itero (unknown version) on scanning dental arch [19]. Muallah and coworkers utilized five boreholes on their 3D printed master cast that were measured utilizing tactile CMM, and the cast was scanned thirty-two times per IOS device. Two of the boreholes replaced the first molars; the intermolar width (IMW) measurement in that study is similar to the interarch measurement D1_D2 in the current study. They found that Trios and Itero had better trueness and precision values. The difference in the results could be caused by different model materials, a different 3D analyzing program, a different software version of the scanners, and different reference landmark size and shapes. The most significant difference that led to better results in their study was that the arch is not edentulous. It should be noted that the IOS software can cause poor stitching and matching procedure of the single point clouds during the scanning process of the edentulous area. By improving the matching algorithms, some IOS devices could attain digital impression of fully edentulous arches with multiple implants cases in the near future.

The accuracy of full-arch scan is correlated with the correct scanning strategy. Muller et al. [13] reported that the zigzag strategy has a lower trueness value but a better precision value than buccal-occlusal-palatal (BOP) strategy. In the present study, both Trios scanners used the BOP strategy and Itero element used the zigzag strategy to scan the master model. The results showed that the Itero element presented better trueness and precision outcomes than Trios 3, and statistically significant difference was found between them. However, Trios 3 mono and Itero element presented comparable results, with a statistically significant difference. Trios 3 mono has no color feature, which might explain why the scanning strategy played no significant role between the two different systems. It can be suggested that the color software collects information related to the color of the object being scanned during the scanning process. Subsequently, color software may interfere with the quality of the stitching process. Lastly, this study failed to account for saliva, soft tissue isolation, patient movement, and humidity in the oral environment. These patient variables may affect accuracy considerably in a clinical situation. The laboratory procedures after scanning also introduce errors that need to be considered.

No power calculation was performed in this study, which could be considered a limitation. The sample size was instead based on ISO standard 12836:2015 which states that, to test a digital device in terms of accuracy, trueness, and precision, the measurement has to be repeated 30 times, which is what was done in this paper [2]. Another limitation of this present study was that all tested scanner systems have similar scanning technology.

The findings in this study do not relate directly to the definitive prostheses. However, the level of model-less digital production tolerances for full-arch framework supported by teeth or implants is not clearly known yet. One of the most common treatment modalities is an implant-supported fixed full-arch framework. Örtorp et al. [20] reported that the production tolerance for implant-supported fixed prostheses should be in the range of 20–100 μm tolerance. Comparison of their findings with this current study results should be done with consideration since the frameworks in their study were produced from scanning the implant master cast with a laboratory scanner. One good example is that the trueness of Trios 3 was ≤114 μm at y-axis with precision 135 μm at x-axis. This could generate a misfit between the components of the whole implant prosthesis, or it could produce unfit implant frameworks. A pilot clinical study investigated the digital impression of 25 patients with two implants in the mandible and reported that errors were too large to fabricate well-fitting implant frameworks [5].

The results of this present study provide the knowledge of the nature of deviation in full-arch digital impression and can help to avoid these errors in future. The study was

conducted to provide knowledge for dental professionals to understand and control the digital scanning process. Future studies need to include more dental scanner systems and compare them in different clinical scenarios. The whole model-less digital production for full-tooth-fixed supported prostheses and full implant-fixed supported prostheses workflow should be assessed.

5. Conclusion

Within the limitations of this in vitro study, the results suggest significant differences between IOS devices when scanning fully edentulous arch with multiple implants. The main observation was the low precision for all intraoral scanners, suggesting that the intraoral scanning devices are unreliable for scanning fully edentulous arch with multiple implants. Two scanners, however, Trios 3 mono and Itero element showed fair trueness.

Data Availability

The data used to support the findings of this study are available from the corresponding author upon reasonable request.

Conflicts of Interest

The authors declare no conflicts of interest.

Acknowledgments

The research was supported by the Department of Prosthodontics, Faculty of Odontology, Malmö University. We would like to thank Elos Medtech Pinol Denmark for providing us with the master model and measurement with CMM, Kulzer GmbH Sweden for scanning the master model with Atos, 3Shape Denmark for providing us with the Trios scanners, and Unident AB Sweden for providing us with the Itero element system.

References

[1] W. H. Mörmann, "The evolution of the CEREC system," *Journal of the American Dental Association*, vol. 137, pp. 7S–13S, 2006.

[2] ISO 12836, *Dentistry–Digitizing Devices for CAD/CAM Systems for Indirect Restorations–Test for Methods for Assessing Accuracy*, International Organization for Standardization, Geneva, Switzerland, 2015.

[3] R. Nedelcu, P. Olsson, I. Nystrom, J. Ryden, and A. Thor, "Accuracy and precision of 3 intraoral scanners and accuracy of conventional impressions: a novel in vivo analysis method," *Journal of Dentistry*, vol. 69, pp. 110–118, 2018.

[4] M. Imburgia, S. Logozzo, U. Hauschild, G. Veronesi, C. Mangano, and F. G. Mangano, "Accuracy of four intraoral scanners in oral implantology: a comparative in vitro study," *BMC Oral Health*, vol. 17, no. 1, p. 92, 2017.

[5] F. S. Andriessen, D. R. Rijkens, W. J. van der Meer, and D. W. Wismeijer, "Applicability and accuracy of an intraoral scanner for scanning multiple implants in edentulous mandibles: a pilot study," *Journal of Prosthetic Dentistry*, vol. 111, no. 3, pp. 186–94, 2014.

[6] Van der Meer, J. Wicher, F. S. Andriessen, W. Daniel, and Y. Ren, "Application of intra-oral dental scanners in the digital workflow of implantology," *PLoS One*, vol. 7, no. 8, Article ID e43312, 2012.

[7] A. Ender and A. Mehl, "In-vitro evaluation of the accuracy of conventional and digital methods of obtaining full-arch dental impressions," *Quintessence International*, vol. 46, pp. 9–17, 2015.

[8] F. G. Mangano, G. Veronesi, U. Hauschild, E. Mijiritsky, and C. Mangano, "Trueness and precision of four intraoral scanners in oral implantology: a comparative in vitro study," *PloS One*, vol. 11, no. 9, Article ID e0163107, 2016.

[9] B. Giménez, M. Özcan, F. Martínez-Rus, and G. Pradíes, "Accuracy of a digital impression system based on parallel confocal laser technology for implants with consideration of operator experience and implant angulation and depth," *International Journal of Oral and Maxillofacial Implants*, vol. 29, pp. 853–862, 2014.

[10] B. Giménez, B. Hassan, M. Özcan, and G. Pradíes, "An in vitro study of factors influencing the performance of digital intraoral impressions operating on active wavefront sampling technology with multiple implants in the edentulous maxilla," *Journal of Prosthodontics*, vol. 26, no. 8, pp. 650–655, 2017.

[11] T. V. Flügge, S. Schlager, K. Nelson, S. Nahles, and M. C. Metzger, "Precision of intraoral digital dental impressions with iTero and extraoral digitization with the iTero and a model scanner," *American Journal of Orthodontics and Dentofacial Orthopedics*, vol. 144, no. 3, pp. 471–478, 2013.

[12] J. H. Kim, K. B. Kim, S. H. Kim, W. C. Kim, H. Y. Kim, and J. H. Kim, "Quantitative evaluation of common errors in digital impression obtained by using an LED blue light in-office CAD/CAM system," *Quintessence International*, vol. 46, pp. 401–407, 2015.

[13] P. Müller, A. Ender, T. Joda, and J. Katsoulis, "Impact of digital intraoral scan strategies on the impression accuracy using the TRIOS Pod scanner," *Quintessence International*, vol. 47, pp. 343–349, 2016.

[14] A. Ender and A. Mehl, "Influence of scanning strategies on the accuracy of digital intraoral scanning systems," *International Journal of Computerized Dentistry*, vol. 16, pp. 11–21, 2013.

[15] T. V. Flügge, W. Att, M. C. Metzger, and K. Nelson, "Precision of dental implant digitization using intraoral scanners," *International Journal of Prosthodontics*, vol. 29, no. 3, pp. 277–283, 2016.

[16] P. Papaspyridakos, G. O. Gallucci, C. -J. Chen, S. Hanssen, I. Naert, and B. Vandenberghe, "Digital versus conventional implant impressions for edentulous patients: accuracy outcomes," *Clinical Oral Implants Research*, vol. 27, no. 4, pp. 465–72, 2016.

[17] J. F. Güth, D. Edelhoff, J. Schweiger, and C. Keul, "A new method for the evaluation of the accuracy of full-arch digital impressions in vitro," *Clinical Oral Investigations*, vol. 20, no. 7, pp. 1487–1494, 2016.

[18] F. Kuhr, A. Schmidt, P. Rehmann, and B. Wostmann, "A new method for assessing the accuracy of full arch impressions in patients," *Journal of Dentistry*, vol. 55, pp. 68–74, 2016.

[19] J. Muallah, C. Wesemann, R. Nowak et al., "Accuracy of full-arch scans using intraoral and extraoral scanners: an in vitro study using a new method of evaluation," *International Journal of Computerized Dentistry*, vol. 20, pp. 151–164, 2017.

[20] A. Örtorp, T. Jemt, T. Bäck, and T. Jalevik, "Comparisons of precision of fit between cast and CNC-milled titanium implant frameworks for the edentulous mandible," *International Journal of Prosthodontics*, vol. 16, pp. 194–200, 2003.

Hindawi
International Journal of Dentistry
Volume 2018, Article ID 5463753, 10 pages
https://doi.org/10.1155/2018/5463753

Research Article

Three-Dimensional Changes of the Auditory Canal in a Three-Year Period during Adolescence Using CBCTs

Adam Woods[1] **and Manuel O. Lagravère**[2]

[1]*Undergraduate Student, School of Dentistry, Faculty of Medicine & Dentistry, University of Alberta, ECHA, 11405-87 Avenue, Edmonton, Alberta, Canada T6G 1C9*
[2]*Associate Professor, School of Dentistry, Faculty of Medicine & Dentistry, University of Alberta, Edmonton, Alberta, Canada*

Correspondence should be addressed to Manuel O. Lagravère; mlagravere@ualberta.ca

Received 7 June 2018; Revised 23 August 2018; Accepted 20 September 2018; Published 22 October 2018

Guest Editor: Vahid Rakhshan

Purpose. There is a lack of identifying suitable regions in the head that can be used for three-dimensional superimposition techniques. For this reason, with the use of cone-beam computed tomography (CBCT), the ear canals were analyzed to verify changes during a period of three years in the adolescent years. *Methods*. CBCTs from fifty-six patients (ages: 10 to 20) were used to landmark the anatomy of the ear canals. Each patient was analyzed using two CBCT reconstructions that were taken approximately three years apart. AVIZO® software was used to locate 28 landmarks distributed following the ear canal path and foramina (ovale, spinosum, rotundum, etc.) in the cranial base to obtain spatial relationships. Three-dimensional coordinates were obtained from the landmarks, and the average distance between various landmark pairings was calculated. The repeated measure ANCOVA was used to determine statistical significance. *Results*. In the main data set, the largest mean distance change was found to be 4.37 mm ± 18.29 mm between the left foramen ovale and the left superior medial ear canal opening. The smallest mean distance change was 0.18 mm ± 3.25 mm between the right inferior lateral ear canal opening and the right inferior medial ear canal opening. *Conclusions*. During the adolescent years, the ear canal presents dimensional changes. Even though in different areas throughout the canal, the average distances were minor, still, large standard deviations were present; thus, caution should be taken when trying to use this structure for superimposition of CBCTs.

1. Introduction

Cone-beam computed tomography (CBCT) has become a popular imaging tool for dental practitioners in North America to visualize structures in the head and neck in three dimensions (3D). While CBCTs struggle with the differentiation of very similar density soft-tissue structures, they produce a high-resolution image when compared to 2D imaging at a lower cost and lower radiation dose when compared to medical CT [1]. The 3D capabilities of CBCTs allow clinicians to better understand a patient's dental development, the potential for dental movement, and possible airway obstruction.

CBCTs have become useful in orthodontic treatment, allowing practitioners to monitor treatment efficacy [2]. Of particular interest are the advantages that CBCTs offer practitioners when trying to superimpose facial structures to assess treatment outcomes. Historically, superimposition has been done using two-dimensional (2D) lateral cephalograms, primarily focusing on relatively stable structures, including the sella turcica, lingual curvature of the palate, and inner border of the symphysis [3]. Evidently, the potential for cephalometric analysis and diagnosis is promising as we move towards the 3D capabilities of CBCT [4]. The caveat of new technology, of course, is that a lot of analysis and optimization is required to establish reliability. Various authors have developed methods of reducing error associated with superimposition of structures using CBCT, most typically using landmarks such as the left and right auditory meatus, the left and right infraorbitale, the left and right

menton, the dorsum foramen magnum [5], anterior wall of the sella turcica, planum sphenoidale, and superior portion of the ethmoid bone [2]. In order to more effectively establish the efficacy of these structures as reference points, it is logical that they should be analyzed using CBCT to determine the extent to which they are changing over time.

The auditory meatus has been landmarked and measured through a number of methods including histological techniques [6], moulding [7], computed tomography imaging [8, 9], dissection [10], magnetic resonance imaging [9], and direct fluid measurements [11]. Previous investigation has indicated that while the auditory meatus undergoes a great deal of development during the embryonic, fetal, and childhood periods, development typically slows and finalizes during the adolescent years [7]. While the auditory meatus has been imaged 2D for use as a reference point in orthodontic treatment [12], it has not been investigated thoroughly in 3D.

A further understanding of the developmental processes that occur in the auditory meatus would have a positive outcome in orthodontic treatment planning. If this structure remains relatively stable in terms of dimensional changes throughout adolescent development, it is possible that it could be used as a reference structure. In the proposed study, images taken using CBCT will be used to landmark and assess development of the auditory meatus in adolescents over two time points. It is hypothesized that the auditory canal will present no significant change over these time periods.

2. Materials and Methods

CBCTs of 56 patients were selected from the Graduate Orthodontic Clinic patient pool in Edmonton, Alberta. These patients were part of clinical trials involving analysis of CBCTs, and patients were informed that taking of CBCT is not the standard of care. With this, it is not suggested that CBCTs should be taken on everybody. Inclusion criteria for the patients were 10–20 years of age, full permanent dentition (with exception of third molars), and absence of syndromic characteristics or systematic disease. A power sample calculation was done considering 80% power and a 5% alpha level using data from Lagravere et al. [13] demonstrated that a sample of 25 patients per group was sufficient using a difference of 1.5 mm. Since we had more available, it was decided to analyze all the samples available in the database. Approximately three years existed between each patient's serial CBCTs, signalling the start and end of orthodontic treatment. CBCT scans were taken using the ICat New Generation (Imaging Sciences International, Hatfield, PA) machine at 0.3 mm voxel size and 8.9 seconds, 13 cm × 16 cm FOV, 120 kV, and 5 mAs with 8 mm aluminum filtration and converted into the DICOM format. The images were analyzed using Avizo 8.1 software (Visualization Science Group, New England, MA). Eight landmarks within each auditory meatus were located, including the superior-, inferior-, anterior-, and posterior-most aspects of the bony limit of the right and left ear canal laterally, and the termination of the Eustachian tubes medially (Figure 1).

As one observer performed the landmarking in this study, it was important to verify that the placement of each landmark could be replicated reliably. To do so, landmarks throughout the cranial base were located on 10 different CBCTs, each coming from a separate patient. From the ear canal landmarks, other 12 landmarks located in different structures of the cranial base were located. The selection of these extra 12 landmarks was based on analysis of the cranial base and selecting structures that can be easily located and recognized in the cranial base. This was repeated once a week for three weeks. In total, 28 landmarks were assessed in each patient, as shown in Figure 1 and Table 1. The three iterations of each landmark were then analyzed for consistency using a 95% confidence interval (CI 95). This was done by subtracting the coordinates of one trial with the ones of another trial (for example, Trial 1-Trial 2, Trial 1-Trial 3, and Trial 2-Trial 3), and then, these differences were averaged to obtain an average measurement error.

Once reliability was determined, CBCTs from the main patient pool were analyzed. The auditory canal was isolated and landmarked in each image so that various dimensions could be analyzed. After landmarks are located, distances were calculated using the following equation (Table 2):

$$d = \sqrt{(X_1 - X_2)^2 + (Y_1 - Y_2)^2 + (Z_1 - Z_2)^2}. \quad (1)$$

Analysis included serial patient images taken from two different time points, so that the change in dimension over time could be assessed. Descriptive statistics were calculated for all distances and for the differences between corresponding distances at the two time points. Sex and age distribution are shown in Table 3. A repeated measures analysis of covariance (ANCOVA) was applied to the data having age at baseline and gender as covariates. This analysis was done to verify if there was a statistical significant difference between both time points ($p < 0.05$).

3. Results

In order to ensure reliability of the landmarks chosen, the CBCTs of ten patients were landmarked three times, with one week in between each landmarking session. The largest measurement error was found in the Z-coordinates of the left ear canal lateral opening posterior landmark (Figure 1) at 2.0 mm. The smallest measurement error was found in the Z-coordinates of the crista galli landmark at 0.1 mm. Intraclass correlation coefficient (ICC) is a commonly used tool to assess intraobserver reliability. In this study, the lowest ICC value was from the left anterior lateral ear canal landmark at 0.99 (CI 0.95–1.00). All landmarks were determined to have appropriate reliability (Table 1).

Twenty-eight distances between 15 different landmarks were used to determine whether the ear canal changed

Landmark	Axial view (XY)	Coronal view (YZ)	Sagittal view (XZ)
Crista galli (CG) definition: superior most point of the crista galli	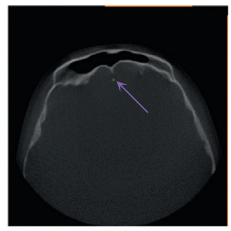	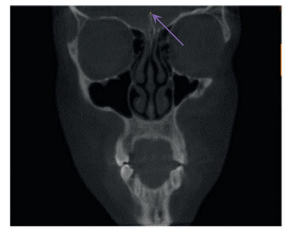	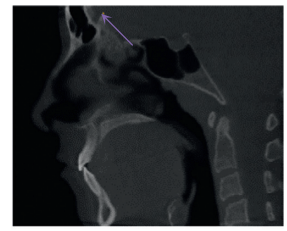
Left foramen ovale (FO) definition: centre of the left foramen ovale	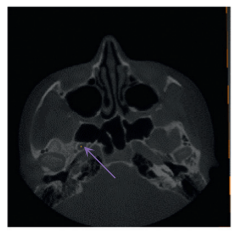	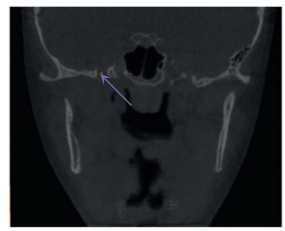	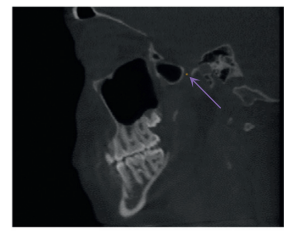
Right foramen ovale (FO) definition: centre of the right foramen ovale	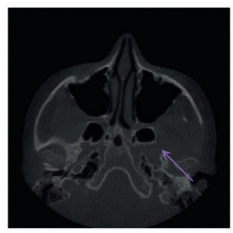	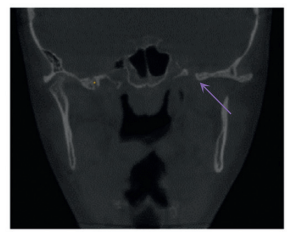	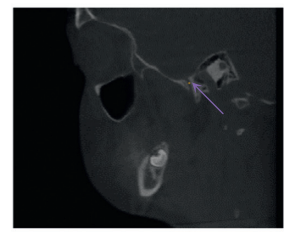
Left foramen spinosum (FS) definition: centre of the left foramen spinosum	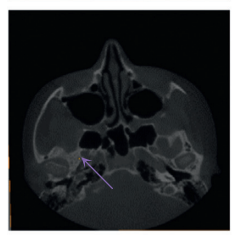	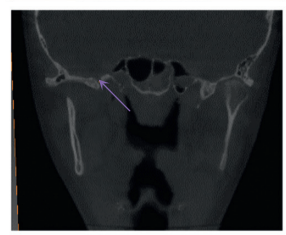	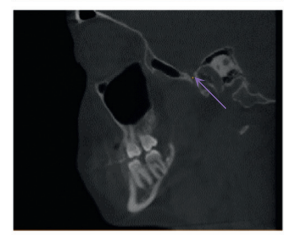
Right foramen spinosum (FS) definition: centre of the right foramen spinosum	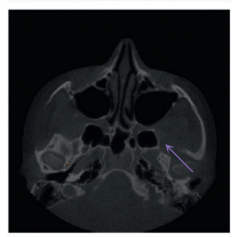	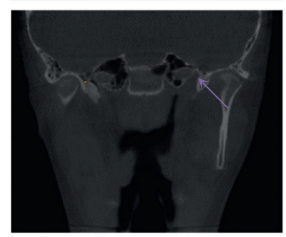	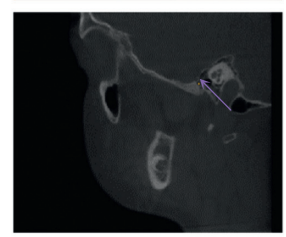
Left foramen rotundum (FR) definition: centre of the left foramen rotundum	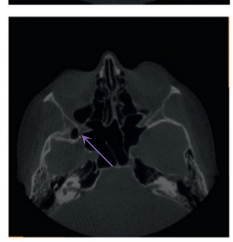	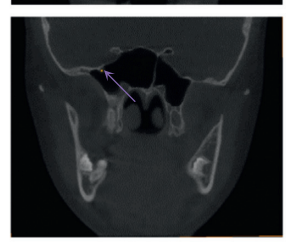	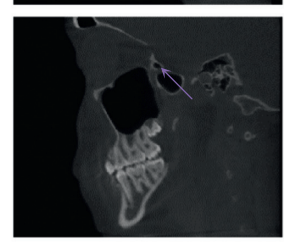
Right foramen rotundum (FR) definition: centre of the right foramen rotundum	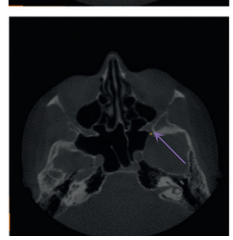	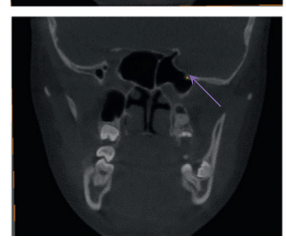	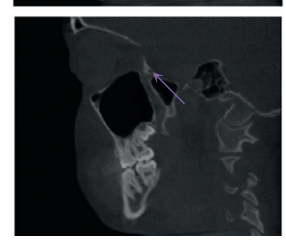

Figure 1: Continued.

Landmark	Axial view (XY)	Coronal view (YZ)	Sagittal view (XZ)
Foramen magnum (FM) definition: anterior-inferior most point of the foramen magnum	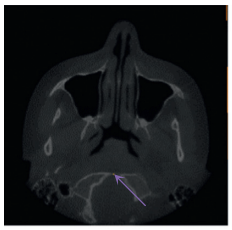	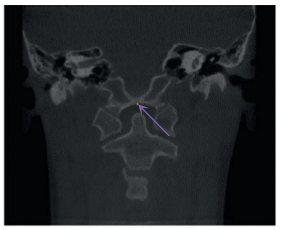	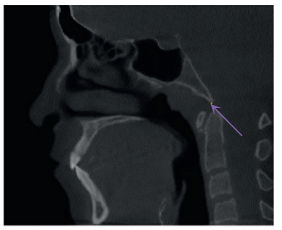
Left posterior vidian canal (PVC) definition: centre of the posterior opening of the left vidian canal	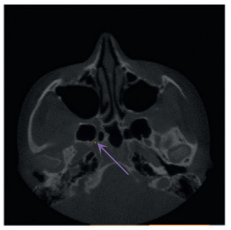	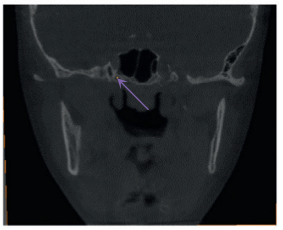	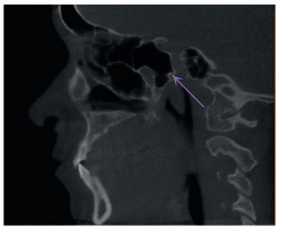
Right posterior vidian canal (PVC) definition: centre of the posterior opening of the right vidian canal	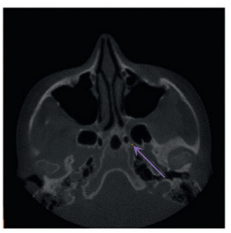	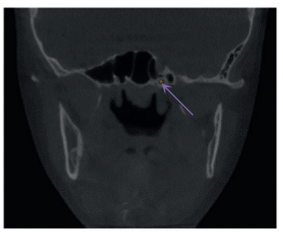	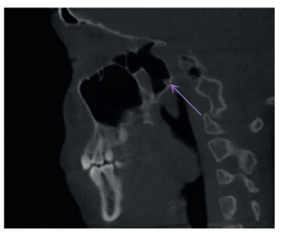
Left hypoglossal canal (HC) definition: centre of the left hypoglossal canal	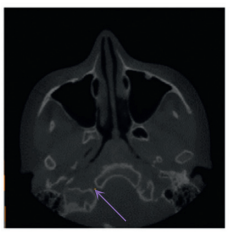	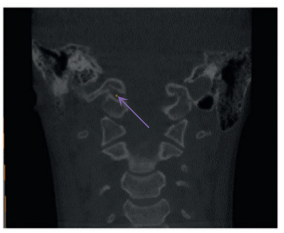	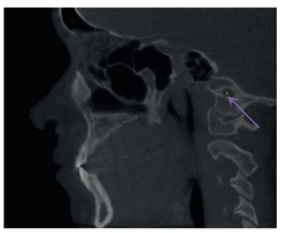
Right hypoglossal canal (HC) definition: centre of the left hypoglossal canal	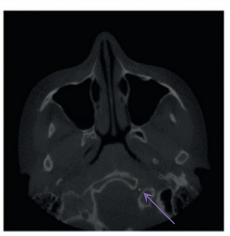	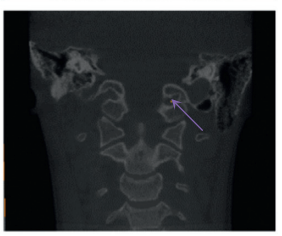	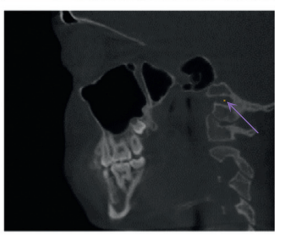
Left ear canal lateral opening superior (ECLOS) definition: superior-most point of the left ear canal, at its lateral bony limit	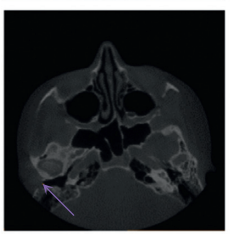	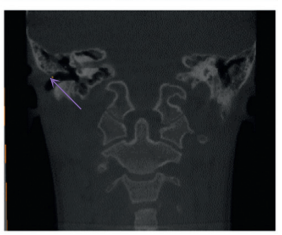	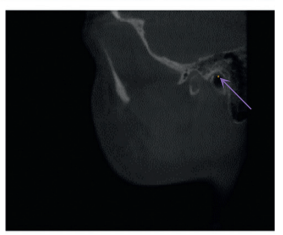
Left ear canal lateral opening inferior (ECLOI) definition: inferior-most point of the left ear canal, at its lateral bony limit	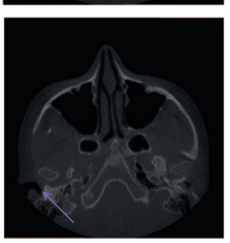	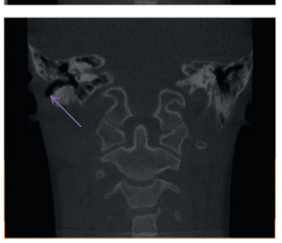	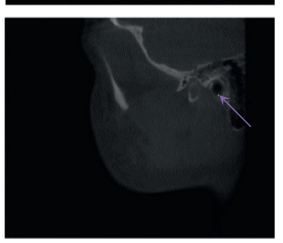

Figure 1: Continued.

Landmark	Axial view (XY)	Coronal view (YZ)	Sagittal view (XZ)
Left ear canal later opening anterior (ECLOA) definition: anterior-most point of the left ear canal, at its lateral bony limit	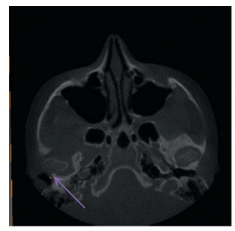	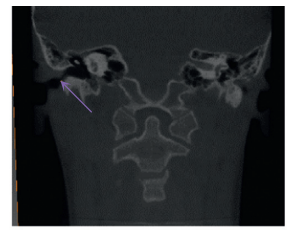	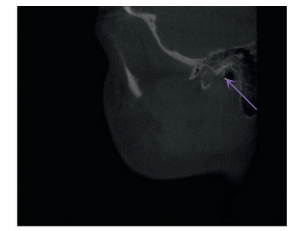
Left ear canal lateral opening posterior (ECLOP) definition: Posterior-most point of the left ear canal, at its lateral bony limit	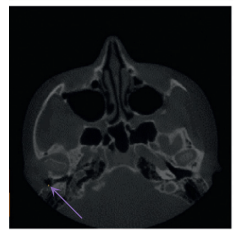	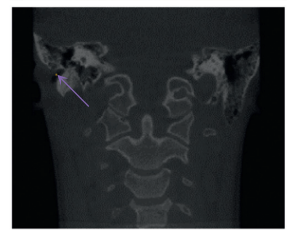	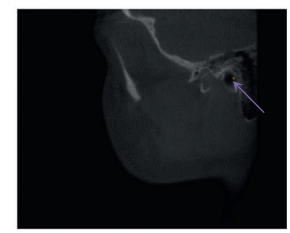
Right ear canal lateral opening superior (ECLOS) definition: superior-most point of the right ear canal, at its lateral bony limit	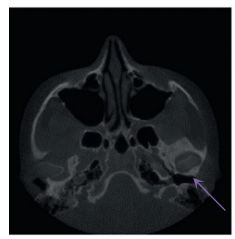	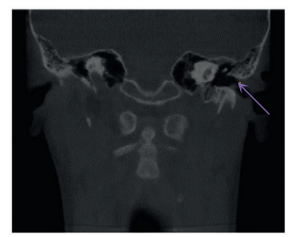	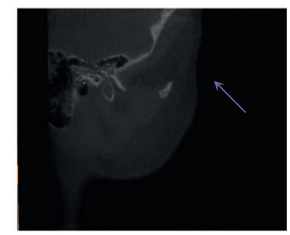
Right ear canal lateral opening inferior (ECLOI) definition: inferior-most point of the right ear canal, at its lateral bony limit	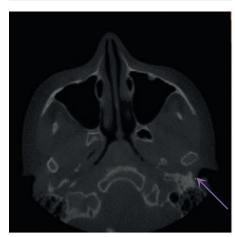	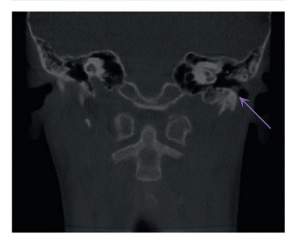	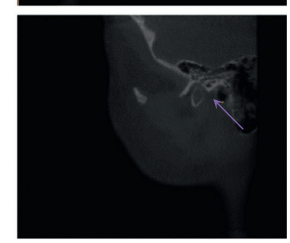
Right ear canal lateral opening anterior (ECLOA) definition: anterior-most point of the right ear canal, at its lateral bony limit	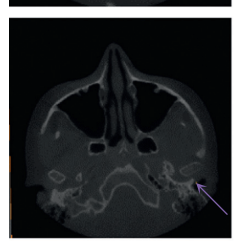	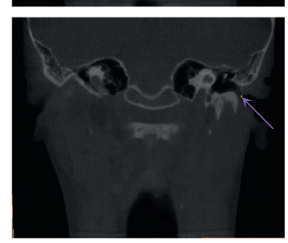	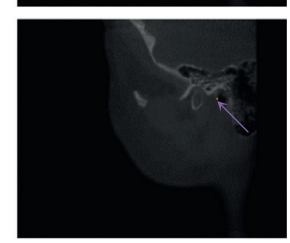
Right ear canal lateral opening posterior (ECLOP) definition: posterior-most point of the right ear canal, at its lateral bony limit	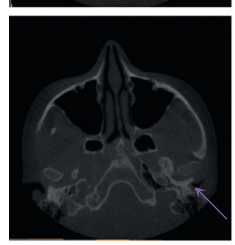	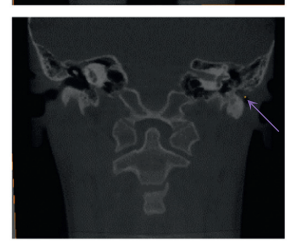	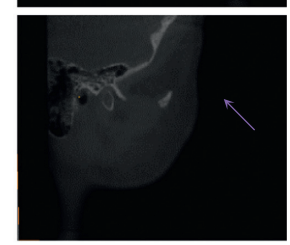
Left ear canal medial opening superior (ECMOS) definition: superior-most point of the left ear canal, at the terminus of the open eustachian tube	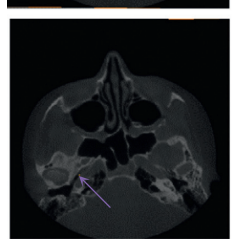	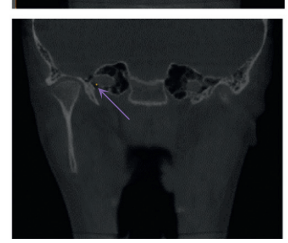	

Figure 1: Continued.

Landmark	Axial view (XY)	Coronal view (YZ)	Sagittal view (XZ)
Left ear canal medial opening inferior (ECMOI) definition: inferior-most point of the left ear canal, at the terminus of the open eustachian tube	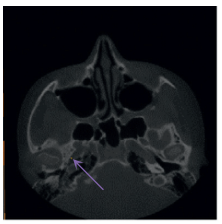	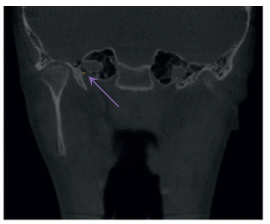	
Left ear canal medial opening anterior (ECMOA) definition: anterior-most point of the left ear canal, at the terminus of the open eustachian tube	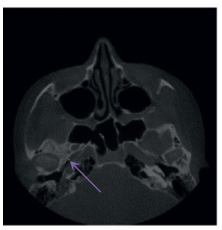	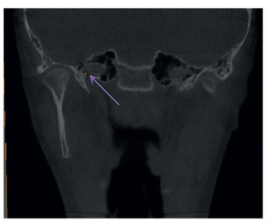	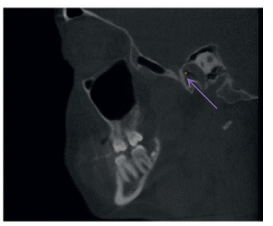
Left ear canal medial opening posterior (ECMOP) definition: posterior-most point of the left ear canal, at the terminus of the open eustachian tube	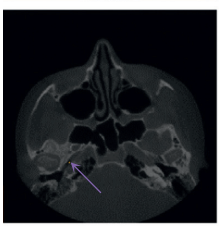	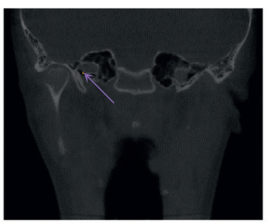	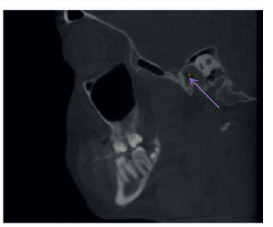
Right ear canal medial opening superior (ECMOS) definition: superior-most point of the right ear canal, at the terminus of the open eustachian tube	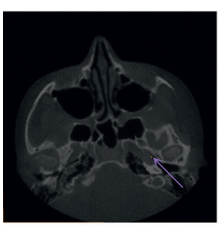	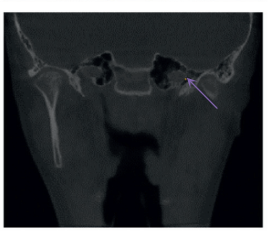	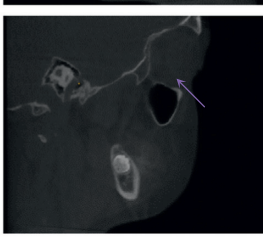
Right ear canal medial opening inferior (ECMOI) definition: inferior-most point of the left ear canal, at the terminus of the open eustachian tube	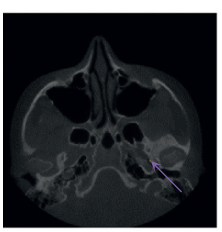	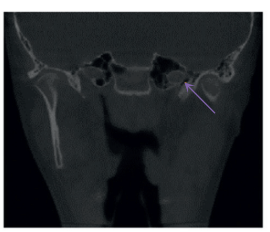	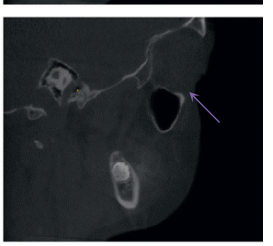
Right ear canal medial opening anterior (ECMOA) definition: anterior-most point of the left ear canal, at the terminus of the open eustachian tube	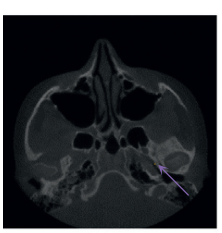	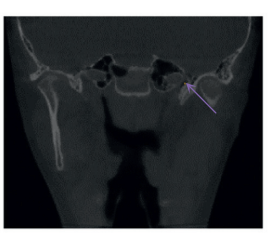	
Right ear canal medial opening posterior (ECMOP) definition: posterior-most point of the left ear canal, at the terminus of the open eustachian tube	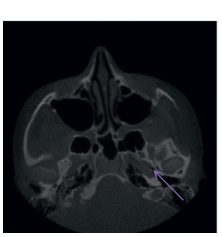	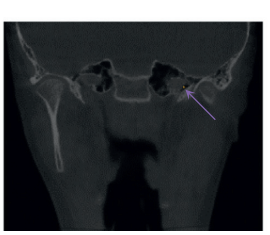	

Figure 1: Landmarks used for reliability and distance analysis.

Table 1: Mean measurement errors in X, Y, and Z coordinates for each landmark.

Landmark	Mean			SD		
	X	Y	Z	X	Y	Z
Crista galli (CG)	0.16	0.47	0.10	0.07	0.05	0.12
Left foramen ovale (FO)	0.51	0.52	0.55	0.33	0.31	0.50
Right foramen ovale (FO)	0.55	0.45	0.47	0.36	0.25	0.27
Left foramen spinosum (FS)	0.28	0.31	0.45	0.18	0.20	0.22
Right foramen spinosum (FS)	0.30	0.34	0.48	0.22	0.11	0.28
Left foramen rotundum (FR)	0.35	0.62	0.23	0.24	0.44	0.08
Right foramen rotundum (FR)	0.48	0.79	0.41	0.31	0.91	0.48
Foramen magnum (FM)	0.41	0.43	0.31	0.21	0.17	0.13
Left posterior vidian canal (PVC)	1.04	1.15	0.50	1.21	0.78	0.39
Right posterior vidian canal (PVC)	0.62	1.01	0.44	1.03	0.78	0.33
Left hypoglossal canal (HC)	0.37	0.39	0.85	0.20	0.25	0.59
Right hypoglossal canal (HC)	0.51	0.95	1.00	0.15	0.66	0.67
Left ear canal lateral opening superior (ECLOS)	1.88	0.62	1.28	1.55	0.43	1.03
Left ear canal lateral opening inferior (ECLOI)	1.88	1.89	1.50	1.55	1.45	1.33
Left ear canal lateral opening anterior (ECLOA)	1.88	1.41	1.47	1.55	0.95	0.85
Left ear canal lateral opening posterior (ECLOP)	1.88	0.98	2.02	1.55	0.82	1.56
Left ear canal medial opening superior (ECMOS)	1.15	0.54	0.73	1.53	0.58	0.50
Left ear canal medial opening inferior (ECMOI)	1.15	0.66	0.79	1.53	0.62	0.56
Left ear canal medial opening anterior (ECMOA)	1.15	0.65	0.63	1.53	0.54	0.49
Left ear canal medial opening posterior (ECMOP)	1.15	0.66	0.75	1.53	0.63	0.43
Right ear canal lateral opening superior (ECLOS)	1.18	0.47	1.40	0.70	0.18	0.74
Right ear canal lateral opening inferior (ECLOI)	1.18	1.48	1.06	0.70	1.04	0.70
Right ear canal lateral opening anterior (ECLOA)	1.18	1.13	1.49	0.70	0.63	0.53
Right ear canal lateral opening posterior (ECLOP)	1.18	0.59	1.77	0.70	0.38	1.06
Right ear canal medial opening superior (ECMOS)	0.80	0.41	0.67	1.40	0.21	0.33
Right ear canal medial opening inferior (ECMOI)	0.80	0.49	0.49	1.40	0.24	0.35
Right ear canal medial opening anterior (ECMOA)	0.80	0.43	0.59	1.40	0.24	0.32
Right ear canal medial opening posterior (ECMOP)	0.80	0.49	0.59	1.40	0.39	0.35

significantly in vertical, anterior-posterior, and transverse dimensions throughout adolescent development. All distances analyzed did not present with a statistically significant ($p > 0.05$) change over the time period when viewing the repeated measures ANCOVA test. When analyzing the raw distance changes (Table 2), it is observed that 6 of the 28 distances presented changes larger than 2 mm. These distances were mostly related to foramen ovale and foramen rotundum relationship. The rest of distances within the ear canal presented differences less than 2 mm. The greatest overall change was found to be 4.4 mm (Table 2), from the left foramen ovale to the left ear canal medial opening superior (Figures 2 and 3).

4. Discussion

The popularity of CBCTs in orthodontics has increased in recent years as a result of its enhanced 3D diagnostic information when compared to conventional radiographic imaging and its reduced radiation dose when compared to multislice CT [14, 15]. It should be noted that even if the radiation of CBCT is less than medical CT, it is still higher compared to traditional two-dimensional radiographs; thus, caution should be taken when assigning a patient to have a CBCT taken. In order to effectively monitor the effectiveness of orthodontic treatment, it is important to be able to reference orthodontic changes in relation to structures that remain stable over the treatment period. A number of studies have discussed the difficulty in establishing the reliability of landmarking the external auditory meatus [13, 16, 17]. In this study, landmarks were placed on the superior-, inferior-, anterior-, and posterior-most positions of the external auditory meatus just lateral to the point where it is surrounded in bone. We were unable to locate a study referencing a reliable landmark to represent the medial end of the ear canal. Additionally, due to the difficulty associated with identifying bony structures within the inner ear, landmarks representing the medial portion of the ear canal were placed in a reliably reproducible location at the end of the Eustachian tubes.

The majority of distances analyzed involving the ear canal did not show a significant change over the observed development period. Four of the five significant changes occurred in distances representing the heights and widths of the ear canal end points. This is most likely a result of differences in CBCT quality. These landmarks were placed on soft-tissue borders, even though they were referenced using neighbouring bony structures. As a result, in certain data sets, a difference in image quality could have influenced the placement of these landmarks to some degree. In most cases, the change seen in these distances was just over 1 mm, and as a result would likely be insignificant clinically.

Table 2: Change in distances between T1 and T2.

Distances	Change in distance (T2-T1)	
	Mean	SD
Left ECLOS to left ECMOS	−1.80	8.87
Right ECLOS to right ECMOS	−1.81	11.81
Left ECLOI to left ECMOI	0.21	2.94
Right ECLOI to right ECMOI	0.18	3.25
Left FO to left ECLOS	−2.97	12.38
Right FO to right ECLOS	0.73	10.04
Left FO to left ECMOS	−4.37	18.30
Right FO to right ECMOS	−3.39	17.39
Left FR to left ECLOS	0.51	4.61
Right FR to right ECLOS	1.30	5.04
Left FR to left ECMOS	−2.54	12.24
Right FR to right ECMOS	−2.12	11.69
Left HC to left ECLOS	0.53	2.95
Right HC to right ECLOS	1.14	3.85
Left HC to left ECMOS	−1.66	9.82
Right HC to right ECMOS	−1.04	8.73
FM to left ECLOS	0.71	3.29
FM to right ECLOS	0.43	2.87
FM to left ECMOS	−1.48	9.05
FM to right ECMOS	−0.48	3.85
Left ECLOS to left ECLOI	−1.35	12.38
Right ECLOS to right ECLOI	−2.37	14.80
Left ECLOP to left ECLOA	0.27	0.94
Right ECLOP to right ECLOA	0.30	0.99
Left ECMOS to left ECMOI	−1.22	5.22
Right ECMOS to right ECMOI	−1.23	5.19
Left ECMOP to left ECMOA	−0.31	0.63
Right ECMOP to right ECMOA	−0.22	0.71

Table 3: Patient demographics.

	Age at T1 (years)		Age at T2 (years)	
	Mean	SD	Mean	SD
Males (23)	13.6	1.4	16.7	1.4
Females (33)	12.7	1.2	15.5	1.3
Total (56)	13.1	1.5	16	1.3

A systematic review done by Lisboa et al. demonstrated that landmarking the porion presented with a large degree of interevaluator error [18]. Ludlow et al. specifically noted that the porion is difficult to landmark as a result of structure curvature, proximity to the temporal bone, and whether bony or soft-tissue contours were used [10]. While this study defined ear canal landmarks on soft-tissue borders, it is possible that the other factors influenced the variability seen in some of the reliability as well as the distance measurements. This may have caused the large standard deviations found in some of the measurements analyzed. Although average values were low, the large standard deviations showed that in some cases the dimensions reduced. Being this a new area in terms of three-dimensional analysis of the ear canal could not find other references with these results for comparison. It is expected that structures increase in size or become more separate to other structures, but in this case, we suggest to take the changes with caution.

4.1. Limitations. One limitation of this study involves the difficulty of which certain landmarks were defined. Specifically, the medial end of each ear canal was difficult to define due to some variability in CBCT quality, especially within the inner ear. As a result, a landmark was chosen within the Eustachian tube that was simpler to identify consistently. That being said, the different qualities likely resulted in some additional variance in the lateral and medial ear canal landmarks.

Another limitation involves the inability to use certain landmarks for every data set. In particular, the crista galli was not present in 8 of 12 reliability trials, as those CBCTs did not extend superiorly sufficiently enough to capture the landmark.

Another limitation was that the size of the ear canal was determined using only the distance between two 3D end points. A more thorough analysis could examine the volumetric change of the ear canal by providing landmarks from lateral to medial end points.

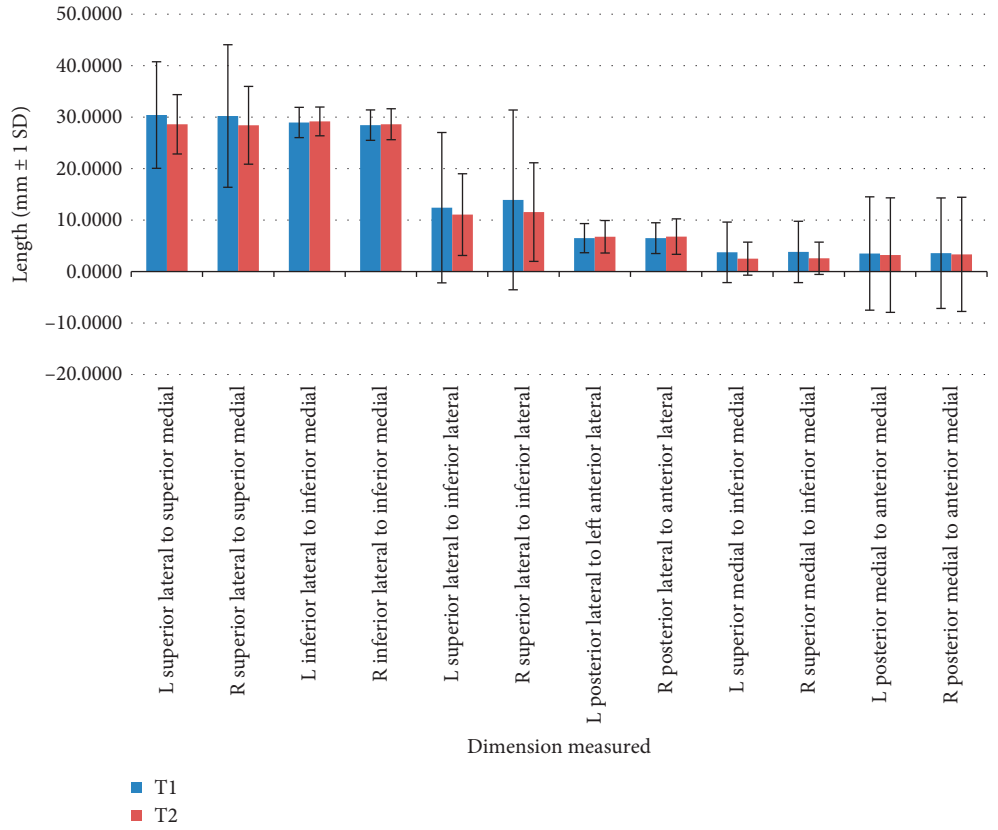

Figure 2: Graphic representation of the major distances in T1 and T2.

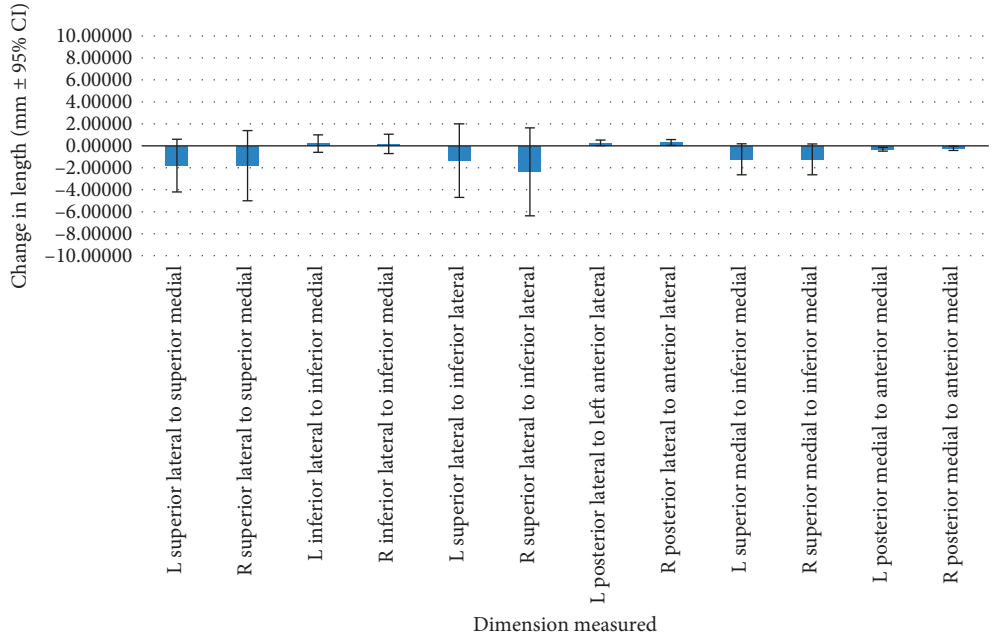

Figure 3: Graphic representation of the change in distances between T1 and T2.

Finally, although the sample size indicated a correct power, more data should be collected in order to completely verify where the changes of the ear canal happen; thus, this should be considered a preliminary analysis.

5. Conclusion

In general, our results suggest that the ear canal presents changes throughout in terms of dimension and relationship

to other structures in the cranial base. Even though in different areas throughout the canal, the average distances were minor, still, large standard deviations were present; thus, caution should be taken when trying to use this structure for superimposition of CBCTs.

Abbreviations

CBCT: Cone-beam computed tomography
2D: Two-dimensional
3D: Three-dimensional.

Data Availability

The data that support the findings of this study are available from the University of Alberta, Orthodontic Program, but restrictions apply to the availability of these data, which were used under license for the current study, and so are not publicly available. Data are however available from the authors upon reasonable request and with permission of the editor.

Ethical Approval

Ethics approval was obtained from the Health Ethics Research Board at the University of Alberta, reference number Pro00044781.

Conflicts of Interest

The authors declare that they have no conflicts of interest.

Authors' Contributions

A. Woods analyzed and interpreted the patient data, developed the measurement tool, and wrote the manuscript. M. Lagravère was his supervisor and mentor in this project and was in charge of obtaining the data and participating in all aspects of this research.

References

[1] S. D. Kapila and J. M. Nervina, "CBCT in orthodontics: assessment of treatment outcomes and indications for its use," *Dentomaxillofacial Radiology*, vol. 44, no. 1, article 20140282, 2015.

[2] L. H. Cevidanes, G. Heymann, M. A. Cornelis, H. J. DeClerck, and J. F. Tulloch, "Superimposition of 3-dimensional cone-beam computed tomography models of growing patients," *American Journal of Orthodontics and Dentofacial Orthopedics*, vol. 136, no. 1, pp. 94–99, 2009.

[3] J. K. Mah, J. C. Huang, and H. Choo, "Practical applications of cone-beam computed tomography in orthodontics," *Journal of the American Dental Association*, vol. 141, pp. 7S–13S, 2010.

[4] D. A. Halazonetis, "From 2-dimensional cephalograms to 3-dimensional computed tomography scans," *American Journal of Orthodontics and Dentofacial Orthopedics*, vol. 127, no. 5, pp. 627–637, 2005.

[5] M. O. Lagravère, M. Secanell, P. W. Major, and J. P. Carey, "Optimization analysis for plane orientation in 3-dimensional cephalometric analysis of serial cone-beam computerized tomography images," *Oral Surgery, Oral Medicine, Oral Pathology, Oral Radiology, and Endodontology*, vol. 111, no. 6, pp. 771–777, 2011.

[6] T. Matsunaga, M. Igarashi, and J. Kanzaki, "Landmark structures to approach the internal auditory canal: a dimensional study related to the middle cranial fossa approach," *Acta Oto-Laryngologica*, vol. 111, no. 487, pp. 48–43, 1991.

[7] L. V. Bonaldi, A. do Lago, L. C. Crema, Y. Fukuda, and R. L. Smith, "Internal auditory canal: pre- and postnatal growth," *Journal of Otolaryngology*, vol. 33, no. 4, pp. 243–247, 2004.

[8] H. Djalilian, K. Thakkar, S. Hamidi, A. G. Benson, and M. F. Mafee, "A study of middle cranial fossa anatomy and anatomic variations," *Ear, Nose & Throat Journal*, vol. 86, no. 8, pp. 474–481, 2007.

[9] S. Toyoda, N. Shiraki, S. Yamada et al., "Morphogenesis of the inner ear at different stages of normal human development," *Anatomical Record*, vol. 298, no. 12, pp. 2081–2090, 2015.

[10] H. Lee, I. Kim, and W. Lee, "New method of identifying the internal auditory canal as seen from the middle cranial fossa approach," *Annals of Otology, Rhinology & Laryngology*, vol. 115, no. 6, pp. 457–460, 2006.

[11] H. Noh and D. H. Lee, "Direct measurement of ear canal volume in a pediatric population: can we explain its individual variation in terms of age and body weight?," *International Journal of Pediatric Otorhinolaryngology*, vol. 76, no. 5, pp. 658–662, 2012.

[12] M. L. Hilgers, W. C. Scarfe, J. P. Scheetz, and A. G. Farman, "Accuracy of linear temporomandibular joint measurements with cone beam computed tomography and digital cephalometric radiography," *American Journal of Orthodontics and Dentofacial Orthopedics*, vol. 128, no. 6, pp. 803–811, 2005.

[13] M. O. Lagravère, J. M. Gordon, I. H. Guedes et al., "Reliability of traditional cephalometric landmarks as seen in three-dimensional analysis in maxillary expansion treatments," *Angle Orthodontist*, vol. 79, no. 6, pp. 1047–1056, 2009.

[14] M. A. Silva, U. Wolf, F. Heinicke, A. Bumann, H. Visser, and E. Hirsch, "Cone-beam computed tomography for routine orthodontic treatment planning: a radiation dose evaluation," *American Journal of Orthodontics and Dentofacial Orthopedics*, vol. 133, no. 5, pp. 640.e1–640.e5, 2008.

[15] S. Kapila, R. S. Conley, and W. E. Harrell Jr., "The current status of cone beam computed tomography imaging in orthodontics," *Dentomaxillofacial Radiology*, vol. 40, no. 1, pp. 24–34, 2011.

[16] J. B. Ludlow, M. Gubler, L. Cevidanes, and A. Mol, "Precision of cephalometric landmark identification: cone-beam computed tomography vs conventional cephalometric views," *American Journal of Orthodontics and Dentofacial Orthopedics*, vol. 136, no. 3, pp. 312-313, 2009.

[17] W. Schlicher, I. Nielsen, J. C. Huang, K. Maki, D. C. Hatcher, and A. J. Miller, "Consistency and precision of landmark identification in three-dimensional cone beam computed tomography scans," *European Journal of Orthodontics*, vol. 34, no. 3, pp. 263–275, 2012.

[18] O. Lisboa Cde, D. Masterson, A. F. da Motta, and A. T. Motta, "Reliability and reproducibility of three-dimensional cephalometric landmarks using CBCT: a systematic review," *Journal of Applied Oral Science*, vol. 23, no. 2, pp. 112–119, 2015.

Hindawi
International Journal of Dentistry
Volume 2018, Article ID 2514243, 7 pages
https://doi.org/10.1155/2018/2514243

Research Article

Accuracy of Periapical Radiography and CBCT in Endodontic Evaluation

R. Lo Giudice,[1] **F. Nicita**,[2] **F. Puleio**,[2] **A. Alibrandi**,[3] **G. Cervino**,[1] **A. S. Lizio**,[2] **and G. Pantaleo**[4]

[1]*Department of Clinical and Experimental Medicine, Messina University, Policlinico G. Martino, Messina, Italy*
[2]*Department of Biomedical and Dental Sciences and Morphofunctional Imaging, Messina University, Messina, Italy*
[3]*Department of Economics, Section of Statistical and Mathematical Sciences, Messina University, Messina, Italy*
[4]*Department of Neurosciences, Reproductive and Odontostomatological Sciences, Naples Federico II University, Naples, Italy*

Correspondence should be addressed to R. Lo Giudice; rlogiudice@unime.it

Received 20 July 2018; Accepted 2 October 2018; Published 16 October 2018

Guest Editor: Anca M. Vitalariu

Introduction. A radiological evaluation is essential in endodontics, for diagnostic purposes, planning and execution of the treatment, and evaluation of the success of therapy. The periapical radiography is nowadays the main radiographic investigations used but presents some limits as 3D anatomic alteration, geometric compression, and possible anatomical structures overlapping that can obscure the area of interest. CBCT (cone beam computed tomography) in endodontics allows a detailed assessment of the teeth and surrounding alveolar anatomy for endodontic diagnosis, treatment planning, and follow-up. *Objective*. The purpose of this study was to evaluate the accuracy of CBCT in comparison with conventional intraoral radiographs used in endodontic procedures. *Materials and Methods*. Statistical analysis was performed on 101 patients with previous endodontic treatments with the relative radiographic documentation (preoperative, postoperative, and follow-up intraoral X-ray) that had underwent at CBCT screening for surgical reasons. The CBCT scans were evaluated independently by two operators and compared with the corresponding periapical images. *Results*. Our analysis shows that the two radiological investigations statistically agree in 100% of cases in the group of patients without any endodontic sign. In the group of patients with an endodontic pathology, detected with CBCT, endodontic under extended treatments (30.6%), MB2 canals in nontreated maxillary molars (20.7%), second canals in nontreated mandibular incisors (9%), root fractures (2.7%), and root resorption (2.7%) were not always visible in intraoral X-ray. Otherwise, positivity in the intraoral X-ray was always confirmed in CBCT. A radiolucent area was detected in CBCT exam in 46%, while the intraoral X-ray exam was positive only in 18%. *Conclusions*. Our study shows that some important radiological signs acquired using CBCT are not always visible in periapical X-ray. Furthermore, CBCT is considered as a II level exam and could be used to solve diagnostic questions, essential to a proper management of the endodontic problems.

1. Introduction

Radiology is essential in endodontics for diagnostic purposes, planning and execution of the treatment, and evaluation of the success of therapy [1].

Until few years ago, the main radiographic investigations used in the endodontic treatment were periapical radiography and, for a general evaluation, orthopantomography.

The conventional radiographic techniques show some limits. These include the following:

(i) *Anatomic 3D compression*. The conventional radiography gives a two-dimensional image, obliging the operator to perform many X-rays with different projections in numerous cases in order to obtain a complete display of the teeth and nearby tissues anatomy [2, 3].

(ii) *Geometric alteration*. For an accurate anatomy reproduction, the image receptor should be parallel to the longitudinal tooth axis and the radiogenic font perpendicular to them. An overangulated or

downangulated radiography reduces or increases the roots' length and the tooth dimension, and it can determine diagnostic omissions of periradicular pathologies [4–6]. The distortion degree of the anatomic structures could range from 3.4% for the periapical radiography to more than 14% for OPT (orthopantomography) [7].

(iii) *Anatomic obstacles*. Some anatomic structures can obscure the area of interest causing a difficult radiological interpretation of the images [8]. So, in the routine clinical practice, there are some cases in which the conventional radiography does not give sufficient information on the pathological conditions, anatomic shapes of the structures, and positional relations.

Ex vivo and in vivo studies confirm that two-dimensional radiology presents clear limits in the periapical lesion diagnoses [9, 10].

One of the factors that highly influence the lesion recognition is bone thickness. Indeed, it has been established that, in an intraoral radiogram, the lesions which involve only the bone medullary component may pass unobserved because of the overhead cortical lines up to the radiolucent area [11–13].

Moreover, two-dimensional images sometimes do not allow to detectthe real number of root canals with consequences on the success rate [14, 15].

The modern systems of digital radiographic imaging introduced relevant improvements in endodontics. The quality of the image is highly important in endodontics because it makes easier the accurate interpretation of the endodontic anatomy, and in particular, the detection of possible canal curvatures, as well as the postoperatory evaluation and long-term result of the endodontic treatment [16–18].

The CBCT permitted a detailed three-dimensional evaluation of the teeth, maxillofacial skeletal district, and relation among anatomical structures [19, 20].

The CBCT in endodontics not only gives a three-dimensional evaluation of the region of interest but also an appropriate resolution of images that allows a detailed analysis of tooth and surrounding alveolar anatomy.

The guidelines of the European Society of Endodontology suggest the use of CBCT in endodontics in limited cases as follows [21]:

(i) Periapical pathology diagnosis in presence of contradictory (not specific) signs and/or symptoms

(ii) To confirm the causes of nonodontogenic pathology

(iii) Maxillofacial trauma evaluation and/or treatment quality

(iv) The extremely complex root canal anatomy evaluation before endodontic orthograde retreatment

(v) The evaluation of the causes of the endodontic failure in surgical endodontic treatment planning

(vi) Evaluation and/or management of radicular resorption.

Therefore, CBCT can be a powerful instrument in endodontic diagnosis, as well as in the treatment planning and follow-up.

At the same time, the decision to expose a patient to a CBCT investigation must be done evaluating risk/benefit ratio in each case, which is determined by the necessity to obtain the optimal endodontic treatment management [22, 23].

The purpose of this study is to compare the accuracy of CBCT imaging with periapical radiographs in the interpretation of clinical endodontic situations.

2. Materials and Methods

2.1. Patient Selection. Our research has been conducted on patients treated between 2015 and 2018 in the Department of Dentistry of Messina University. The selection was performed according to the following inclusion criteria:

(1) Execution of three-dimensional X-ray examination (CBCT) for surgical reasons

(2) Presence of at least one tooth previously endodontically treated, with the relative radiographic documentation (pre- and post-operative intraoral X-ray and the follow-up X-ray between 3 and 6 months)

(3) Radiographic quality of the images adequate for the evaluation of the periapical status of the teeth.

One hundred and one patients satisfied these criteria and have been submitted for further evaluation.

The CBCT images have been done by using an extraoral radiographic hybrid system (MyRay Hyperion X9 Pan/Ceph/CBCT Scanner).

The equipment accomplishes the reconstruction of three-dimensional mold of the volume examined.

Then, the image is transferred to a computer real time and visualized and saved with the iRYS Software.

2.2. Radiographic Evaluation. All the images have been endodontically evaluated separately, by two operators selected as experienced endodontists with more than 10 years of clinical practice and II level master in Endodontics, not directly involved in the patients' treatment planning.

The operators have analyzed each tooth and the periapical structures, highlighting all the images with possible endodontic relevance.

For the CBCT images, the radiolucency should be visible at least in two image plans (0.5 mm thickness).

The CBCT scans have been compared to the corresponding intraoral control X-ray.

For each detected periapical lesion, we evaluated for the following:

(1) Under extended endodontic treatments

(2) Nontreated canals (MB2 canal in maxillary molars and lingual canal in mandibular incisors)

(3) Root fractures

(4) Resorptions.

2.3. Statistical Analysis. The selected patients were divided into two groups:

(i) Patients without endodontic pathology in the radiographic documentation at the end of the endodontic treatment and in CBCT

(ii) Patients with an endodontic pathology in intraoral X-ray and/or CBCT.

All the data have been evaluated through preliminary descriptive analysis.

The clinical-statistical evaluations were relevant to the following:

(i) Absence of lesion in CBCT, Absence of lesion in Rx

(ii) Presence of lesion in CBCT, Absence of lesion in X-ray

(iii) Presence of lesion in CBCT, Presence of lesion in X-ray

(iv) Absence of lesion in CBCT, Presence of lesion in X-ray.

Presence/absence of a periapical radiolucent area and diagnostic concordance between periapical X-ray and CBCT, considering the following the four possible combinations.

The presence of an endodontic pathology or incorrect treatment associated with a periapical radiolucency and the incidence of the diagnostic investigation on the detection of individual clinical situations.

The chi-square test was performed to compare the accuracy of intraoral radiographs and CBCT scans in the detection of periapical lesions and/or endodontic pathologies.

To evaluate diagnostic matching degree between the two instrumental exams, Cohen's kappa coefficient was considered with the following values [24]:

(i) ≤0.2: bad

(ii) 0.21–0.4: sufficient

(iii) 0.41–0.6: not bad

(iv) 0.61–0.8: good

(v) 0.81–1: excellent.

The statistical analysis was conducted by using SPSS 17.0 for Windows operating system. A P value <0.05 was considered statistically significant.

3. Results

The statistical analysis of 111 periapical radiographic images and CBCT showed that signs of endodontic relevance were not present in 34.2% (group A #38). In 65.8% of cases, these signs were observed in the radiological diagnosis exams (group B #73).

In particular, the following diagnostic elements were identified (Table 1):

(i) 34 cases of endodontic under extended treatments (30.6%)

Table 1: Comparison of diagnostic evidences detection between CBCT and intraoral X-ray.

Diagnostic evidences	CBCT	Intraoral Rx	Total (%)
Root fractures	3	/	2.7
Underextended endodontic treatments	34	34	30.6
Internal/external root reabsorption	3	/	2.7
Lack of superior molar's MB2 treatment	23	/	20.7
Lack of a inferior incisor's lingual canal	10	/	9

(ii) 23 cases of MB2 canals nontreated maxillary molars (20.7%) (Figure 1)

(iii) 10 cases of second canals nontreated mandibular incisors (9%)

(iv) 3 cases of root fractures (2.7%)

(v) 3 cases of internal or external root resorption (2.7%).

In group B, 70% of the cases had developed a periapical lesion. The radiolucent area was found in the CBCT exam in 51 cases on 111 (46%), while the endoral X-ray exam was positive only in 20 cases (18%) (Figure 2).

The prevalence of endodontic under extended therapy in the context of the examined trends is 34 cases on 111 (30.06%). In the 100% of cases, there was diagnostic agreement between endoral X-ray and CBCT.

The chi-square test reveals the existence of a perfect statistic concordance between the two diagnostic exams. The K Cohen's coefficient highlights an excellent agreement (1000) among the surveys performed by using endoral X-ray and CBCT.

The distribution of periapical radiolucency detected in association with the correspondent endodontic pathology is summarized in Table 2.

The chi-square test highlights a significant association between the two diagnostic exams in detecting the presence of radiolucent area and under extended endodontic treatments. Moreover, the K Cohen coefficient reports the values 0.411 and 1000, respectively, for periapical lesion and underextended treatments. The data obtained from the two analysis performed are described in Table 3.

4. Discussion

The presence of an apical periodontitis represents an important prognostic factor [25, 26].

However, it was demonstrated that periapical lesions are visible on radiography only when the periapical pathology determines a 30%–50% loss of bone structure [27].

The intraoral images technique shows many evident limitations related to a bidimensional representation of three-dimensional structures and often gives insufficient information about the dimension, extension, and position of the periapical lesion [2].

(a) (b) (c)

Figure 1: Endodontic treatment 1.6. (a) Periapical X-ray: apex endodontic treatment and periapical radiolucency. (b) CBCT sagittal section: apex endodontic treatment MB, untreated MB2, and periapical radiolucency. (c) CBCT transversal section: untreated MB2.

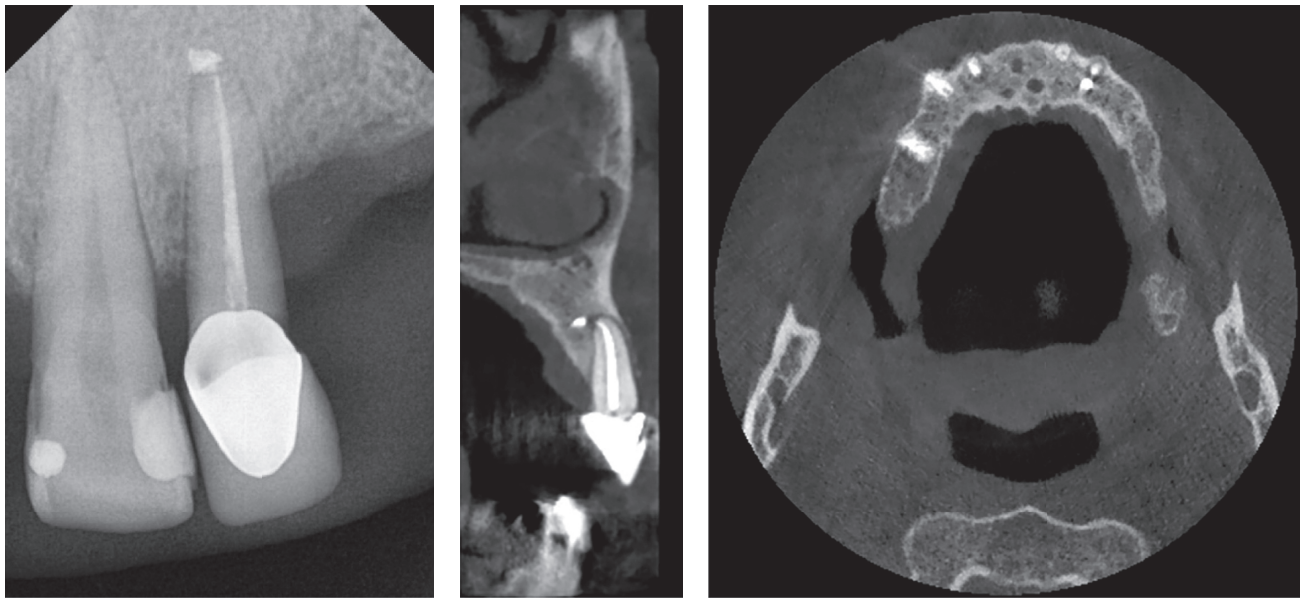

(a) (b) (c)

Figure 2: Endodontic treatment 2.2. (a) Periapical X-ray: endodontic overfilling and no periapical radiolucency. (b) CBCT sagittal cross section: apex endodontic treatment, over filling, and periapical radiolucency. (c) CBCT transversal section: over filling and periapical radiolucency.

Table 2: Comparison periapical lesions detection related to different endodontic and iatrogenic pathologies.

Diagnostic evidences	Periapical lesions (CBCT)	Periapical lesions (X-ray)
Under extended endodontic treatment	31	11
Nontreated MB2 canals	11	5
Nontreated lingual canals	7	4
Root fractures	1	—
Int/ext reabsorption	1	—
Total	51	20

Nowadays, the intraoral examination represents the routine investigation for the diagnosis formulation, the planning of treatment, and the evaluation of success [28].

The introduction of cone beam computed tomography (CBCT) scanning determined important advantages for the diagnosis of endodontic pathology.

Table 3: Statistical analysis: association between CBCT and intraoral Rx results in diagnosis of radiolucent areas and under-extended treatments.

	Pearson's chi-square	Cohen's kappa
Radiolucent area	28.701/0.000	0.411/0.000
Under-extended treatments	111.000/0.000	1/0.000

Our descriptive analysis shows that the two radiological investigations (CBCT and intraoral X-ray) agree in 100% of cases in the group of patients without any endodontic sign (A group).

However, the presence of an endodontic pathology or an incorrect treatment, associated or not to a periapical radiolucency, was not always visible in intraoral X-ray.

On the contrary, positivity in the periapical X-ray was always detectable in CBCT. This fact is confirmed by recent studies which showed how CBCT gives more accurate information in the survey of endodontic signs [29–31], avoiding anatomic structure overlapping [32, 33].

Our research points out that the periapical lesions detected in the context of all the examined CBCT scans are 51 cases. Only in 20 cases the diagnostic agreement was recorded between the two instrumental exams. Even Cheung et al. and Venskutonis et al. reported, respectively, an improvement of 63% and of 57.1% on the periapical lesions quality detection with CBCT [31, 34].

In addition, Cohen's kappa coefficient shows a decent agreement between the endoral X-ray and CBCT surveys, in spite of a relevant percentage of diagnostic discordance (27.9%).

Therefore, although CBCT is obviously more reliable in identifying signs of endodontic relevance than conventional radiography, the latter retains an effective validity.

In vitro studies have shown the greater reliability of CBCT images compared to conventional endoral X-ray in the pathology diagnosis of endodontic relevance such as root fracture, root perforation, and resorption [8, 30, 35, 36].

Our study highlights that, only in CBCT, scans are detected: root fractures (2.7%) and resorption (2.7%).

Regarding the iatrogenic errors, we have noticed the missing treatment of MB2 (20.7%) and the lingual canal of the lower incisors (9%).

In case of underextended endodontic therapies, there is a total diagnostic agreement between endoral X-ray and CBCT.

Our analysis shows that endodontic underextended treatments are more frequently associated with a periapical lesion than other endodontic diseases (31 out of 51 cases). Furthermore, some radiolucent lesions associated with no treatment of MB2 and/or mandibular incisors' lingual canal are also evident in the X-ray, despite the presence of the untreated canals which has been ascertained only in CBCT scans.

5. Conclusions

Our research shows that many of the endodontic signs obtained from the analysis of CBCT images are not resulted in the corresponding intraoral radiographs. The use of two-dimensional radiology therefore shows clear limits that can be overcome by 3D examinations.

Cone beam is therefore indispensable in all those cases in which a discrepancy between the clinical examination and the diagnostic evidence that can be objected to the intraoral radiographic examination is observable.

To perform a 3D examination, it is essential that the radiation dose is kept "at the lowest level reasonably obtainable" and that the FOV is limited only to the region of interest [37, 38].

However, the use of intraoral radiographs in different projections may increase the possibility of a correct diagnosis compared to a single radiograph.

Consequently, the CBCT remains a second level survey to be used adequately exploiting the system potential (correct FOV settings, mAs, appropriate kVp, and selection of the definition parameters) according to the ALADA concept (dosage as low as acceptable from the point of diagnostic view).

Data Availability

The data used to support the findings of this study are available from the corresponding author upon request.

Conflicts of Interest

The authors declare that there are no conflicts of interest.

References

[1] C. Reit, K. Petersson, and O. Molven, *Diagnosis of Pulpal and Periradicular Disease. Textbook of Endodontology,* pp. 9–18, Blackwell Publishing Ltd., Oxford, UK, 1st edition, 2003.

[2] P. Velvart, H. Hecker, and G. Tillinger, "Detection of the apical lesion and the mandibular canal in conventional radiography and computed tomography," *Oral Surgery, Oral Medicine, Oral Pathology, Oral Radiology, and Endodontology*, vol. 92, no. 6, pp. 682–688, 2001.

[3] G. Lo Giudice, V. Nigrone, A. Longo, and M. Cicciù, "Supernumerary and supplemental teeth: case report," *European Journal of Paediatric Dentistry*, vol. 9, no. 2, pp. 97–101, 2008.

[4] J. Forsberg and A. Halse, "Radiographic simulation of a periapical lesion comparing the paralleling and the bisecting-angle techniques," *International Endodontic Journal*, vol. 27, no. 3, pp. 133–138, 1994.

[5] G. Lo Giudice, F. Lipari, A. Lizio, G. Cervino, and M. Cicciù, "Tooth fragment reattachment technique on a pluri traumatized tooth," *Journal of Conservative Dentistry*, vol. 15, no. 1, pp. 80–83, 2012.

[6] G. Lo Giudice, A. Alibrandi, F. Lipari et al., "The coronal tooth fractures: preliminary evaluation of a three-year follow-up of the anterior teeth direct fragment reattachment technique without additional preparation," *Open Dentistry Journal*, vol. 11, no. 1, pp. 266–275, 2017.

[7] F. Lazzerini, D. Minorati, R. Nessi, M. Gagliani, and C. M. Uslenghi, "The measurement parameters in dental radiography: a comparison between traditional and digital techniques," *La Radiologia Medica*, vol. 91, pp. 364–369, 1996.

[8] S. B. Paurazas, J. R. Geist, F. E. Pink, M. M. Hoen, and H. R. Steiman, "Comparison of diagnostic accuracy of digital

imaging by using CCD and CMOS-APS sensors with E-speed film in the detection of periapical bony lesions," *Oral Surgery, Oral Medicine, Oral Pathology, Oral Radiology, and Endodontology*, vol. 89, no. 3, pp. 356–362, 2000.

[9] E. G. Jorge, M. Tanomaru-Filho, M. Gonvalves, and J. M. Tanomaru, "Detection of periapical lesion development by conventional radiography or computed tomography," *Oral Surgery, Oral Medicine, Oral Pathology, Oral Radiology, and Endodontology*, vol. 106, no. 1, pp. e56–e61, 2008.

[10] F. W. G. Paula-Silva, M.-K. Wu, M. R. Leonardo, L. A. B. da Silva, and P. R. Wesselink, "Accuracy of periapical radiography and cone beam computed tomography in diagnosing apical periodontitis using histopathological findings as a gold standard," *Journal of Endodontics*, vol. 35, no. 7, pp. 1009–1012, 2009.

[11] S. Patel, A. Dawood, F. Mannocci, R. Wilson, and T. Pitt Ford, "Detection of periapical bone defects in human jaws using cone beam computed tomography and intraoral radiography," *International Endodontic Journal*, vol. 42, no. 6, pp. 507–515, 2009.

[12] P. Tsai, M. Torabinejad, D. Rice, and B. Azevedo, "Accuracy of cone-beam computed tomography and periapical radiography in detecting small periapical lesions," *Journal of Endodontics*, vol. 38, no. 7, pp. 965–970, 2012.

[13] Y. Gao, M. Haapasalo, Y. Shen, H. Wu, H. Jiang, and X. Zhou, "Development of virtual simulation platform for investigation of the radiographic features of periapical bone lesion," *Journal of Endodontics*, vol. 36, no. 8, pp. 1404–1409, 2010.

[14] S. Patel, "New dimensions in endodontic imaging: part 2. Cone beam computed tomography," *International Endodontic Journal*, vol. 42, no. 6, pp. 463–475, 2009.

[15] Q.-H. Zheng, Y. Wang, X.-D. Zhou, Q. Wang, G.-N. Zheng, and D.-M. Huang, "A cone-beam computed tomography study of maxillary first permanent molar root and canal morphology in a Chinese population," *Journal of Endodontics*, vol. 36, no. 9, pp. 1480–1484, 2010.

[16] K. H. Versteeg, G. C. Sanderink, F. C. van Ginkel, and P. F. van der Stelt, "Estimating distances on direct digital images and conventional radiographs," *Journal of American Dental Association*, vol. 128, no. 4, pp. 439–443, 1997.

[17] Z. Mohammadi, L. Giardino, F. Palazzi et al., "Effect of sodium hypochlorite on the substantivity of chlorhexidine," *International Journal of Clinical Dentistry*, vol. 6, no. 2, pp. 173–178, 2013.

[18] G. Lo Giudice, A. Lizio, R. Lo Giudice et al., "The effect of different cleaning protocols on post space: a SEM study," *International Journal of Dentistry*, vol. 2016, Article ID 1907124, 7 pages, 2016.

[19] H. M. Pinsky, S. Dyda, R. W. Pinsky, K. A. Misch, and D. P. Sarament, "Accuracy of three-dimensional measurements using CBCT," *Dentomaxillofacial Radiology*, vol. 35, no. 6, pp. 410–416, 2006.

[20] G. Lo Giudice, G. Iannello, A. Terranova, R. Lo Giudice, G. Pantaleo, and M. Cicciù, "Transcrestal sinus lift procedure approaching atrophic maxillary ridge: a 60-month clinical and radiological follow-up evaluation," *International Journal of Dentistry*, vol. 2015, Article ID 261652, 8 pages, 2015.

[21] S. Patel, C. Durack, F. Abella et al., "European society of endodontology position statement: the use of CBCT in endodontics," *International Endodontic Journal*, vol. 47, no. 6, pp. 502–504, 2014.

[22] S. Patel, C. Durack, F. Abella, H. Shemesh, M. Roig, and K. Lemberg, "Cone beam computed tomography in endodontics—a review," *International Endodontic Journal*, vol. 48, pp. 3–15, 2015.

[23] M. M. Bornstein, R. Lauber, P. Sendi, and T. von Arx, "Comparison of periapical radiography and limited cone-beam computed tomography in mandibular molars for analysis of anatomical landmarks before apical surgery," *Journal of Endodontics*, vol. 37, no. 2, pp. 151–157, 2011.

[24] D. G. Altman, *Practical Statistics for Medical Research*, Chapman & Hall/CRC, London, UK, 1991.

[25] S. Patel, R. Wilson, A. Dawood, F. Foschi, and F. Mannocci, "The detection of periapical pathosis using digital periapical radiography and cone beam computed tomography-part 2: a 1-year post-treatment follow-up," *International Endodontic Journal*, vol. 45, no. 8, pp. 711–723, 2012.

[26] G. Lo Giudice, G. Matarese, A. Lizio et al., "Invasive cervical resorption: a case series with 3-year follow-up," *International Journal of Periodontics and Restorative Dentistry*, vol. 36, no. 1, pp. 102–109, 2016.

[27] I. B. Bender and S. Seltzer, "Roentgenographic and direct observation of experimental lesions in bone. Part I," *Journal of American Dental Association*, vol. 62, no. 2, pp. 152–160, 1961.

[28] D. A. Tyndall and S. Rathore, "Cone-beam CT diagnostic applications: caries, periodontal bone assessment, and endodontic applications," *Dental Clinics of North America*, vol. 52, no. 4, pp. 825–841, 2008.

[29] M. B. Vizzotto, P. F. Silveira, N. A. Arús, F. Montagner, B. P. Gomes, and H. E. da Silveira, "CBCT for the assessment of second mesiobuccal (MB2) canals in maxillary molar teeth: effect of voxel size and presence of root filling," *International Endodontic Journal*, vol. 46, no. 9, pp. 870–876, 2013.

[30] C. Durack, S. Patel, J. Davies, R. Wilson, and F. Mannocci, "Diagnostic accuracy of small volume cone beam computed tomography and intraoral periapical radiography for the detection of simulated external inflammatory root resorption," *International Endodontic Journal*, vol. 44, no. 2, pp. 136–147, 2011.

[31] G. S. Cheung, W. L. Wei, and C. McGrath, "Agreement between periapical radiographs and cone-beam computed tomography for assessment of periapical status of root filled molar teeth," *International Endodontic Journal*, vol. 46, no. 10, pp. 889–895, 2013.

[32] K. M. Low, K. Dula, W. Bürgin, and T. von Arx, "Comparison of periapical radiography and limited cone-beam tomography in posterior maxillary teeth referred for apical surgery," *Journal of Endodontics*, vol. 34, no. 5, pp. 557–562, 2008.

[33] E. Soğur, H. G. Gröndahl, B. G. Baksı, and A. Mert, "Does a combination of two radiographs increase accuracy in detecting acid-induced periapical lesions and does it approach the accuracy of cone-beam computed tomography scanning?," *Journal of Endodontics*, vol. 38, no. 2, pp. 131–136, 2012.

[34] T. Venskutonis, P. Daugela, M. Strazdas, and G. Juodzbalys, "Accuracy of digital radiography and cone beam computed tomography on periapical radiolucency detection in endodontically treated teeth," *Journal of Oral and Maxillofacial Research*, vol. 5, no. 2, p. e1, 2014.

[35] M. Varshosaz, M. A. Tavakoli, M. Mostafavi, and A. A. Baghban, "Comparison of conventional radiography with cone beam computed tomography for detection of vertical root fractures: an in vitro study," *Journal of Oral Science*, vol. 52, no. 4, pp. 593–597, 2010.

[36] T. Venskutonis, G. Juodzbalys, O. Nackaerts, and L. Mickevicienė, "Influence of voxel size on the diagnostic ability of cone-beam computed tomography to evaluate

simulated root perforations," *Oral Radiology*, vol. 29, no. 2, pp. 151–159, 2013.

[37] ICRP, "Publication 103: the 2007 recommendations of the international commission on radiological protection," *Annals of ICRP*, vol. 37, no. 2–4, pp. 1–332, 2007.

[38] SEDENTEXCT, *European Commission, Radiation Protection N 172: Cone Beam CT for Dental and Maxillofacial Radiology. Evidence based Guidelines*, SEDENTECT Project, Luxembourg, Europe, 2012.

Hindawi
International Journal of Dentistry
Volume 2018, Article ID 4927503, 7 pages
https://doi.org/10.1155/2018/4927503

Research Article

Development and Validation of 3D Finite Element Models for Prediction of Orthodontic Tooth Movement

Udomsak Likitmongkolsakul,[1] **Pruittikorn Smithmaitrie**,[2] **Bancha Samruajbenjakun**,[1] **and Juthatip Aksornmuang**[3]

[1]*Orthodontic Section, Department of Preventive Dentistry, Faculty of Dentistry, Prince of Songkla University, Hat Yai, Songkhla, Thailand*
[2]*Department of Mechanical Engineering, Faculty of Engineering, Prince of Songkla University, Hat Yai, Songkhla, Thailand*
[3]*Prosthodontic Section, Department of Conservative Dentistry, Faculty of Dentistry, Prince of Songkla University, Hat Yai, Songkhla, Thailand*

Correspondence should be addressed to Juthatip Aksornmuang; juthatip.a@gmail.com

Received 9 May 2018; Revised 10 July 2018; Accepted 29 July 2018; Published 30 August 2018

Academic Editor: Predrag Vucinic

Objectives. The aim of this study was to develop and validate three-dimensional (3D) finite element modeling for prediction of orthodontic tooth movement. *Materials and Methods*. Two orthodontic patients were enrolled in this study. Computed tomography (CT) was captured 2 times. The first time was at T_0 immediately before canine retraction. The second time was at T_4 precisely at 4 months after canine retraction. Alginate impressions were taken at 1 month intervals (T_0–T_4) and scanned using a digital scanner. CT data and scanned models were used to construct 3D models. The two measured parameters were clinical tooth movement and calculated stress at three points on the canine root. The calculated stress was determined by the finite element method (FEM). The clinical tooth movement was measured from the differences in the measurement points on the superimposed model. Data from the first patient were used to analyze the tooth movement pattern and develop a mathematical formula for the second patient. Calculated orthodontic tooth movement of the second patient was compared to the clinical outcome. *Results*. Differences between the calculated tooth movement and clinical tooth movement ranged from 0.003 to 0.085 mm or 0.36 to 8.96%. The calculated tooth movement and clinical tooth movement at all reference points of all time periods appeared at a similar level. Differences between the calculated and clinical tooth movements were less than 0.1 mm. *Conclusion*. Three-dimensional FEM simulation of orthodontic tooth movement was achieved by combining data from the CT and digital model. The outcome of the tooth movement obtained from FEM was found to be similar to the actual clinical tooth movement.

1. Introduction

Orthodontic tooth movement has been routinely practiced in clinics, but the orthodontic treatment force is largely unknown. Knowledge of the biomechanical changes in the loaded tissues and the mechanisms of tissue response on an applied force are difficult to study because the stress/strain in a periodontal ligament cannot be measured directly and must be derived from mathematical models.

An initial study attempted to relate tooth movement to an applied force by developing a simple theory that assumed that the force is a constant value with imprecise experimental techniques on human subjects [1]. Other studies in tooth movement and properties of the periodontium were animal experiments [2–8]. This approach has limitations to explain the biomechanics of tooth movement in humans because animal tissues often produce morphological and biomechanical changes unlike human tissues. The development of tissue culture systems to determine the effects of stress on osteoblast cells was reported [9]. Finding the effects of stress at the cellular level has driven much research in an attempt to understand the mechanisms of cell reaction in the

process of tooth movement. Several published papers on this issue can be found during the last decade [9–11]. The linking of an application of a continuous load on a tooth crown in an orthodontic force all the way down to the cellular response may provide a much clearer picture to the clinician and improve the biomechanical understanding of the resultant local stress/strain. The methods to study the biomechanics of tooth movement include theoretical mathematical techniques [12], photoelastic systems [13], and laser holographic interferometry [14]. Some methods were effective in predicting the tissue response from the applied load. However, some were ineffective because they examined only the surface stress and were not well validated. Clinically, the observation time of the tooth movement was too long to describe the biomechanics of stress and strain in orthodontics. Besides, the biological cell response in humans has individual variations. Recently, the finite element method (FEM), which was originally used in structural analysis, has been applied in dental biomechanical predictions [15, 16]. The FEM has been used to solve stress-strain problems in the mechanics of solids and structures. This analysis technique has been adopted to study biomaterials and human structures as well. Thus, the biomechanics of orthodontic tooth movement can be analyzed by this method. Although clinical validation of the FEM in orthodontic tooth movement is necessary, it has not been previously reported. The aim of this study was to develop and validate the prediction of three-dimensional (3D) finite element modeling of orthodontic tooth movement.

2. Materials and Methods

Two patients were enrolled in this study. They were 18 and 20 years old and attended the Orthodontic Clinic, Faculty of Dentistry, Prince of Songkla University. Orthodontics patients from our clinic, who meet the inclusion criteria and had not previously received any orthodontic therapy, were enrolled in this study. The inclusion criteria were good general health, no medical problems, no signs or symptoms of temporomandibular dysfunction, good oral hygiene, and probing depth values of the entire dentition less than 3 mm. Patients had to be diagnosed as skeletal Class I bimaxillary dentoalveolar protrusion and normodivergent pattern with a plan to extract the maxillary and mandibular first premolars and distalize the canines. The absolute maximum anchorage situation was determined. The research protocol was approved by the Research Ethics Committee of the Faculty of Dentistry, Prince of Songkla University (Project No. EC5804-10-P-HR). For each patient, Roth's prescription preadjusted edgewise brackets (Ormco Corporation, Glendora, CA, USA) with 0.018×0.025-inch slots were attached on the incisors, 0.022×0.028-inch slots were attached on the posterior teeth, and self-ligating brackets (Ormco Corporation, Glendora, CA, USA) with 0.022×0.028-inch slots were attached on the canines after extraction of the first premolars. For anchorage preparation, temporary skeletal anchorage devices (Dentos, Daegu, Korea) were placed on the attached gingiva between the second premolar and first molar. The second premolar through the second molar were tied together with 0.010-inch stainless steel wire and bound with 0.016×0.022-inch stainless steel wire to passively engage the tubes and slots of the edgewise appliances. The wires were left in situ for 1 month to become passive before starting to retract the canines. The mechanics for canine distalization consisted of a NiTi-based closed-coil spring (Dentos, Light, Daegu, Korea) tied between the canine and temporary skeletal anchorage device. The NiTi coil springs were activated to obtain 100 grams of force. Each canine was retracted for 4 months. The patients were scheduled for visits every month. At each appointment during the experimental period, the NiTi coil spring was checked and adjusted to ensure that the level of the force was at 100 grams.

For construction of the 3-dimensional model, the patient's head image was captured 2 times with low-dose dental computed tomography (CT) using a Veraviewepocs (Morita, Tokyo, Japan). The first CT image at T_0 was taken immediately before canine retraction and the last CT image at T_4 was taken after canine retraction precisely at 4 months. The dental CT scan at T_0 was saved in DICOM format and later converted to an initial model. The model between the mesial of the lateral incisor and mesial of the second premolar area included the maxilla, alveolar bone, periodontal ligament, lateral incisor, canine, second premolar, bracket, main archwire, and the temporary skeletal anchorage device. It was constructed by 3D image processing and editing software (ITK-SNAP open-source software). The 3D model of the canines was sectioned into buccal and palatal sides. The root was divided at one-third and two-thirds of the root length. Three points were defined as C1D, C2D, and C1M. C1D and C2D points were on the distal surface of the tooth at one-third and two-thirds coronal to the root, respectively. The C1M point was on the mesial surface of the tooth at one-third coronal to the root (Figure 1).

At each appointment (T_0–T_4), alginate impressions were taken to determine the amount of tooth movement. The models were then scanned using a calibrated digital scanner (R700 Orthodontic 3D Scanner, 3 Shape, Copenhagen, Denmark).

The T_1 constructed model was generated from individually constructed tooth models and periodontal ligament models from the T_0 superimposed over the T_1 scanned dental model based on the best-fit method at the area of palatal side using 3D image processing software (Geomagic Wrap software; www.geomagic.com) (Figure 2). Maxilla from T_0 was simultaneously adjusted to the new position of canine and periodontal ligament. The T_2 and T_3 constructed models were generated with the same method. Finally, the T_4 constructed model was generated from the T_4 dental CT following the T_0 model technique. The T_0, T_1, T_2, and T_3 constructed models were saved in STL format.

To analyze the 3D solid model, the program required the numerical dimensions of the object, and it must be able to visualize how these dimensions relate to lines and curves. Constructed models were used to generate finite element mesh and exported as a mesh model. The T_0, T_1, T_2, and T_3 constructed models were meshed by finite element analysis preprocess and postprocess software (MSC Patran; MSC Software, Inc., USA). The tetrahedral element was used in

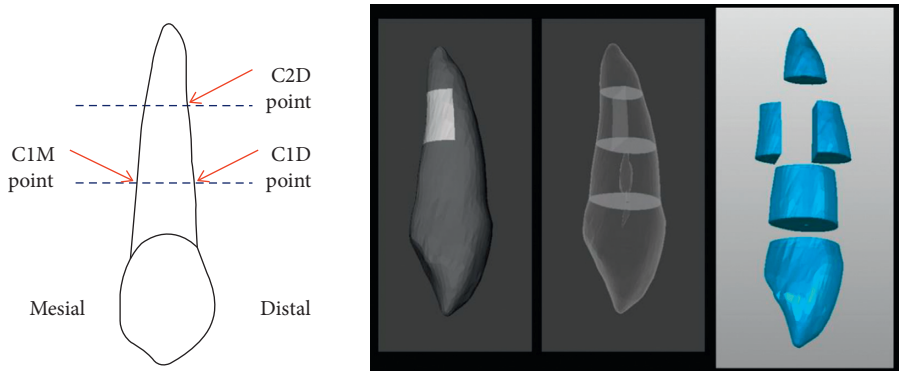

Figure 1: Measurement landmarks in the canine model.

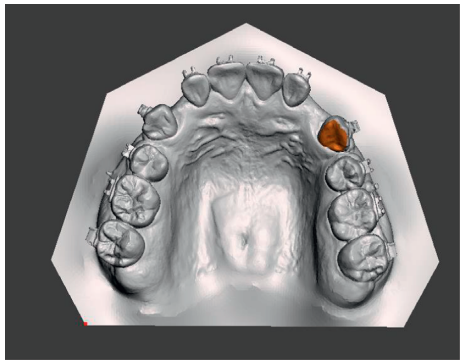

Figure 2: Superimposition of the constructed tooth model and the scanned model using the palatal side of the teeth.

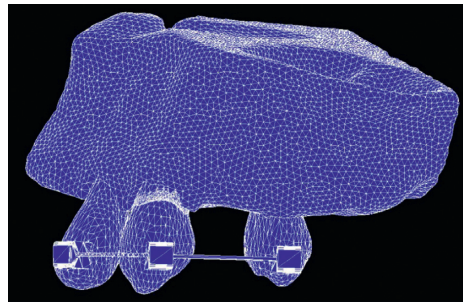

Figure 3: The mesh model of the maxilla, alveolar bone, periodontal ligament, lateral incisor, canine, second premolar, bracket, and main archwire.

mesh generation. The resultant volumetric model consisted of approximately 100,000 elements and 170,000 nodes (Figure 3). The mesh model was imported into the 3D finite element software (MSC Marc; MSC Software, Inc., USA). Mechanical properties of each tissue and materials are shown in Table 1. The model imitated the clinical situation by applying force at the canine bracket. The direction was set to the temporary skeletal anchorage device in the mesh model, and the magnitude was 100 grams of force. The boundary condition between bracket and wire was touch contacted that the bracket can slide along the archwire. The program calculated stress from the effect of applied force, boundary conditions, and mechanical properties of each tissue.

The two measured parameters were clinical tooth movement and calculated stress at the C1D, C2D, and C1M points. Clinical tooth movement was determined from the difference of the measurement points on the superimposed model. The distance measurements were repeated at 2-week intervals. The method error was calculated using Dahlberg's formula [17]. The stress was determined by the FEM. The 3D models and analyses in each period are shown in Figure 4. To create a formula for the prediction of tooth movement, data from the first patient were used to analyze the tooth movement pattern. Data of tooth movement in each visit were plotted showing the relationship between tooth movement and stress. All data and stress from the finite element model of the first patient were used to create the pattern prediction formula which was subsequently used in the second patient.

The dental CT data and the scanned dental model of the other patient were processed with the same method as the first patient. The formula from the first patient was used to calculate the orthodontic tooth movement which was then compared with the clinical outcome.

3. Results and Discussion

The results of the calculated stress and clinical tooth movement obtained from the first patient are shown in Table 2. The ranges of the calculated stress and clinical tooth movement were 0.028 to 0.063 MPa and 0.194 to 1.378 mm, respectively. The data from the calculated stress and clinical tooth movement were plotted (Figure 5). The relationship between the calculated stress and clinical tooth movement was matched to a quadratic trend. The fitting formula can be written as Equation (1), where Y is the tooth movement (mm) and X is the stress (N/mm^2):

$$Y = 2960X^2 - 254.56X + 5.667. \quad (1)$$

The results of the calculated stress, calculated tooth movement, and clinical tooth movement of the second patient are shown in Table 3. The results revealed that the range of calculated stress, calculated tooth movement, and clinical tooth movement were 0.030 to 0.063 MPa, 0.206 to 1.378 mm, and 0.219 to 1.296 mm, respectively. The differences between the calculated tooth movement and clinical

Table 1: Mechanical properties of the materials.

Tissue	Material	Young's modulus (N/mm^2)	Poisson's ratio
Maxilla	Cortical bone	13,800	0.26
	Cancellous bone	345	0.31
Lateral incisor Canine Second premolar	Tooth	20,000	0.15
Periodontal ligament	Periodontal ligament	0.68	0.49
Bracket Main archwire	Stainless steel	210,000	0.30

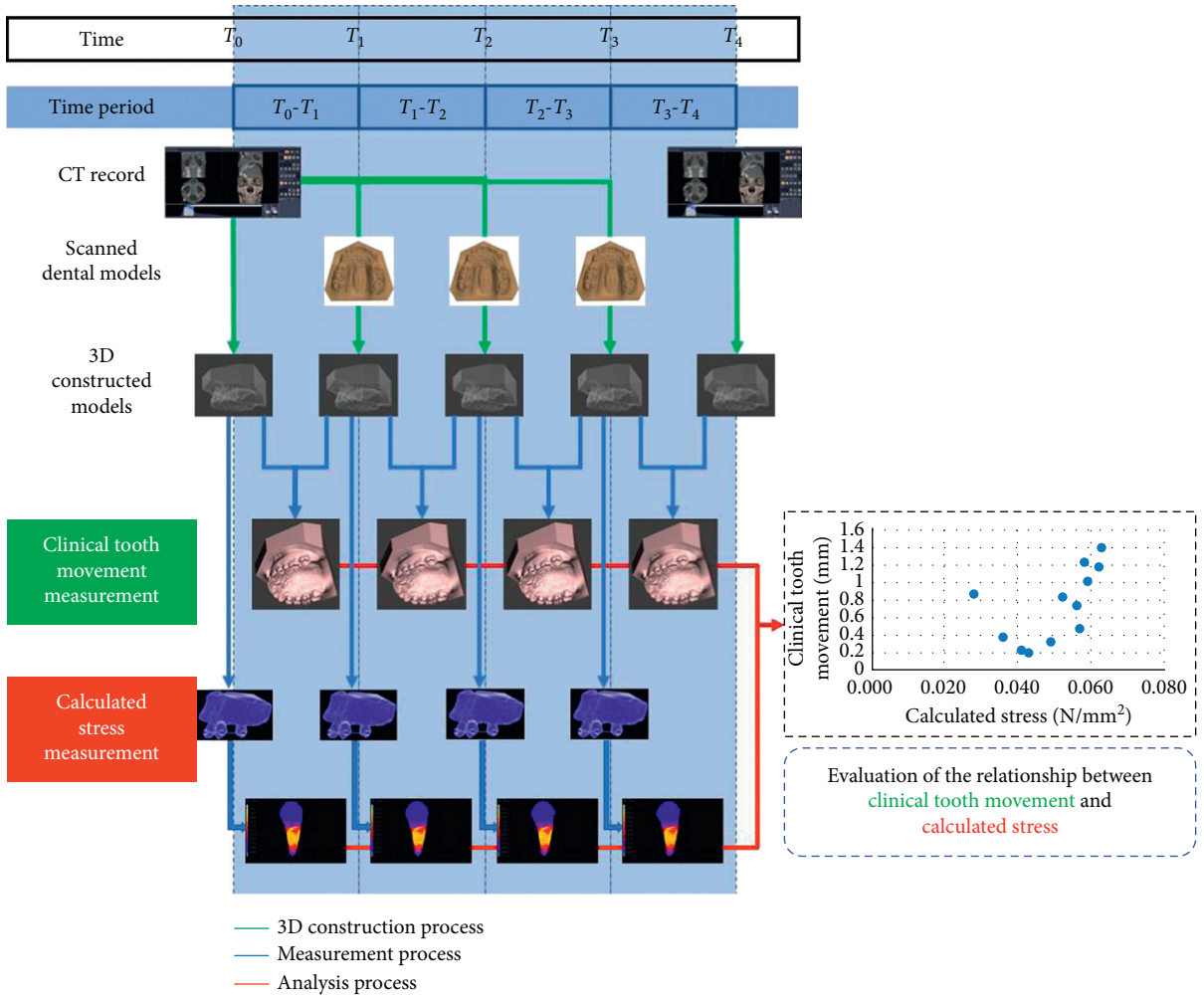

Figure 4: Overview of the experimental steps and measurements.

tooth movement ranged from 0.003 to 0.085 mm or 0.36 to 8.96%. The calculated tooth movement and clinical tooth movement at all reference points of all time periods appeared to be at similar levels. Differences in the values were less than 0.1 mm. The data from the calculated stress and clinical tooth movement were plotted (Figure 6).

Orthodontic tooth movement of the first patient was studied and simulated to develop a mathematical formula to represent the relationship between stress and the amount of tooth movement. Orthodontic tooth movement of the second patient was predicted using the formula from the first patient and then compared with the clinical outcome.

Two patients with absolute maximum anchorage were included in this study. Therefore, a skeletal anchorage device was used to reduce the complexity of mimicking the orthodontic tooth model. The first point of loading was fixed at the skeletal anchorage device. The loading force and direction were therefore virtually stable between each month. In addition, the skeletal anchorage device was employed as a landmark in the superimposition process and for the

Table 2: Calculated stress and clinical tooth movement of the first orthodontic patient.

Point	Time	Calculated stress (N/mm^2)	Time	Clinical tooth movement (mm)
C1M		0.062		1.153
C1D	T_0	0.059	$T_{0\text{-}1}$	1.003
C2D		0.041		0.221
C1M		0.058		1.221
C1D	T_1	0.063	$T_{1\text{-}2}$	1.378
C2D		0.043		0.194
C1M		0.052		0.827
C1D	T_2	0.056	$T_{2\text{-}3}$	0.723
C2D		0.028		0.859
C1M		0.057		0.464
C1D	T_3	0.049	$T_{3\text{-}4}$	0.321
C2D		0.036		0.367

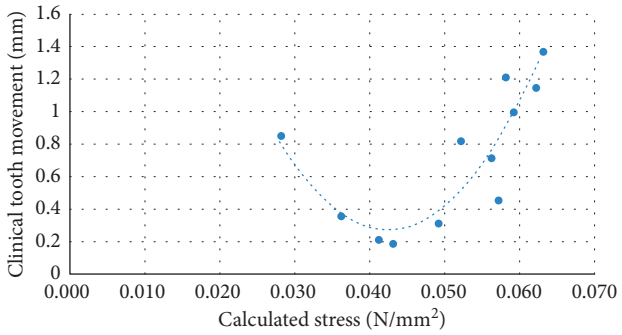

Figure 5: Relationship between the calculated stress and clinical tooth movement of the first orthodontic patient.

measurements. The NiTi-based closed-coil spring was attached to distalize the canine. Since the properties of NiTi generated a continuous force with a low decay rate [18], the magnitude of force could be controlled at each visit. Our previous study proved that 3D constructed models could be accurately created using the scanned plaster dental model combined with the original CT scan data [19]. To reduce the CT dose, T_1, T_2, and T_3 were therefore evaluated using only the impression method.

The canine model was segmented into six pieces to reduce systematic error in the measurements. The measurement landmarks were at the point angles of the segments. Our previous experiment was performed to validate landmarks of the 3D model [19]. The results showed that the segmental tooth model was effective for evaluating the tooth position. In this study, Dahlberg's error of distance measurement was less than 0.001 mm. The results of this study confirmed that the segmented model could improve reproducibility and generate less error.

The results in Table 2 show that the stress ranged from 0.028 to 0.063 MPa. In a study by Rudolph et al., a force of 0.25 N was used to tip the upper central incisor. The results found that the maximum stress was 0.00245 MPa at the cervical area and approximately 0.00765 to 0.00122 MPa in the one-third to two-thirds area [20]. In another previous study that used a force of 0.5 N, stress in the crestal bone was found to range from 0.0187 to 0.0560 MPa [21]. The results of stress in this study were higher than those of the previous studies due to the higher force used. A force magnitude of 1 N was applied in the present experiment which was 2 to 4 times higher than the previous experiments. The finite element model in this study was composed of more than 170,000 nodes and 100,000 elements (10-node quadratic tetrahedron). The model consisted of cortical bone, cancellous bone, tooth, and periodontal ligament which could represent the shape and type of each tissue similar to the real situation.

A previous study reported that stress was found to be a factor that affected tooth movement [22]. Kojima et al. reported the equations between stress and bone resorption to demonstrate tooth movement through the alveolar bone [23]. This present study revealed the relationship between stress and tooth movement directly and the relationship was validated by the clinical outcome. The relationship between stress and tooth movement is represented by the plot shown in Figure 5. It was found that the relationship between stress and tooth movement was nonlinear as demonstrated in previous studies [24–26]. Tooth movement initially occurred at a low level of stress. The rate of tooth movement decreased until it passed the stress threshold and then the tooth movement increased rapidly (Figure 5). This can be described by the pressure-tension theory; that is, the optimal force could activate the biological mechanism and then the tooth would move [27, 28]. As the stress increased, blood flow would consequently decrease. Blood flow serves as the source of mediation in biological mechanisms. The amount of tooth movement therefore decreased in the middle of the movement pattern. If the stress continuously increased, blood flow would be cut-off and the tissue adjacent to this area would become necrotic. A biological mechanism would also occur in the alveolar bone and the amount of tooth movement would increase based on the extent of the necrotic zone. However, the side effects of a high magnitude of force, such as root resorption, could not be simulated in this study.

The differences between the predicted tooth movement and clinical tooth movement of the second orthodontic patient ranged from 0.03 to 0.086 mm or 0.36 to 8.95%. The data obtained from the calculated tooth movement were found to be allied with the clinical tooth movement. However, the prediction of tooth movement by this method is suitable for a one-month period. A series of prediction

Table 3: Calculated stress, calculated tooth movement, and clinical tooth movement of the second orthodontic patient.

Point	Time	Calculated stress (N/mm^2)	Time	Calculated tooth movement (F) (mm)	Clinical tooth movement (C) (mm)	Difference ($\lvert F-C \rvert$) (mm (%))
C1M		0.063		1.378	1.296	0.082 (5.95)
C1D	T_0	0.061	$T_{0\text{-}1}$	1.153	1.211	0.058 (5.03)
C2D		0.039		0.241	0.223	0.018 (7.61)
C1M		0.062		1.263	1.258	0.005 (0.36)
C1D	T_1	0.059	$T_{1\text{-}2}$	0.952	1.037	0.085 (8.96)
C2D		0.041		0.206	0.219	0.013 (6.39)
C1M		0.053		0.490	0.487	0.003 (0.61)
C1D	T_2	0.051	$T_{2\text{-}3}$	0.383	0.395	0.012 (3.01)
C2D		0.048		0.268	0.272	0.004 (1.49)
C1M		0.030		0.694	0.674	0.020 (2.92)
C1D	T_3	0.031	$T_{3\text{-}4}$	0.620	0.630	0.010 (1.57)
C2D		0.034		0.434	0.451	0.017 (3.97)

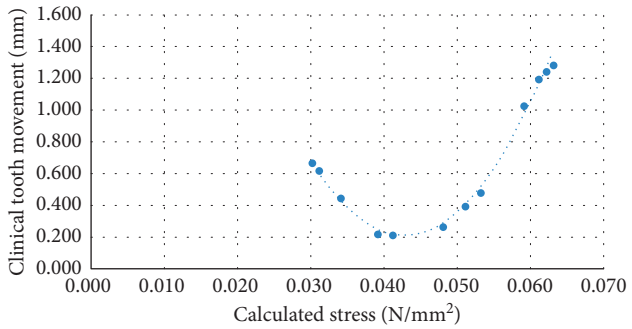

Figure 6: Relationship between the calculated stress and clinical tooth movement of the second orthodontic patient.

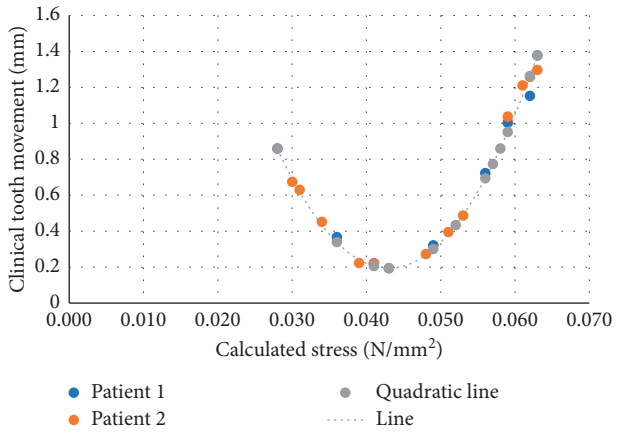

Figure 7: Relationship between the calculated stress and clinical tooth movement of the first and second orthodontic patient and quadratic line of the equation.

models should be performed to predict tooth movement for time periods longer than one month because the stress would change during treatment and would affect the amount of tooth movement. The other factor that affects the outcome is individual tissue response [29]. Although data from the second patient seem to be in better agreement with the equation, the error in the data of the first patient occurred from one point of measurement, C1M, which might affect the multiple processes. When the data of C1M for the first patient was excluded, the agreement in both patients was similar (Figure 7). However, the present study revealed similar results between the two patients. The equation created from the first patient could be used to predict the clinical outcome of the second patient (Table 3).

The FEM presented in this study would be an alternative method to simulate orthodontic tooth movement. This could assist treatment planning by predicting the outcome of clinical treatment and assist orthodontists in choosing a treatment option for the best outcome. Researchers should be able to use this finite element prediction to test various mechanics, and materials in different situations for orthodontic plans before a clinical trial which traditionally takes a long time and usually involves ethical issues. However, this technique requires several procedures and an investment of time for the 3D modeling process. The evolution of computer technology may facilitate simpler 3D modeling methods in the near future. The FEM processing protocol should be developed further in terms of saving time and user friendliness for general orthodontists.

The major limitation of this research is the small sample size due to the difficulty in 3D model production and analysis, which take long periods of time [30]. Orthodontic tooth movement is a biological response depending upon the individual. Affirmation of FEM results to clinical results therefore should be performed in a greater quantity of sample size. However, this precursory research has delivered positives results, which can be continuously researched.

4. Conclusions

Within the limitation of this study, it can be concluded that the 3D FEM simulation of orthodontic tooth movement can be achieved by combining data from a dental CT and a digital model. This technique provided acceptable accuracy. The outcome of tooth movement obtained from the FEM was found to be similar to the actual clinical tooth movement.

Data Availability

The data used to support the findings of this study are available from the corresponding author upon request.

Conflicts of Interest

The authors declare that they have no conflicts of interest.

Acknowledgments

This study was supported by the Faculty of Graduate Studies, Prince of Songkla University, Hat Yai, Songkhla, Thailand, and the Common Oral Diseases and Epidemiology Research Center (Ph.D. program).

References

[1] E. Storey and R. Smith, "Force in orthodontics and its relation to tooth movement," *Australian Journal of Dentistry*, vol. 56, pp. 11–18, 1952.

[2] K. Reitan, "Some factors determining the evaluation of forces in orthodontics," *American Journal of Orthodontics*, vol. 43, no. 1, pp. 32–45, 1957.

[3] D. Picton and W. Davies, "Dimensional changes in the periodontal membrane of monkeys (*Macaca irus*) due to horizontal thrusts applied to the teeth," *Archives of Oral Biology*, vol. 12, no. 12, pp. 1635–1643, 1967.

[4] D. Wills, D. Picton, and W. Davies, "An investigation of the viscoelastic properties of the periodontium in monkeys," *Journal of Periodontal Research*, vol. 7, no. 1, pp. 42–51, 1972.

[5] P. Rygh, "Elimination of hyalinized periodontal tissues associated with orthodontic tooth movement," *European Journal of Oral Sciences*, vol. 82, no. 1, pp. 57–73, 1974.

[6] Z. Davidovitch and J. Shanfeld, "Cyclic AMP levels in alveolar bone of orthodontically-treated cats," *Archives of Oral Biology*, vol. 20, no. 9, pp. 567–574, 1975.

[7] M. Chiba and S. Ohkawa, "Measurement of the tensile strength of the periodontium in the rat mandibular first molar," *Archives of Oral Biology*, vol. 25, no. 8-9, pp. 569–572, 1980.

[8] K. Yamasaki, "The role of cyclic AMP, calcium, and prostaglandins in the induction of osteoclastic bone resorption associated with experimental tooth movement," *Journal of Dental Research*, vol. 62, no. 8, pp. 877–881, 1983.

[9] J. Sandy, "DNA changes in mechanically deformed osteoblasts: a new hypothesis," *Journal of Orthodontics*, vol. 20, no. 1, pp. 1–11, 1993.

[10] J. R. Sandy and R. W. Farndale, "Second messengers: regulators of mechanically-induced tissue remodelling," *European Journal of Orthodontics*, vol. 13, no. 4, pp. 271–278, 1991.

[11] J. Sandy, "Signal transduction," *Journal of Orthodontics*, vol. 25, no. 4, pp. 269–274, 1998.

[12] C. L. Steyn, W. S. Verwoerd, E. J. Van Der Merwe, and O. L. Fourie, "Calculation of the position of the axis of rotation when single-rooted teeth are orthodontically tipped," *Journal of Orthodontics*, vol. 5, no. 3, pp. 153–156, 1978.

[13] A. Nakamura, T. Teratani, H. Itoh, J. Sugawara, and H. Ishikawa, "Photoelastic stress analysis of mandibular molars moved distally with the skeletal anchorage system," *American Journal of Orthodontics and Dentofacial Orthopedics*, vol. 132, no. 5, pp. 624–629, 2007.

[14] C. J. Burstone and R. J. Pryputniewicz, "Holographic determination of centers of rotation produced by orthodontic forces," *American Journal of Orthodontics*, vol. 77, no. 4, pp. 396–409, 1980.

[15] B. Ludwig, S. Baumgaertel, B. Zorkun et al., "Application of a new viscoelastic finite element method model and analysis of miniscrew-supported hybrid hyrax treatment," *American Journal of Orthodontics and Dentofacial Orthopedics*, vol. 143, no. 3, pp. 426–435, 2013.

[16] R. J. Lee, A. Weissheimer, J. Pham et al., "Three-dimensional monitoring of root movement during orthodontic treatment," *American Journal of Orthodontics and Dentofacial Orthopedics*, vol. 147, no. 1, pp. 132–142, 2015.

[17] M. Galvão, J. Sato, and E. Coelho, "Dahlberg formula–a novel approach for its evaluation," *Dental Press Journal of Orthodontics*, vol. 17, no. 1, pp. 115–124, 2012.

[18] H. Tripolt, C. J. Burstone, P. Bantleon, and W. Manschiebel, "Force characteristics of nickel-titanium tension coil springs," *American Journal of Orthodontics and Dentofacial Orthopedics*, vol. 115, no. 5, pp. 498–507, 1999.

[19] U. Likitmongkolsakul, J. Aksornmuang, P. Smithmaitrie, and B. Samruajbenjakun, "Three dimensional simulation of root position by a combined technique using cone beam computed tomography and a digital model," *Journal of Indian Orthodontic Society*, 2018, In press.

[20] D. J. Rudolph, M. G. Willes, and G. T. Sameshima, "A finite element model of apical force distribution from orthodontic tooth movement," *The Angle Orthodontist*, vol. 71, no. 2, pp. 127–131, 2001.

[21] A. Geramy, J. Bouserhal, D. Martin, and P. Baghaeian, "Bone stress and strain modification in diastema closure: 3D analysis using finite element method," *International Orthodontics*, vol. 13, no. 3, pp. 274–286, 2015.

[22] T. S. Fill, R. W. Toogood, P. W. Major, and J. P. Carey, "Analytically determined mechanical properties of, and models for the periodontal ligament: critical review of literature," *Journal of Biomechanics*, vol. 45, no. 1, pp. 9–16, 2012.

[23] Y. Kojima, H. Fukui, and K. Miyajima, "The effects of friction and flexural rigidity of the archwire on canine movement in sliding mechanics: a numerical simulation with a 3-dimensional finite element method," *American Journal of Orthodontics and Dentofacial Orthopedics*, vol. 130, no. 3, pp. 275.e10–275.e1, 2006.

[24] K. R. Williams, J. T. Edmundson, G. Morgan, M. L. Jones, and S. Richmond, "Orthodontic movement of a canine into an adjoining extraction site," *Journal of Biomedical Engineering*, vol. 8, no. 2, pp. 115–120, 1986.

[25] K. Williams and J. Edmundson, "Orthodontic tooth movement analysed by the finite element method," *Biomaterials*, vol. 5, no. 6, pp. 347–351, 1984.

[26] M. Nishihira, K. Yamamoto, Y. Sato, H. Ishikawa, and A. N. Natali, *Mechanics of Periodontal Ligament*, Taylor & Francis, Didcot, UK, 2003.

[27] A. M. Schwarz, "Tissue changes incidental to orthodontic tooth movement," *International Journal of Orthodontia, Oral Surgery and Radiography*, vol. 18, no. 4, pp. 331–352, 1932.

[28] K. Reitan, "The initial tissue reaction incident to orthodontic tooth movement as related to the influence of function; an experimental histologic study on animal and human material," *Acta Odontologica Scandinavica*, vol. 6, pp. 1–240, 1951.

[29] C. Verna, M. Dalstra, and B. Melsen, "The rate and the type of orthodontic tooth movement is influenced by bone turnover in a rat model," *European Journal of Orthodontics*, vol. 22, no. 4, pp. 343–352, 2000.

[30] U. Likitmongkolsakul, *Development and validation of 3d finite element models for prediction of orthodontic tooth movement*, Ph.D. thesis, Prince of Songkla University, Hat Yai, Songkhla, Thailand, 2018.

Hindawi
International Journal of Dentistry
Volume 2018, Article ID 8926314, 12 pages
https://doi.org/10.1155/2018/8926314

Research Article

Assessing the Correlation between Skeletal and Corresponding Soft-Tissue Equivalents to Determine the Relationship between CBCT Skeletal/Dental Dimensions and 3D Radiographic Soft-Tissue Equivalents

Da In Kim[1] **and Manuel O. Lagravère**[2]

[1]*School of Dentistry, Faculty of Medicine and Dentistry, University of Alberta, ECHA, 11405-87 Avenue, Edmonton, AB, Canada T6G 1C9*
[2]*School of Dentistry, Faculty of Medicine and Dentistry, University of Alberta, Edmonton, AB, Canada T6G 1C9*

Correspondence should be addressed to Manuel O. Lagravère; mlagravere@ualberta.ca

Received 4 April 2018; Revised 30 May 2018; Accepted 2 June 2018; Published 3 July 2018

Academic Editor: Vahid Rakhshan

Objective. Compare measurements of skeletal and dental areas on the CBCT to the corresponding soft-tissue measures taken from a 3D Facial Scanner. *Methods*. 30 patients with CBCT and 3D Facial scanner photos were selected from the orthodontic program database. 30 different distance measurements were obtained from CBCT and facial scan. OrthoInsight software was used to obtain the measurements from the facial scan images, and AVIZO software was used for corresponding CBCT landmarks. The Euclidean distance formula was used to determine the distances for the corresponding x, y, and z coordinates of the CBCT. Reliability for CBCT and Facial Scanner was completed by calculating 30 distances for 10 patients, 3 times. Once reliability was determined, all 30 distances were calculated once for CBCT and facial scanner on each patient and descriptive statistics and paired t-test were applied. *Results*. All distances measured presented excellent reliability, the lowest one being the left eye width for the facial scanner (ICC 0.847). The landmark with the highest mean error on the CBCT was 2.0 ± 1.6 mm on the z-axis for the spinal level landmark. The Facial Scanner's largest mean measurement error was 1.5 ± 0.9 mm for the distance of the left corner of the mouth to gonion. All data except width between outer eye corners were statistically significant ($p < 0.05$). The average differences between facial scan and CBCT measurements ranged between 0.77 mm (left canine to cheekbone) to 26.94 mm (left subnasale to gonion) and are thus comparable. All measurements show a reasonable standard deviation between 2.57 mm (left eye width) to 9.91 mm (left gnathion to EAM). *Conclusion*. Distances obtained from CBCT and facial scan present mild differences giving the perspective of a relationship between them. Understanding this difference and relationship can make it plausible to expect certain underlying skeletal distances under soft-tissue structures.

1. Introduction

Since the development of dental photographic tools, much emphasis is put on skeletal landmarks as a tool for measurement in orthodontic analysis. In addition to skeletal evaluation, facial soft tissue evaluation plays a relevant role in treatment planning [1], since facial changes must be estimated while a patient undergoes long-term treatment. Both soft- and hard-tissue analyses as well as a more exact prediction of hard and soft tissue changes are important tools to help the clinician assess treatment outcomes and give added diagnostic information about the patient [2].

2D lateral cephalometric imaging has been the routine method of obtaining hard-tissue information of the patient [3]. In recent years, high precision of three-dimensional (3D) cone-beam computed tomography (CBCT) scanners and their clinically insignificant errors has gauged interest in many clinicians to use this as a routine tool for hard-tissue investigation during treatment planning and diagnosis [4]. However, 3D hard-tissue analysis alone is inadequate for

proper treatment planning. Since soft-tissue profile reflects underlying skeletal tissue, visual inspection and examination of the patient can give insightful information of the underlying dental tissue [5]. Conventional methods for facial soft-tissue analysis include 2D measurement methods, such as taking photos of the patient at different angles [6]. These photos are then used to measure certain distances via computational analysis. Over the years, 3D facial soft-tissue analysis has been introduced to provide a more accurate description of the patient's soft-tissue profile [6]. These 3D facial scanners use a strip of laser light to record the contour of the patient's face and cranium and project their recordings onto a computer. With this 3D information, clinicians are able to obtain information such as cranial growth changes and treatment outcomes in a more realistic fashion. This ultimately allows the clinician to undergo prediction planning for the patient [7].

As such, both 3D soft- and hard-tissue analyses are essential in obtaining precise measurements for treatment planning. However, precise facial measurements can only be made when the clinician truly understands the relationship between these two imaging modalities and by obtaining a truthful 3D model of the soft tissues and underlying skeletal structures [7]. By determining relationships and assessing imaging tendencies between CBCT and facial scanner, clinicians will be able to deliver diagnoses with increased exactness: if the soft-tissue distance is highly correlated with that of the hard tissue, the clinician can conclude that this particular distance on the skin can highly reflect its underlying hard-tissue distance. Also, these would be the initial steps towards verifying the effects of treatments (orthodontic or surgical) on soft tissues when viewing in three-dimensions. The objective of this study is therefore, to analyze different landmark relations obtained from 3D facial scanner and CBCT for comparison and prediction planning, for use as a diagnostic tool.

2. Materials and Methods

CBCTs and 3D facial scans from 30 patients that were seen in the University of Alberta Graduate Orthodontic Clinic were selected for analysis. The basis for this sample size was based on availability of the images needed for the purpose of this study, since the CBCT and facial scan images were all taken retrospectively and were chosen amongst a main database. The reasoning of the full field of view CBCTs for these patients was for diagnostic and treatment planning purposes of the orthodontists in charge of the individual patient cases and was not taken for the purpose of this study. The University of Alberta's Human Research Ethics Board approved of this study (Pro00057947). CBCT scans of 0.3 mm voxel size were taken with the I-CAT Next generation device (9 sec exposure time, 13 cm x 16 cm FOV, 0.3 mm voxel size, Imaging Sciences International, Hatsfield, PA) at 120 kV, 5 mA with 8 mm aluminum filtration according to manufacturer's settings. 3D facial scans were obtained on the same day as the CBCTs, using Ortho Insight 3D Scanner (Motion View LLC., United States of America). All images were chosen with patients in their natural upright head position, with the Frankfort plane parallel to the floor. As all data were collected retrospectively, strict positioning of the head was not available to be controlled. CBCTs were analyzed using a third party software called AVIZO (Thermo Fisher Scientific, Hillsboro, United States of America), which helped to obtain the 3D reconstruction of the image for landmark positioning.

In relation to a reference point, each CBCT landmark (Tables 1 and 2) was given coordinates in x, y, and z format. This reference point was an arbitrary position placed amongst the coordinates of the software program. Since the distance between two specific points were to be measured, the initial reference point for each distance was different for each patient and distance, as it was all relative to where the second point was to be placed. The Euclidean distance formula was used to determine the linear distances for the corresponding x, y, and z coordinates.

$$d = \sqrt{(x_1 - x_2)^2 + (y_1 - y_2)^2 + (z_1 - z_2)^2}. \quad (1)$$

The facial scanning machine along with its corresponding third party software, OrthoInsight, was used to obtain the 3D soft-tissue profile of the patient. Soft-tissue distances between landmarks (Table 3) were calculated by the software to obtain landmark measurements in millimetres.

CBCTs and 3D facial scans from 10 patients out of the main sample were selected for reliability analysis (Figures 1 and 2). For the CBCT, reliability analysis was performed by initially obtaining 30 preselected distances (Table 1) based off of well-defined landmarks on soft and hard tissues (Table 2), for each of these 10 sets of patient images for both imaging modalities. All 30 distances were measured repeatedly, 3 times in total, for all 10 selected patient images for the CBCT and facial scan. A time span of one week took place after each of those three trials, in order to minimize any errors regarding the researcher's subjectivity of the placement of landmarks, especially those that were not too precise to locate on the images. Coordinates of the CBCT were analyzed for reliability calculations. For the facial scan, the same 30 distances (Table 1) were measured on 10 different facial scans, 3 times. Landmark distances were measured 3 times, leaving a week in between trials. Reliability calculations were performed from this data. Following landmark reliability calculations, the true data set of CBCT and facial scan images of the 30 selected patients were analyzed. Each of the 30 chosen distances was measured once on these patients for both imaging modalities. Descriptive statistics and paired t-test calculations were applied in order to obtain information regarding the relationships between distances on the skeletal and those on the facial tissue. The gold standard imaging modality is the CBCT, as it claims to have high precision (1 : 1 image to reality ratio), minimum deviation, and is highly reliable when evaluating linear distances for craniofacial analysis [4, 8–13].

3. Results

All measured distances presented excellent reliability, the lowest one being the left eye width of the facial scanner, with an intraclass correlation coefficient (ICC) of 0.847 (Tables 4 and 5). For CBCTs, the landmark with the highest mean error was 2.0 ± 1.6 mm on the z-axis for the spinal level

Table 1: Measured and defined distances depending on the image used.

	Landmarks	Description of distances on CBCT	Description of distances on facial scanner
1	Width of nose	Left bottom-most skeletal corner under the nasal aperture to the right bottom-most skeletal corner	Left alar curvature point (the most lateral part of the curved base of the ala) to the right alar curvature point
2	Left canine to left outer eye	Most tip of left canine crown to left frontozygomatic suture	Most tip of left canine (patient smiling) to left lateral canthus
3	Right canine to right outer eye	Most tip of right canine crown to right frontozygomatic suture	Most tip of right canine (patient smiling) to right lateral canthus
4	Gnathion to throat	Lowest point of the midline of the mandible to C3-C4 cervical vertebrae	Lowest point of the midline of the mandible to the most indented location of the throat between the chin and neck
5	Gnathion to left gonion	Lowest point of the mandibular midline to the lowest, most posterior, and lateral point of the left mandibular angle	Lowest point of the mandibular midline to the lowest, most posterior, and lateral point of the left mandibular angle
6	Gnathion to right gonion	Lowest point of the mandibular midline to the lowest, most posterior, and lateral point of the right mandibular angle	Lowest point of the mandibular midline to the lowest, most posterior, and lateral point of the right mandibular angle
7	Left canine to left cheekbone	Most tip of left canine crown to most prominent frontal portion of the left zygomatic bone	Most tip of left canine crown (patient smiling) to most prominently raised point of left cheek area, most likely an area under the left lateral canthus
8	Right canine to right cheekbone	Most tip of right canine crown to most prominent frontal portion of the right zygomatic bone	Most tip of right canine crown (patient smiling) to most prominently raised point of right cheek area, most likely an area under the right lateral canthus
9	Nasion to gnathion	Distinctly depressed area between the intersection of the frontal bone and two nasal bones to the lowest point of the mandibular midline.	Distinctly depressed area directly between the eyes and superior to the bridge of the nose to the lowest point of the mandibular midline
10	Gnathion to left external auditory meatus (EAM)	Lowest portion of the mandibular midline to lowest bony portion of the left hollow canal of the tympanic portion of the temporal bone, posterior to the condylar process of the mandible	Lowest portion of the mandibular midline to the left lowest portion of the hollow ear canal
11	Gnathion to right EAM	Lowest portion of the mandibular midline to lowest bony portion of the right hollow canal of the tympanic portion of the temporal bone, posterior to the condylar process of the mandible	Lowest portion of the mandibular midline to the right lowest portion of the hollow ear canal
12	Corners of mouth	Tip of left canine crown to tip of right canine crown	Left cheilion (left labial commissure) to right cheilion (right labial commissure)
13	Left EAM to left outer eye corner	Lowest bony portion of the left hollow canal of the tympanic portion of the temporal bone, posterior to the condylar process of the mandible, to the left lateral canthus of eye	Left lowest portion of the hollow ear canal to the left lateral canthus of eye
14	Right EAM to right outer eye corner	Lowest bony portion of the right hollow canal of the tympanic portion of the temporal bone, posterior to the condylar process of the mandible, to the right lateral canthus of eye	Right lowest portion of the hollow ear canal to the right lateral canthus of eye
15	Bottom of nose to nasion	Anterior nasal spine to the distinctly depressed area between the intersection of the frontal bone and two nasal bones	Subnasale (the midpoint of the angle at the nasal base where the lower border of the nasal septum and the upper lip surface meets) to the distinctly depressed area directly between the eyes and superior to the bridge of the nose
16	Width of left eye	Left frontozygomatic suture to left frontomaxillary suture	Left lateral canthus to left medial canthus
17	Width of right eye	Right frontozygomatic suture to right frontomaxillary suture	Right lateral canthus to right medial canthus
18	Left inner eye to left canine	Left frontomaxillary suture to tip of left canine crown	Left medial canthus to tip of left canine crown (patient smiling)
19	Right inner eye to right canine	Right frontomaxillary suture to tip of right canine crown	Right medial canthus to tip of right canine crown (patient smiling)

Table 1: Continued.

	Landmarks	Description of distances on CBCT	Description of distances on facial scanner
20	Left gonion to left EAM	Lowest, most posterior, and lateral point of the left mandibular angle to the lowest bony portion of the left hollow canal of the tympanic portion of the temporal bone, posterior to the condylar process of the mandible	Most posterior and lateral point of the left mandibular angle to the left most lowest portion of the hollow ear canal opening
21	Right gonion to right EAM	Lowest, most posterior, and lateral point of the right mandibular angle to the lowest bony portion of the right hollow canal of the tympanic portion of the temporal bone, posterior to the condylar process of the mandible	Most posterior and lateral point of the right mandibular angle to the right most lowest portion of the hollow ear canal opening
22	Bottom of nose to left EAM	Anterior nasal spine to the lowest bony portion of the left hollow canal of the tympanic portion of the temporal bone, posterior to the condylar process of the mandible	Subnasale (the midpoint of the angle at the nasal base where the lower border of the nasal septum and the upper lip surface meets) to the left most lowest portion of the hollow ear canal opening
23	Bottom of nose to right EAM	Anterior nasal spine to the lowest bony portion of the right hollow canal of the tympanic portion of the temporal bone, posterior to the condylar process of the mandible	Subnasale (the midpoint of the angle at the nasal base where the lower border of the nasal septum and the upper lip surface meets) to the right most lowest portion of the hollow ear canal opening
24	Left corner of mouth to left EAM	Tip of left canine crown to the lowest bony portion of the left hollow canal of the tympanic portion of the temporal bone, posterior to the condylar process of the mandible	Left cheilion (left labial commissure) to the left most lowest portion of the hollow ear canal opening
25	Right corner of mouth to right EAM	Tip of right canine crown to the lowest bony portion of the right hollow canal of the tympanic portion of the temporal bone, posterior to the condylar process of the mandible	Right cheilion (right labial commissure) to the right most lowest portion of the hollow ear canal opening
26	Width between outer eye corners	Left frontozygomatic suture to right frontozygomatic suture	Left lateral canthus to right lateral canthus
27	Left corner of mouth to left gonion	Tip of left canine crown to the lowest, most posterior, and lateral point of the left mandibular angle	Left cheilion (left labial commissure) to the most posterior and lateral point of the left mandibular angle
28	Right corner of mouth to right gonion	Tip of right canine crown to the lowest, most posterior, and lateral point of the right mandibular angle	Right cheilion (right labial commissure) to the most posterior and lateral point of the right mandibular angle
29	Bottom of nose to left gonion	Anterior nasal spine to lowest, most posterior, and lateral point of the left mandibular angle	Subnasale (the midpoint of the angle at the nasal base where the lower border of the nasal septum and the upper lip surface meets) to most posterior and lateral point of the left mandibular angle
30	Bottom of nose to right gonion	Anterior nasal spine to lowest, most posterior, and lateral point of the right mandibular angle	Subnasale (the midpoint of the angle at the nasal base where the lower border of the nasal septum and the upper lip surface meets), to most posterior and lateral point of the right mandibular angle

landmark. The facial scanner's largest mean measurement error was 1.5 ± 0.9 mm for the distance of the left corner of the mouth to the left gonion.

When comparing the difference between facial scanner and CBCT measurements via the paired t-test, all data except that of the width between outer eye corners were statistically significant ($p < 0.05$). Although the p value of the width between outer eye corners is $p = 0.44$, a very small facial scan to CBCT mean difference of 0.71 mm makes this measurement comparable.

Most measurements had a mean facial scan to CBCT difference of less than 9 mm. Such means indicate that distances measured on the CBCT and facial scan are very similar and thus comparable. However, measurements containing the left and right gonion, throat, corners of mouth, and subnasale had large facial scan to CBCT mean differences ranging from 16.66 mm (right corner of mouth to gonion) to 23.32 mm (left subnasale to gonion). Even though these means were relatively large, *paired* measurements with left and right sides had similar means. For example, the left gnathion to gonion measurement had a mean of 21.76 mm, while the right gnathion to gonion measurement had a mean of 20.79 mm, giving a difference in measurement of only 0.97 mm; although the mean is relatively large, both left and right sides are similar, indicating that they are comparable.

Table 2: Definition of landmarks used for measuring specific distances, depending on the imaging modality used.

	Landmark	Description of landmark on CBCT	Description of landmark on soft tissue
1	Sides of nose	Left/right bottom most skeletal corner under the nasal aperture	Left/right alar curvature (most lateral part of the curved base of the ala)
2	Canine	Most tip of the left/right canine crown	Most tip of the left/right canine crown
3	Outer eye	Left/right frontozygomatic suture	Left/right lateral canthus
4	Gnathion	Lowest point of the midline of the mandible	Lowest point of the midline of the mandible
5	Throat	C3-C4 cervical vertebrae location	Most indented location of the throat between the chin and neck
6	Gonion	Most posterior and lateral point of the left/right mandibular angle	Most posterior and lateral point of the left/right mandibular angle on the skin
7	Cheekbone	Most prominent frontal portion of the left/right zygomatic bone	Most prominently raised point of the left/right cheek area, most likely an area under the left/right lateral canthus
8	Nasion	Distinctly depressed area between the intersection of the frontal bone and two nasal bones	Distinctly depressed area directly between the eyes and superior to the bridge of the nose
9	External auditory meatus (EAM)	Lowest bony portion of the left/right hollow canal of the tympanic portion of the temporal bone, posterior to the condylar processes of the mandible	Left/right lowest portion of the hollow ear canal
10	Corners of mouth	Tip of left/right canine crowns	Left/right cheilion (left/right labial commissures)
11	Bottom of nose	Anterior nasal spine	Subnasale (midpoint of the angle at the nasal base where the lower border of the nasal septum and upper lip surface meets)
12	Inner eye	Left/right frontomaxillary suture	Left/right medial canthus

4. Discussion

Hard- and soft-tissue analyses are both critical tools for patient treatment planning and diagnosis and analysis of the patient over a long period of time. In contrary to conventional soft tissue and skeletal imaging tools such as patient photos and 2D analog films, 3D images of the patient are considered the ideal method of representing the face, and thus gives added information to the clinician, which in turn will give more realistic analyses [7]. Unlike using traditional 2D imaging to analyze 3D structures, which can have limited significance [7, 14, 15], comparing 3D hard to 3D soft tissue structures can be an improved alternate for the clinician to assess and evaluate cranial changes over time. Recently, several studies have adopted similar approaches in comparing 3D photography to CBCT concepts and have concluded that there is a close relationship between patient images taken by these two modalities.

In the present study, all measurements show a reasonable standard deviation between 2.57 mm (left eye width) to 9.91 mm (left gnathion to EAM). This shows that over a large sample size, these measurements are very similar, and less variable. However, the standard deviation for the gnathion to throat measurement is comparably large at 23.34 mm. This shows that there is lot of variation between the gnathion to throat measurement within a large sample.

The ratio between the soft tissue and CBCT measurements indicate their close correlation and any amount of variation or difference between them. The ratio percentages presented on Table 3 indicate the percentage of the CBCT distance measurements compared to that of the soft tissue measurements. Most ratio measurements are ±20%, but those that include the left and right gonion have a tendency to have smaller ratios, except for that of the left gonion to left EAM (+49.76%) and that of the right gonion to right EAM (+52.92%). These small ratios indicate that the CBCT, when measuring distances including the left and right gonion, tend to measure shorter than the soft tissue distances. A similar finding is seen in a study conducted by Naudi et al. [7], who evaluated the registration exactness of the simultaneous capture between a CBCT scan and a 3D surface of the face. Unlike the present study, the CBCT scans of this study captured soft-tissue measures to compare their superimposition with the 3D image capture. Naudi et al. concluded that in most of the facial surfaces, the level of superimposition in designated facial patches was 0.4 mm for simultaneous captures, denoting that superimpositions of the CBCT were smaller than those of the 3D image capture. The study also concluded that the most significant difference of superimposition between the CBCT and 3D image capture was in the chin area, with the mobile nature of the mandible being a large contributing factor of this result. It was mentioned that the relaxing atmosphere of the 3D image capture rooms may have led to patients slightly opening their jaws and bringing their teeth apart, leading to a slight increase in the degree of mouth opening and spatial changes of the related soft tissue. It can therefore be extrapolated that a larger degree of mouth opening of the soft tissue scans leads to a large superimposition, and thus, a larger difference compared to the CBCT image. These findings of Naudi et al. agree with the present study, as it was found that the tendency of losing measurement similarity, and thus having less of an intimate relationship between CBCT and facial scans was most prominent along the lateral portions of the face.

The tendency of having a lower correlation along the lateral portions of the face can be due to the variability of amounts of subcutaneous tissue present on each patient, but it may also be attributed to the increased amounts of larger,

Table 3: Statistics of soft tissue distances and their CBCT equivalents, including average mean measurements, standard deviation, the difference between the average mean measurements, and the ratio of the CBCT distances to the soft-tissue distances in percentage format, p values, and 95% confidence intervals of the differences between the facial scan and CBCT.

	Landmarks	Soft tissue measurements		CBCT hard tissue measurements		p value	95% confidence interval of the differences (facial scan-CBCT)		Facial scanner and CBCT mean difference (mm)	Ratio of soft tissue and CBCT distances (%)
		Average mean (mm)	Standard deviation	Average mean (mm)	Standard deviation		Lower	Upper		
1	Width of nose	25.26	2.53	21.65	3.33	0.001	−15.04	9.43	3.61	−14.29
2	Left canine to left outer eye	70.05	3.97	78.60	5.62	0.001	−17.70	−5.79	−8.55	+12.21
3	Right canine to right outer eye	70.47	4.49	77.90	5.33	0.001	−9.17	−5.68	−7.43	+10.54
4	Gnathion to throat	68.68	24.07	79.67	10.09	0.019	−20.88	−0.42	−10.99	+16.00
5	Gnathion to left gonion	101.68	8.37	79.92	7.72	0.001	21.59	31.86	21.76	−21.40
6	Gnathion to right gonion	100.56	8.33	79.77	6.03	0.001	21.11	31.55	20.79	−20.67
7	Left canine to left cheekbone	48.18	3.28	43.51	3.62	0.001	−7.04	8.58	4.67	−9.69
8	Right canine to right cheekbone	49.09	4.07	42.07	6.32	0.001	−20.36	16.31	7.02	−14.30
9	Nasion to gnathion	116.51	8.51	111.41	8.58	0.003	0.18	14.99	5.10	−4.38
10	Gnathion to left external auditory meatus (EAM)	128.58	12.71	120.86	9.25	0.001	−4.89	15.28	7.72	−6.00
11	Gnathion to right EAM	127.69	12.15	120.30	9.25	0.001	3.47	15.03	7.39	−5.79
12	Corners of mouth	47.43	4.80	35.67	3.74	0.001	−6.24	17.90	11.76	−24.79
13	Left EAM to left corner eye	80.71	5.52	72.88	5.10	0.001	0.29	10.71	7.83	−9.70
14	Right EAM to right corner eye	80.80	5.59	72.87	5.00	0.001	−1.95	10.40	7.93	−9.81
15	Bottom of nose to nasion	47.71	4.32	54.05	6.19	0.001	−8.87	−4.29	−6.34	+13.29
16	Width of left eye	30.94	2.28	38.43	2.79	0.001	−26.87	−1.01	−7.49	+24.21
17	Width of right eye	31.19	2.38	38.48	2.62	0.001	−8.30	−6.27	−7.29	+23.37
18	Left inner eye to left canine	63.27	4.46	70.51	5.48	0.001	−20.34	−2.78	−7.24	+11.44
19	Right inner eye to right canine	63.63	4.63	70.44	5.72	0.001	−43.33	5.63	−6.81	+10.70
20	Left gonion to left EAM	35.25	5.90	52.79	6.53	0.001	−26.02	−14.41	−17.54	+49.76
21	Right gonion to right EAM	34.88	5.17	53.34	7.38	0.001	−27.41	−14.06	−18.46	+52.92
22	Bottom of nose to left EAM	119.07	8.82	101.26	9.21	0.001	14.00	24.11	17.81	−14.96
23	Bottom of nose to right EAM	120.17	8.80	101.29	8.81	0.001	−11.12	30.86	18.88	−15.71
24	Left corner of mouth to left EAM	98.68	7.96	95.78	7.54	0.015	−6.78	6.25	2.90	−2.94
25	Right corner of mouth to right EAM	98.86	8.03	94.92	7.70	0.001	−0.19	7.08	3.94	−3.99
26	Width between outer eye corners	94.88	5.42	94.18	11.69	0.437	−7.03	10.41	0.70	−0.74
27	Left corner of mouth to left gonion	85.72	6.76	68.43	8.44	0.001	7.96	23.08	17.29	−20.17
28	Right corner of mouth to right gonion	84.42	7.15	67.76	6.11	0.001	15.41	20.23	16.66	−19.73
29	Bottom of nose to left gonion	109.42	8.33	86.10	9.35	0.001	21.29	32.56	23.32	−21.31
30	Bottom of nose to right gonion	110.41	8.98	87.26	8.93	0.001	19.84	33.63	23.15	−20.97

curved, boney surface areas on the lateral profile of the face. Toma et al. [16] indicated that due to the difficulty of placing points accurately on a patient's lateral profile, soft-tissue landmarks on both left and right lateral sides of the face are not highly reproducible. Such findings agree with the present study, since it was also found in this investigation that the left and right gonions have a tendency to elicit relatively large differences amongst soft tissue and CBCT landmark sites, whereas some of the smallest CBCT to soft tissue ratios were found along landmarks near the center of the face, including the width between outer eye corners (−0.74%) and the measurement between the nasion to gnathion (−4.38%).

Baumrind and Frantz [17] also found that the gonion was one of the least reliable landmarks to identify, whereas the nasion had a relatively smaller skeletal landmark estimating error. Although this study focused on 2D films, their findings can be extrapolated to 3D skeletal measurements on CBCT films. The study acknowledged that as a boney structure has a gradually curving edge, such as the gonion, the mean error of incorrect landmarking tends to be larger, leading to the large measurement error. Their findings agree with the present study, because in this investigation, landmark distances including either the left or right gonion were interpreted as those with the least amount of correlation between CBCT and 3D facial scanner (Table 3). The difficulty of locating the exact landmark of the left and right gonions may have lead to the large CBCT to soft tissue ratio difference, since landmarks may have been unintentionally placed along different areas of this largely curved boney edge. Additionally, despite the precise definition given to the gonion on the soft tissue (Table 1), the structure itself was found to be very challenging to visualize on facial images of

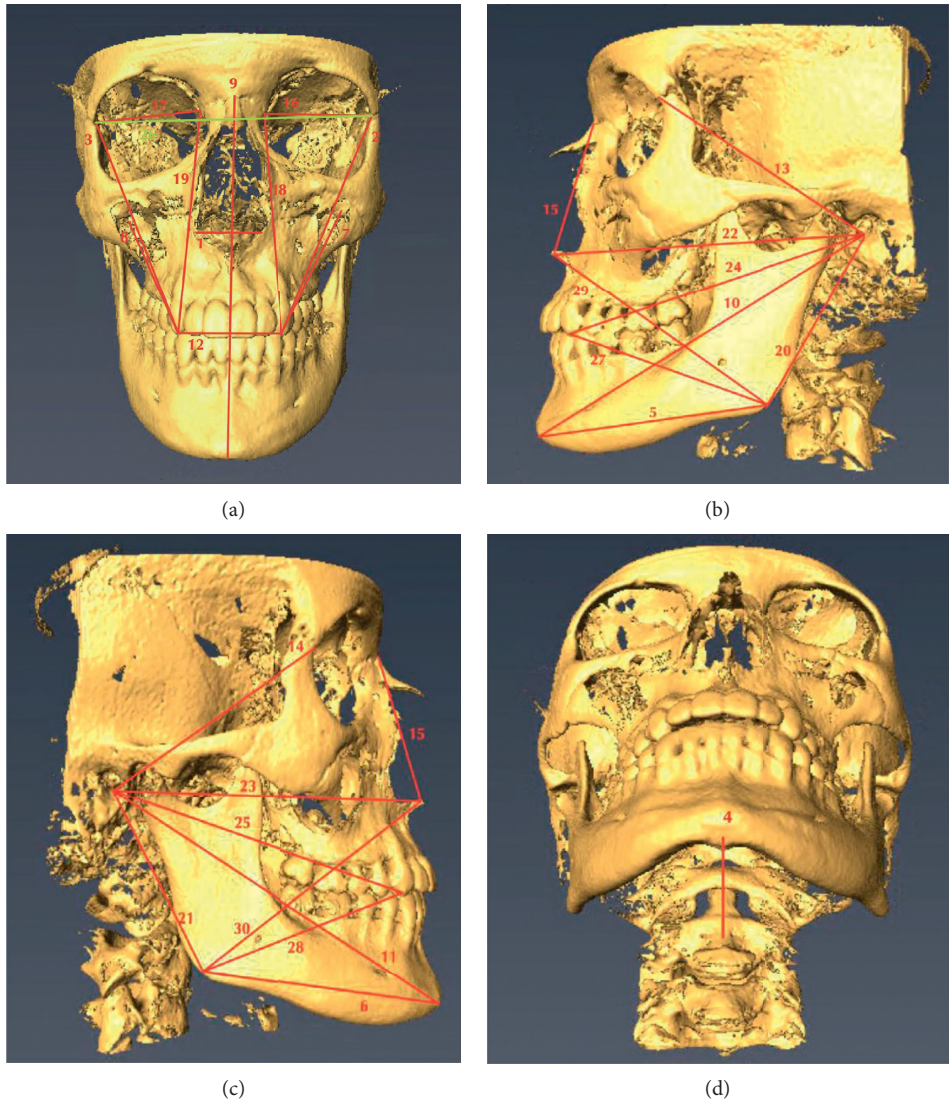

(a) (b) (c) (d)

Figure 1: Front, left lateral profile, right lateral profile, and inferior views of the CBCT image, with numbered areas corresponding to landmarks. (a) Frontal view. (b) Left lateral profile view. (c) Right lateral profile view. (d) Inferior view.

the patient, as it is a structure that is easily hidden by subcutaneous tissue underneath.

As mentioned previously, measurements containing the left and right gonion, throat, corners of mouth, and subnasale had large facial scanner to CBCT mean differences. These measurements, along with others that had large means between facial scanner and CBCT data were those that had slightly different landmarks on the face between the two imaging modalities. Another study conducted by Maal et al. [18] had similar findings. This group investigated image fusion between soft tissue CBCT images and 3D photographs. It was found in their study that registration errors between CBCT and 3D images were largest at the lateral neck, mouth, and areas around the eyes. One of the causes of such dissimilarities was accredited to the fact of the inability of the CBCT to capture exact soft-tissue surfaces. Although this study focused on soft tissue comparison, the present study agrees with the concept that more registration error is found when there are different locations and definitions present for the same area on the face between two different imaging modalities. Soft-tissue CBCTs of Maal et al. were not of the same quality of comparison to that of the 3D images, and thus less precise locations would have been compared between these two imaging modalities. Similarly in this project, landmarks with a significant soft tissue to CBCT ratio > 20% are mainly due to the different definitions of the landmarks of the CBCT and soft tissue images, as defined in Table 1. The different definitions were created because it was acknowledged that hard- and soft-tissue landmarks are distinctly different in some definitions. For example, the large ratio percentage of the measurement of the width of the left eye (+24.21%) and the width of the right eye (+23.37%) raises mostly due to the different landmarking positions. The definition given for the "width of eye" is completely different: the CBCT defines this landmark as a distance between the frontozygomatic suture and the frontomaxillary suture,

Figure 2: Frontal, left lateral profile, right lateral profile, inferior, frontal smiling, left lateral profile smiling, and right lateral profile smiling views of the facial scanner image, with numbered areas corresponding to landmarks. (a) Frontal View. (b) Left lateral profile view. (c) Right lateral profile view. (d) Inferior view. (e) Frontal view, smiling. (f) Left lateral profile view, smiling. (g) Right lateral profile view, smiling.

whereas the same landmark on the facial scanner is defined to be the distance from the lateral canthus to the medial canthus. Since both skeletal sutures extend beyond the lateral and medial canthi, this may be the cause of the CBCT's ratio being much higher. The larger discrepancy of the ratio due to different definitions is also seen in the "corners of mouth" landmark (−24.79%). The CBCT definition of the distance between the corners of the mouth is from one tip of the canine crown to the other, whereas the soft tissue definition is that of one cheilion to the other. Since individuals may have extended lip commissures, which potentially go further beyond the location of their canines,

Table 4: Intraclass correlation coefficients (ICC) of facial scan landmarks, lower and upper limits of their 95% confidence intervals, and their corresponding p values.

	Landmarks	Intraclass correlation coefficient	95% confidence intervals of soft tissue ICC		p value
			Lower	Upper	
1	Width of nose	0.960	0.883	0.989	0.001
2	Left canine to left outer eye	0.965	0.900	0.991	0.001
3	Right canine to right outer eye	0.990	0.970	0.997	0.001
4	Gnathion to throat	0.999	0.997	1.000	0.001
5	Gnathion to left gonion	0.999	0.998	1.000	0.001
6	Gnathion to right gonion	0.999	0.998	1.000	0.001
7	Left canine to left cheekbone	0.947	0.846	0.986	0.001
8	Right canine to right cheekbone	0.971	0.918	0.992	0.001
9	Nasion to gnathion	1.000	0.999	1.000	0.001
10	Gnathion to left external auditory meatus (EAM)	1.000	0.999	1.000	0.001
11	Gnathion to right EAM	1.000	0.999	1.000	0.001
12	Corners of mouth	0.974	0.925	0.993	0.001
13	Left EAM to left corner eye	0.971	0.914	0.992	0.001
14	Right EAM to right corner eye	0.972	0.921	0.992	0.001
15	Bottom of nose to nasion	0.989	0.968	0.997	0.001
16	Width of left eye	0.847	0.539	0.959	0.001
17	Width of right eye	0.875	0.643	0.966	0.001
18	Left inner eye to left canine	0.993	0.979	0.998	0.001
19	Right inner eye to right canine	0.993	0.980	0.998	0.001
20	Left gonion to left EAM	0.994	0.983	0.998	0.001
21	Right gonion to right EAM	0.991	0.974	0.998	0.001
22	Bottom of nose to left EAM	0.998	0.994	0.999	0.001
23	Bottom of nose to right EAM	0.996	0.990	0.999	0.001
24	Left corner of mouth to left EAM	0.996	0.990	0.999	0.001
25	Right corner of mouth to right EAM	0.996	0.989	0.999	0.001
26	Width between outer eye corners	0.989	0.968	0.997	0.001
27	Left corner of mouth to left gonion	0.982	0.950	0.995	0.001
28	Right corner of mouth to right gonion	0.992	0.978	0.998	0.001
29	Bottom of nose to left gonion	0.994	0.982	0.998	0.001
30	Bottom of nose to right gonion	0.991	0.975	0.998	0.001

Table 5: Intraclass correlation coefficients (ICC) of CBCT landmarks, lower and upper limits of their 95% confidence intervals, and their corresponding p values.

	Landmark	Intraclass correlation coefficient	95% confidence intervals of CBCT ICC		p value
			Lower	Upper	
1	Left nose radiolucency	0.990	0.971	0.997	0.001
2	Right nose radiolucency	0.967	0.908	0.991	0.001
3	Left canine	0.993	0.980	0.998	0.001
4	Right canine	0.997	0.989	0.999	0.001
5	Gnathion	0.979	0.940	0.994	0.001
6	Throat (spinal level)	0.987	0.964	0.997	0.001
7	Left gonion	0.999	0.997	1.000	0.001
8	Right gonion	0.998	0.995	1.000	0.001
9	Left zygomatic process	0.975	0.927	0.993	0.001
10	Right zygomatic process	0.969	0.910	0.991	0.001
11	Left external auditory meatus	0.998	0.995	1.000	0.001
12	Right external auditory meatus	0.992	0.977	0.998	0.001
13	Left frontozygomatic suture (outer corner of eye)	0.987	0.963	0.997	0.001
14	Right frontozygomatic suture (outer corner of eye)	0.988	0.967	0.997	0.001
15	Subnasale	0.992	0.978	0.998	0.001
16	Nasion	0.991	0.973	0.997	0.001
17	Left frontonasal suture (inner corner of eye)	0.962	0.891	0.990	0.001
18	Right frontonasal suture (inner corner of eye)	0.977	0.934	0.994	0.001

this may cause the CBCT to be seemingly shorter than that of the soft-tissue distances, even though this difference was due to a dissimilar definition.

Considering anterior-posterior (AP) and vertical measurements, left and right gonion landmarks were easily found on the CBCT but were difficult to locate on the facial scanner. Depending on the patient's size, the location of the gonion was easily or not easily found on the facial scanner. If not found, approximate landmarks were taken for the location of the gonion, which may have contributed to a larger difference in location compared to the CBCT. The measurement involving the throat (gnathion to throat, −10.99 mm) also had a relatively large facial scanner to CBCT mean difference, since slightly different landmarks were taken between the facial scanner and CBCT. On the facial scanner, the throat was defined and landmarked as the deepest part of the neck when viewed from the left and right sides. On the CBCT, the "throat" was landmarked as the spinal level that corresponded to the area of the throat, approximately at C2. Such different landmarks may have possibly contributed to a larger difference in the mean, with the CBCT measurement being larger than that of the facial scanner. Large mean differences of the throat may be related to low reproducibility of landmarks, since soft tissue anatomical features of the throat are much less clear than the hard tissue definition of this landmark. This may ultimately lead to low intraobserver reproducibility of this landmark [19].

Considering transverse measurements, the corners of the mouth also lead to a relatively large mean difference of 11.76 mm. On the facial scanner, the corner of each side of the mouth was landmarked to the furthest corner of the lips when the patient was not smiling. On the CBCT, the landmark for each corner of the mouth was taken as the canine for left and right sides. With some patients having a shifted or rotated canine, no canine, or orthodontic brackets, landmarking the canine on the CBCT had to be approximated, and for some cases, maxillary lateral incisors were used as landmarks instead. Distractions such as metal artefacts may reduce the exactness of the superimposition between the two imaging modalities [20]. The landmark for subnasale also had slightly different locations. On the facial scanner, the soft tissue subnasale point was used, which is the point of convergence of the nose and upper lip, directly beneath the nose. However on the CBCT, the central, most dense area directly under and between the two nasal sinuses was used for landmarking. Since the CBCT subnasale landmark was close to the anterior nasal spine, its measurements were more superior on the face compared to that of the facial scanner. A study conducted by Ayoub et al. [15] which investigated the superimposition of 3D data gathered from a CT scanner and a stereophotogrammetry tool found errors within an acceptable range of ±1.5 mm, with relatively large errors around the eyelid area. It was noted that the eyelid and eyebrow area is subject to surface shape differences when taken via these different imaging modalities, leading to this registration error. Additionally, Hwang et al. [19] stated that some anatomical structures such as the midlateral orbit do not clearly represent the actual anatomical structure of the soft tissues. The findings of both studies agree with the present study, as it was found that measurements containing outer and inner eyes generally had relatively large mean differences. The outer eye landmark on the facial scanner was defined as the most outer sharp part of the eye, and the inner eye landmark was also defined as the most inner sharp part seen on the eye. On the CBCT, the outer eye was defined as the suture between the frontal and zygomatic bones, and the inner eye landmark was located and the suture between the frontal bone and maxilla, near the nasal bone. Since these sutures are more superior on the face than the actual soft tissue outer and inner eye corners, a slightly different mean between the facial scanner and CBCT can be seen; CBCT values are slightly larger, and thus mean difference measurements for left canine to outer eye (−8.55 mm), right canine to outer eye (−7.43 mm), left eye width (−7.49 mm), right eye width (−7.29 mm), left inner eye to canine (−7.25 mm), and right inner eye to canine (−6.81 mm) are negative. As such, these findings indicate that soft- and hard-tissue landmarks of the eye are difficult to reproduce.

Nahm et al. [21] also similarly found the registration relationship between CBCT and facial surfaces to be very close and concluded that merging CBCT and facial scans can produce a much truthful image of the patient to give the orthodontist enhanced diagnostic information and lessen errors in diagnosis. These findings agree with the present study, since it was found that other than some of the few distances mentioned above, many other ratios have excellent soft tissue to CBCT ratio percentages, such as the width between outer eye corners (−0.74%), left (−2.94%) and right (−3.99%) corners of the mouth to EAM, and the nasion to gnathion (−4.38%) measurement. This indicates that the CBCT has a tendency to superimpose very closely to distances of the facial scanner.

Limitations to this study exist which warrant changes to be made for further improvement of this study. Due to the data being collected in a retrospective fashion, there was no method in which head positions for the facial scan and CBCT could have been strictly controlled. Patients were only advised to keep their head in the natural position, with their Frankfort plane parallel to the floor. The result of such minor head position changes of each patient may lead to changes in the position of mobile facial structures, such as the mandible. This will lead to slight changes in landmark positioning of areas such as the gonion, causing a greater difference between the two imaging modalities.

The fact that this study was based off of retrospective data also serves as a limitation in that it limited the sample size. A high-enough sample size is needed based on *a priori* calculations, but such calculations were not performed, since there were only a few patient files within the database that included both facial scans and full field of view CBCTs. Thus, within the small given number of available data to work with, the number 30, was chosen, which was the highest number based on availability of data.

In this study, the gold standard was considered to be the CBCT. This assumption was made based on multiple, high-quality research papers and articles [4, 8–13]. Although it is an educated assumption, this assumption serves as a limitation to this study. In order to improve clinical precision, it

is important to complete real distance measurements on the patient's face and compare them very carefully with both digital methods.

Most measurements have a reasonably small facial scanner to CBCT mean difference. Even if the difference is relatively large, this can be explained by knowing that some landmarks were slightly different in terms of location on the CBCT and facial scanner. Additionally, even if the means and standard deviations may be large, all paired measurements with left and right sides have similar values within at most 2.35 mm from each other, indicating that such measurements are still comparable.

5. Conclusion

The mean soft tissue to CBCT facial distances tend to be within ±20%, with a tendency for the facial scan measurements to be slightly larger than CBCT equivalents. In general, correlation between the facial scan and CBCT tends to be smaller at lateral and mobile areas of the face such as the gonion. Right and left gonions were areas of the face with a high level of difference between landmark sites of the two imaging modalities. There is a general tendency of obtaining less correlation on boney structures as they increase in dimensional size and increase their curvature. Other significant measurement dissimilarities were due to differences in landmark definition between CBCT and facial scan, in areas such as the throat, corners of mouth, and outer/inner eyes. Areas of the face that have a tendency to have high differences between surface shapes, such as the eyelid and eyebrow region, had relatively low correlation between their soft tissues and corresponding hard-tissue landmarks. Some of the limitations of this study, which may lead to lower correlation in some facial landmarks, may include data from a retrospective database, nonspecific head positions of the patient, as well as an indefinite gold standard imaging modality.

Data Availability

The data used to support the findings of this study are available from the corresponding author upon request.

Conflicts of Interest

The authors declare that they have no conflicts of interest.

References

[1] S. Anicy-Milosevicy, M. Lapter-Varga, and M. Slaj, "Analysis of the soft tissue facial profile by means of angular measurements," *European Journal of Orthodontics*, vol. 30, no. 2, pp. 135–140, 2008.

[2] E. G. Kaklamanos and O.-E. Kolokitha, "Relation between soft tissue and skeletal changes after mandibular setback surgery: a systematic review and meta-analysis," *Journal of Cranio-Maxillofacial Surgery*, vol. 44, no. 4, pp. 427–435, 2016.

[3] P. A. Zecca, R. Fastuca, M. Beretta, A. Caprioglio, and A. Macchi, "Correlation assessment between three-dimensional facial soft tissue scan and lateral cephalometric radiography in orthodontic diagnosis," *International Journal of Dentistry*, vol. 2016, Article ID 1473918, 8 pages, 2016.

[4] H. M. Pinsky, S. Dyda, R. W. Pinsky, K. A. Misch, and D. P. Sarment, "Accuracy of three-dimensional measurements using cone-beam CT," *Dentomaxillofacial Radiology*, vol. 35, no. 6, pp. 410–416, 2006.

[5] R. A. Holdaway, "A soft-tissue cephalometric analysis and its use in orthodontic treatment planning. Part I," *American Journal of Orthodontics*, vol. 84, no. 1, pp. 1–28, 1983.

[6] Y.-j. Zhao, Y.-x. Xiong, and Y. Wang, "Three-dimensional accuracy of facial scan for facial deformities in clinics: a new evaluation method for facial scanner accuracy," *PLoS One*, vol. 12, no. 1, Article ID e0169402, 2017.

[7] K. B. Naudi, R. Benramadan, L. Brocklebank, X. Ju, B. Khambay, and A. Ayoub, "The virtual human face: superimposing the simultaneously captured 3D photorealistic skin surface of the face on the untextured skin image of the CBCT scan," *International Journal of Oral and Maxillofacial Surgery*, vol. 42, no. 3, pp. 393–400, 2013.

[8] M. O. Lagravère, J. Carey, R. W. Toogood, and P. W. Major, "Three-dimensional accuracy of measurements made with software on cone-beam computed tomography images," *American Journal of Orthodontics and Dentofacial Orthopedics*, vol. 134, no. 1, pp. 112–116, 2008.

[9] N. Zamora, R. Cibrian, J. Gandia, and V. Paredes, "A new 3D method for measuring cranio-facial relationships with cone beam computed tomography (CBCT)," *Medicina Oral Patología Oral Y Cirugia Bucal*, vol. 18, no. 4, pp. e706–e713, 2013.

[10] C. Lascala, J. Panella, and M. Marques, "Analysis of the accuracy of linear measurements obtained by cone beam computed tomography (CBCT-NewTom)," *Dentomaxillofacial Radiology*, vol. 33, no. 5, pp. 291–294, 2004.

[11] R. Marmulla, R. Wörtche, J. Mühling, and S. Hassfeld, "Geometric accuracy of the NewTom 9000 cone beam CT," *Dentomaxillofacial Radiology*, vol. 34, no. 1, pp. 28–31, 2005.

[12] D. Periago, "Comparative linear accuracy and reliability of cone beam ct derived 2-dimensional and 3-dimensional images constructed using an orthodontic volumetric rendering program," Master's thesis, University of Louisville, Louisville, Kentucky, 2007.

[13] S. Stratemann, J. Huang, K. Maki, A. Miller, and D. Hatcher, "Comparison of cone beam computed tomography imaging with physical measures," *Dentomaxillofacial Radiology*, vol. 37, no. 2, pp. 80–93, 2008.

[14] W. E. Harrell, "3D diagnosis and treatment planning in orthodontics," *Seminars in Orthodontics*, vol. 15, no. 1, pp. 35–41, 2009.

[15] A. F. Ayoub, Y. Xiao, B. Khambay, J. P. Siebert, and D. Hadley, "Towards building a photo-realistic virtual human face for craniomaxillofacial diagnosis and treatment planning," *International Journal of Oral and Maxillofacial Surgery*, vol. 36, no. 5, pp. 423–428, 2007.

[16] A. M. Toma, A. Zhurov, R. Playle, E. Ong, and S. Richmond, "Reproducibility of facial soft tissue landmarks on 3D laser-scanned facial images," *Orthodontics and Craniofacial Research*, vol. 12, no. 1, pp. 33–42, 2009.

[17] S. Baumrind and R. C. Frantz, "The reliability of head film measurements," *American Journal of Orthodontics*, vol. 60, no. 5, pp. 505–517, 1971.

[18] T. J. J. Maal, J. M. Plooij, F. A. Rangel, W. Mollemans, F. A. C. Schutyser, and S. J. Bergé, "The Accuracy of matching three-dimensional photographs with skin surfaces derived from cone-beam computed tomography," *International*

Journal of Oral and Maxillofacial Surgery, vol. 37, no. 7, pp. 641–646, 2008.

[19] H.-S. Hwang, S.-Y. Choe, J.-S. Hwang et al., "Reproducibility of facial soft tissue thickness measurements using cone-beam ct images according to the measurement methods," *Journal of Forensic Sciences*, vol. 60, no. 4, pp. 957–965, 2015.

[20] E. Nkenke, S. Zachow, M. Benz et al., "Fusion of computed tomography data and optical 3d images of the dentition for streak artefact correction in the simulation of orthognathic surgery," *Dentomaxillofacial Radiology*, vol. 33, no. 4, pp. 226–232, 2004.

[21] K.-Y. Nahm, Y. Kim, Y.-S. Choi, J. Lee, S.-H. Kim, and G. Nelson, "Accurate registration of cone-beam computed tomography scans to 3-dimensional facial photographs," *American Journal of Orthodontics and Dentofacial Orthopedics*, vol. 145, no. 2, pp. 256–264, 2014.

Hindawi
International Journal of Dentistry
Volume 2018, Article ID 3761750, 9 pages
https://doi.org/10.1155/2018/3761750

Research Article

Three-Dimensional Accuracy of Digital Impression versus Conventional Method: Effect of Implant Angulation and Connection Type

Marzieh Alikhasi,[1] **Hakime Siadat**,[1] **Alireza Nasirpour**,[2] **and Mahya Hasanzade**[3]

[1]*Dental Research Center, Dentistry Research Institute, Department of Prosthodontics, Tehran University of Medical Sciences, Tehran, Iran*
[2]*Dental Student Research Center, School of Dentistry, Tehran University of Medical Sciences, Tehran, Iran*
[3]*Dental Research Center, Dentistry Research Institute, Department of Prosthodontics, School of Dentistry, Tehran University of Medical Sciences, Tehran, Iran*

Correspondence should be addressed to Mahya Hasanzade; mahya_hasanzade@yahoo.com

Received 12 March 2018; Accepted 9 May 2018; Published 4 June 2018

Academic Editor: Anca M. Vitalariu

Purpose. The aim of this in vitro study was to compare the accuracy of different implant impression techniques of the maxillary full arch with tilted implants of two connection types. *Materials and Methods*. Two maxillary edentulous acrylic resin models with two different implant connections (internal or external) served as a reference model. Each model had two anterior straight and two posterior angulated implants. Ninety impressions were made using an intraoral scanner (Trios 3Shape) with scan bodies for digital impression (groups DII and DIE), a custom open tray with additional silicone for the conventional direct group (groups CDI and CDE), and a custom closed tray with additional silicone for the conventional indirect group (groups CII and CIE) from both internal and external models, respectively. A coordinate-measuring machine (CMM) was used to measure linear and angular displacement for conventional specimens. For digital groups, an optical CMM was used to scan the reference model. STL data sets from the digital specimen were superimposed on STL reference data sets to assess angular and linear deviations. Data were analyzed with three-way ANOVA and *t*-test at $\alpha = 0.05$. *Results*. There were significant angular and linear distortion differences among three impression groups ($P < 0.001$), angular distortion differences between internal and external connections ($P < 0.001$), and between straight and tilted implants for either linear ($P < 0.001$) or angular ($P = 0.002$) distortion. The type of the connection and implant angle did not have any effect on linear and angular distortion of the digital technique ($p > 0.05$). Minimum angular and linear distortion was seen for tilted implants in DII and DIE groups ($0.36^{\circ} \pm 0.37$ and 0.16 ± 0.1 mm). *Conclusion*. Impression techniques (digital versus conventional) affected the transfer accuracy. Digital techniques demonstrated superior outcome in comparison with conventional methods, and the direct technique was better than the indirect conventional technique. Connection type and implant angulation were other factors that influenced accuracy. However, when digital impression was applied, accuracy was not affected by the type of connection and angulation.

1. Introduction

High precision in transfer of clinical conditions to dental laboratory is one of the most important factors in fabrication of the prosthesis with excellent fit for either natural teeth or implants [1]. Therefore, the essential first step for fabrication of a successful implant-supported prosthesis is accurate transfer of three-dimensional implant position and angulation from the mouth to the master cast via impression [1, 2]. Inaccurate position of the implant in the master cast makes it impossible to fabricate a well-fitting prosthesis, and the resultant misfit can lead to biomechanical complications such as screw loosening [3], bone loss [4], and ceramic veneer fracture as a result of increasing stress within the prosthesis or at the interface of the implant and bone. Accuracy of the master cast is influenced by several factors including the impression

technique, type of the tray [5, 6], manipulation of the dental stone, and its compatibility with the impression material [7]. Each step could have a potential error related to inherent materials or humans which is inevitable. Moreover, other factors involved in the precision of implant impression could be the impression technique (direct versus indirect), splinting, machining tolerance of components, number and angle of implants, depth of implants, and type of connection [8–14]. Multiple implants with different angulations can cause distortion of the impression material on removal [11]. In a review by Lee et al. [15], it has been reported that when the implants are more than three, angulation of implants may affect the accuracy. However, when the implants are limited to 2 or 3, no effect was reported on the impression accuracy [10]. Also, many articles studied the accuracy of different implant impression techniques [16–20]. For situations in which there were 4 or more implants, studies showed more accurate impressions with the direct technique than the transfer technique [8, 15, 18, 19].

The advent of intraoral scanners (IOSs) has led to a change in implant dentistry. Although the first IOSs became commercially available two decades ago, their popularity in recent years has grown dramatically, which results from an increase in precision and efficiency [21]. Digital impression can improve patient acceptance [22], reduce possible distortion of impression materials and master casts [11], reduce chairside time [22], and provide a 3D image of preparation. Although some articles reported distortion and lower accuracy for digital impression [5, 17], there is also some defensive evidence that shows digital impression comparable to or even better than conventional impression [16, 21, 23, 24]. Therefore, there is disagreement towards the priority of these methods.

Fabrication of the prosthesis with CAD/CAM has many steps including acquisition of data by scanning, processing the information, designing the restoration, and eventually manufacturing. All of these steps have some potential errors which are displayed in the final restoration as the amount of misfit. As different factors influence the accuracy of each step, breaking up of the errors of different steps is important. Several studies have compared fitness of final restoration fabricated with CAD/CAM or conventional methods [12, 25–28] although there is not enough knowledge of the accuracy of intraoral digital impression systems for dental implants [11, 29].

The aim of the current study was to compare the accuracy of conventional (direct and indirect) and intraoral digital impressions of the maxillary full arch with tilted implants of two connection types. The null hypothesis was that there was no difference between digital and conventional techniques, and also, implant angulation and connection type would not affect the accuracy.

2. Materials and Methods

This in vitro experimental study was conducted on two edentulous maxillary acrylic resin models with two different implant connections (internal trilobe and external hexagon). In each resin model, the two anterior implants were placed straight at the site of canine teeth with no angulation and parallel to each other (their longitudinal axis was perpendicular to the plane of the resin model). Implants were numbered from 1 to 4 from the posterior right to the posterior left (implants 1 and 4 were angulated and 2 and 3 had straight position). The two posterior implants were placed at the site of the second premolars with 45° distal angulations. The NobelReplace implant system (Nobel Biocare AB, Göteborg, Sweden) was used in one acrylic resin model with a regular diameter (4.3 mm), 11 mm height, and internal trilobe connection. The Branemark Nobel Biocare implant system (Brånemark System® Mk III, Nobel Biocare AB) with a regular diameter (4.1 mm), 12 mm height, and external hexagon connection was used in the second acrylic resin model. A metal reference cylinder was inserted in the midline of the palate in the model as a reference of measurement and was defined as the zero point [13].

Table 1: Definition of groups.

Impression method	Connection type	Group	Number
Digital	Internal	DII	15
	External	DIE	15
Conventional direct	Internal	CDI	15
	External	CDE	15
Conventional indirect	Internal	CII	15
	External	CIE	15

Description of the groups is presented in Table 1. After 24 hours, the conical impression copings of both systems (Nobel Biocare AB, Göteborg, Sweden) were fastened to the implants, the baseplate wax (Modeling wax; Dentsply DeTrey, Konstanz, Germany) was adapted around and over the impression coping, and irreversible hydrocolloid (Alginoplast; Heraeus Kulzer GmbH &Co., Wehrheim, Germany) impressions were made to obtain two casts. These casts were used to mold custom trays. The obtained casts were covered by two layers of the baseplate wax (Modeling wax; Dentsply DeTrey, Konstanz, Germany) to allow a reliable thickness of the impression material. Tissue stops were included in the impression trays to standardize tray positioning during impression making. Sixty 2 mm thick custom impression trays (30 open trays and 30 closed trays) were made with light polymerizing resin (Megatray; Megadenta, Radeberg, Germany). Each tray was perforated, and the internal part and 5 mm outside of the borders were coated with an adhesive 30 minutes before each impression was made. Addition silicone (Zhermack Elite HD + Regular Body, Kouigo, Italy) was the impression material of choice for all transfer procedures and was managed according to manufacturers' recommendations and the specification number 19 of ADA. All impressions were made in a temperature-controlled environment ($23 \pm 1^{\circ}$C) with a relative humidity of $50 \pm 10\%$ [13].

Square copings in groups CDI and CDE and conical copings in groups CII and CIE were adapted to the implants. All impression copings were secured with a torque wrench calibrated at 10 Ncm torque on the implants. An automixing cartridge was used for mixing the impression material. For each impression, 12 mL of the material was carefully injected

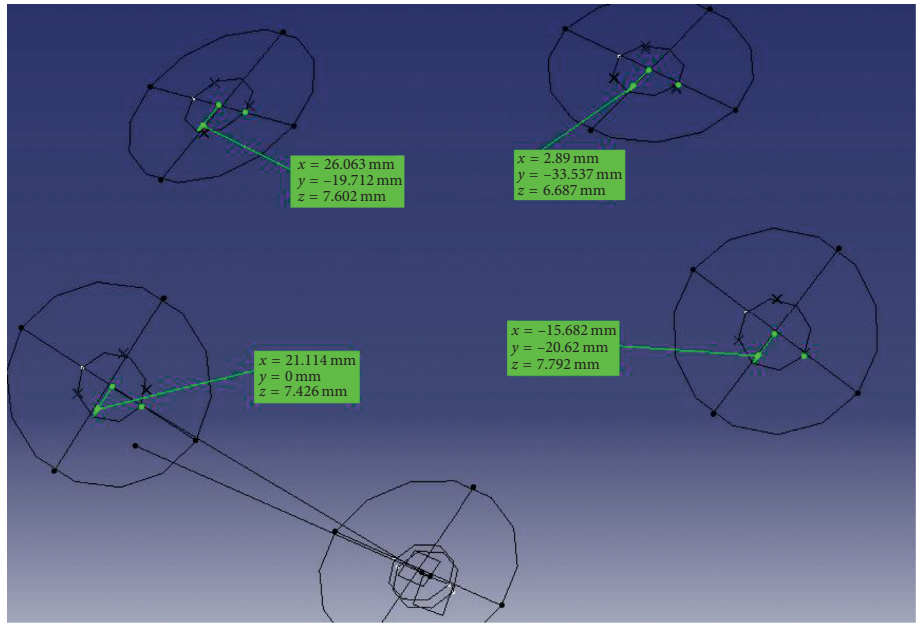

Figure 1: Schematic drawing of the measurements according to the reference point.

around and over the copings to ensure complete coverage of the copings. 35 mL of the remaining impression material was used to fill the impression special tray. To standardize the seating load for each impression, a 5 kg weight was placed over the trays during material polymerization. The impression materials were allowed to polymerize for 12 minutes after the start of the procedure according to the manufacturer's recommendation. The impression/matrix set was placed in distilled water at 36 ± 1°C during the setting time.

Once the impression had been obtained, implant analogues were adapted and screwed into the pick-up impression copings. In groups CII and CIE, the impression/matrix set was separated. Then, the conical transfer impression copings were unscrewed from the matrix and fitted to the implant analogues, and they were immediately replaced in each respective notch left in the impression. The combined impression coping analogue unit was inserted into the impression by firmly pushing it into place to full depth and slightly rotating it clockwise to feel the antirotational resistance. Casts were made by pouring type IV dental stone (Herostonel Vigodent Inc., Rio de Janeiro, RJ, Brazil), which was vacuum mixed with a powder/water ratio of 30 g/7 mL, as recommended by the manufacturer's instructions. When set (120 minutes after pouring), the impression was separated from the cast. The same operators prepared all sixty impressions in all clinical and laboratory procedures [13].

For making digital impression, Trios 3Shape (3Shape, Copenhagen, Denmark) IOS was used. Scan bodies for internal (14.005; DESS Abutments Co., Barcelona, Spain) and external (14.002; DESS Abutments Co., Barcelona, Spain) connections were torqued 10 Ncm to the NobelReplace and Branemark Nobel Biocare implants, respectively. Fifteen scans of the models were done by one experienced operator of each model. After calibrating and scanning by the operator, the best method selected was starting scan from the reference pin in the palate of the model towards the right tuberosity and lingual surfaces of all scan bodies. Next, the buccal surfaces and then the occlusal surfaces of scan bodies were scanned. Care was taken to well record the connection area and smooth surface at the distance between scan bodies. Intraoral scanning data were transferred to Dental System software and converted from 3OXZ format to STL format.

2.1. Measurements. A single calibrated blinded examiner performed all readings randomly without any notification of previously described information about the code of each stone cast. The coordinate-measuring machine (CMM) (Mistral, DEA Brown&Sharpe, Grugliasco, Italy) was used for recording the x-, y-, and z-dimensions and also angular dislocation simultaneously. Each working cast was measured three times, and an average was obtained. Additionally, readings were obtained in each of four implants of the groups. These linear and angular measurements performed on the master models were repeated for all study casts. To represent three-dimensional linear displacement, Δr was calculated using $\Delta r^2 = \Delta x^2 + \Delta y^2 + \Delta z^2$, where Δx, Δy, and Δz were displacements at x-, y-, and z-directions, respectively (Figure 1) [13].

For digital models, reference models were scanned by an optical coordinate-measuring machine (ATOS Core 80; GOM GmbH, Germany). The data from this scanner were transferred to GOM Inspect software (GOM GmbH, Germany) in STL format and were set as a nominal element. The output data in STL format of intraoral scans were also transferred to GOM Inspect software as actual elements, and comparison with nominal values was made. Measurements were made by one experienced operator. For the measurements, first, the best-fitted plane to the occlusal surface of the reference pin and the scan bodies in each reference model were defined in the software, and then, a cylinder with the best fit to the external surface of each scan body was

designed. The central axis of each cylinder was determined, and its intersection with the occlusal plane was marked (Figure 2(a)). The same definitions for the plane, cylinder, axis of each cylinder, and its intersection with the occlusal plane were used in the scanned model by Trios 3Shape and also for the reference pin in the palate. Then, the best-fit alignment was used for superimposition of scans obtained from Trios 3Shape on the corresponding images obtained from ATOS Core (Figure 2(b)). To determine the change in implant position, the distance between the intersection point of the central axis of the cylinder with the occlusal plane on the surface of the scan body and the central index was recorded. The reported deviation was the distance of the measured data point from the surface of the nominal (CAD) model to the actual model surface at that point location (Figure 2(c)). The software measured the values in three spatial planes of *XY*, *XZ*, and *YZ*. To determine the change in angular position of each scan body, the change in the angle of the cylinder axis of each scan body with the corresponding axis on the nominal model was calculated in degrees. All measurements were made automatically by the software.

2.2. Statistical Analysis. The sample size was calculated for 80% power, using PASS Sample Size Software version 11. Data were analyzed using SPSS version 23 (SPSS Inc., IL, USA). The mean and standard deviation values were reported for dependent variables including ΔR and ΔA. Considering the presence of three independent variables (impression method, implant connection, and implant angulation), three-way ANOVA was applied. Since the interaction effect of some independent variables was found to be significant, pairwise comparisons were done with post hoc Tukey and independent *t*-tests. The level of significance was set at 0.05.

3. Results

The mean and SD of the linear and angular distortion of six groups and subgroups are presented in Table 2. Three-way ANOVA showed a statistically significant difference among three impression techniques ($P < 0.001$), between internal and external connections regarding angular distortion ($P < 0.001$), between straight and tilted implants for either linear ($P < 0.001$) or angular ($P = 0.002$) distortion, and their mutual interaction ($P < 0.001$). Minimum angular and linear distortion was seen for tilted implants in DII and DIE groups, respectively ($0.36^{\circ} \pm 0.37$ and 0.16 ± 0.1 mm). The maximum value of angular distortion was for tilted implants in the CII group ($9.37^{\circ} \pm 6.9$ mm), and straight implants in the CII group had maximum linear distortion (0.88 ± 0.38 mm).

3.1. Impression Method. The effect of the impression technique by comparing inaccuracy values for each group at the implant angulation and connection type is shown in Table 3. There was a significant difference of angular distortion (ΔA) among three impression groups ($P < 0.001$); The DII group produced better results than conventional direct and indirect techniques with either straight ($P < 0.001$) or tilted ($P < 0.001$) implants. The DIE group was more accurate than the CIE group both for straight ($P < 0.001$) and tilted ($P < 0.001$) implants. The DIE group showed more accurate values than the CDE group only for tilted implants ($P < 0.001$). Comparing direct and indirect methods, results showed that the direct technique (CDI and CDE groups) was more accurate than the indirect method (CII ($P < 0.001$) and CIE ($P < 0.001$)).

Linear distortion (Δr), when external connection was used regardless of being straight or tilted digital technique, was better than both conventional direct ($P < 0.001$) and indirect ($P < 0.001$) methods. However, when the connection was internal, the DII group was more accurate than the CII group ($P < 0.001$) and the CDI group was better than the CII group ($P < 0.001$). There was no significant difference between digital (DII) and direct (CDI) techniques in straight implants.

3.2. Connection Type. The effect of the connection type was analyzed by comparing angular and linear distortion for each group with the impression technique and angulation of the implant as variables, and the results are demonstrated in Table 4. The results showed that there was no significant difference between internal and external connections of digital groups (DII and DIE). In conventional direct groups (CDI and CDE), the external connection was better than the internal connection in angular distortion both for tilted ($P < 0.001$) and straight ($P < 0.001$) implants. With the indirect impression technique (CII and CIE groups), the connection type did not have any effect on the accuracy of straight implant transfer, although for tilted implants, external connections showed better results of ΔA ($P < 0.001$) and Δr ($P = 0.001$).

3.3. Implant Angle. The effect of the implant angle was analyzed in the same way, and the results are shown in Table 5. There was no significant difference between angled and straight implants for the digital technique (DII and DIE groups). In the CDI group, straight implants were better than tilted implants regarding ΔA ($P < 0.001$) and Δr ($P = 0.03$). However, in the CIE group, tilted implants showed less Δr ($P < 0.001$) and ΔA ($P < 0.001$) distortion.

4. Discussion

A precise impression of implants in an edentulous jaw is a prerequisite of an accurate master cast which is necessary for fabricating a well-fitting prosthesis [2]. The use of IOS is overgrowing; however, there is not enough evidence about the accuracy of it in comparison with the conventional method [8, 30]. The current study compares both the linear and angular distortion among three different impression methods (digital impression with 3Shape IOS, the conventional direct impression technique, and the conventional indirect impression technique), types of connections, and angulations of implants.

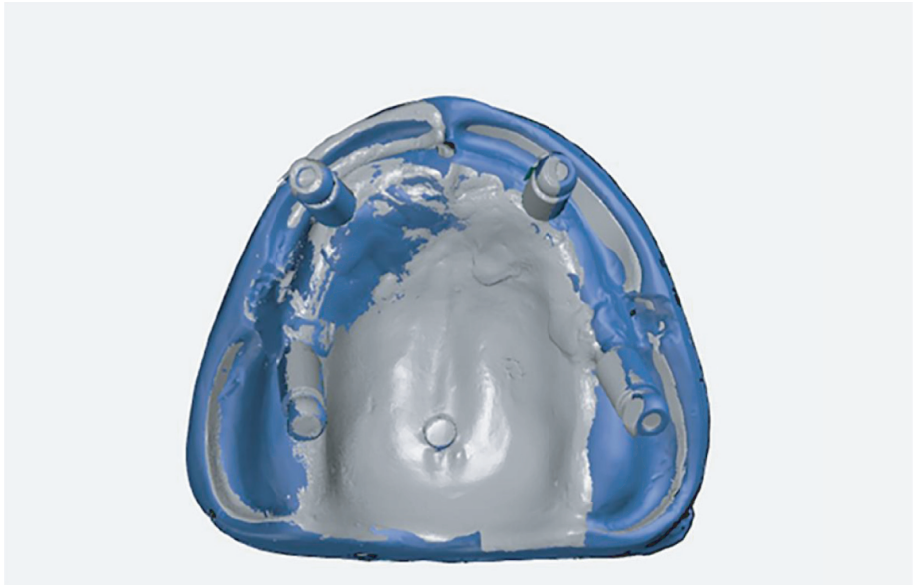

(a)

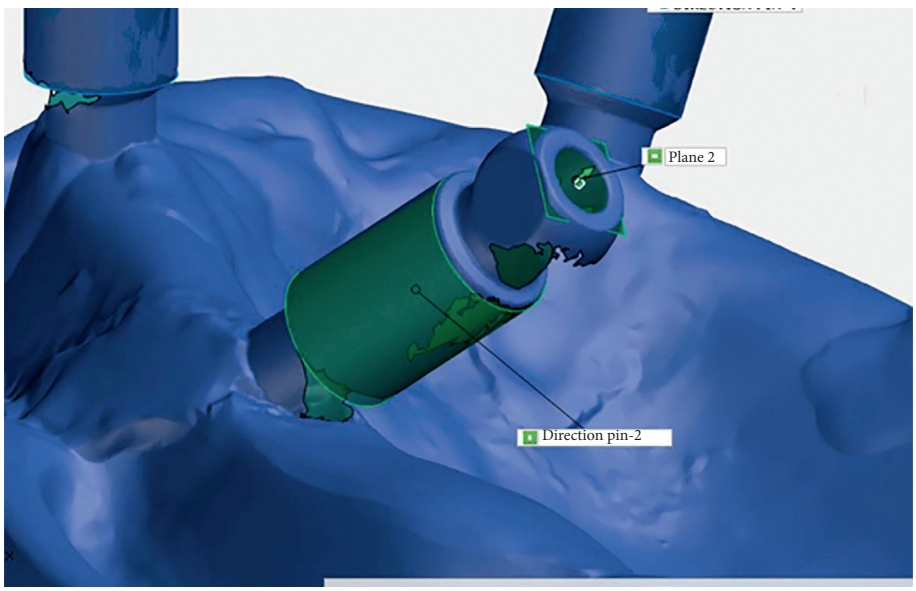

(b)

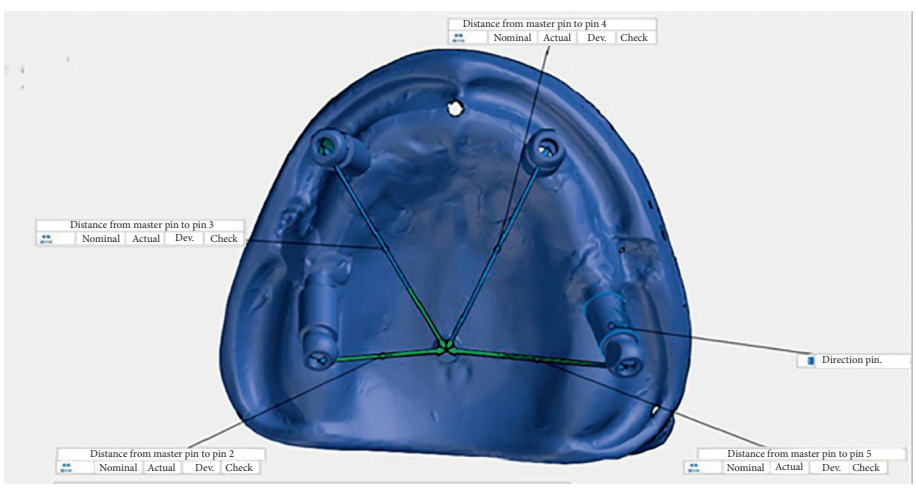

(c)

Figure 2: Digital impression measurements. (a) Superimposition of nominal and actual data. (b) Fitting plane and cylinder and intersecting point (green) which indicates implant position. (c) Linear measurements.

Table 2: Mean and SD values of three groups.

Group	Implant angulation	Linear distortion		Angular distortion	
		Mean (mm)	SD	Mean (degree)	SD
DII	Straight	0.188	0.134	0.585	0.724
	Tilted	0.162	0.103	0.364	0.374
DIE	Straight	0.195	0.158	0.587	0.724
	Tilted	0.165	0.134	0.366	0.377
CDI	Straight	0.280	0.142	2.287	1.325
	Tilted	0.389	0.228	4.765	2.203
CDE	Straight	0.711	0.286	1.004	0.453
	Tilted	0.364	0.231	1.098	0.381
CII	Straight	0.885	0.389	4.096	2.726
	Tilted	0.721	0.384	9.371	6.900
CIE	Straight	0.797	0.351	4.851	1.459
	Tilted	0.442	0.226	2.062	0.968

Table 3: The effect of the impression technique by comparing inaccuracy values for each group at the implant angulation and connection type.

Impression technique	Internal				External			
	Tilted		Straight		Tilted		Straight	
	Δr P value	ΔA P value	Δr P value	ΔA P value	Δr P value	ΔA P value	Δr P value	ΔA P value
Digital versus closed	0.000	0.000	0.000	0.000	0.000	0.000	0.000	0.000
Digital versus open	0.004	0.000	0.35	0.001	0.001	0.000	0.000	0.228
Open versus closed	0.000	0.000	0.000	0.001	0.229	0.000	0.450	0.000

Table 4: The effect of the connection type by comparing inaccuracy values for each group at the implant angulation and impression technique.

Impression method	Angulation	Connection type	Group	Δr P value	ΔA P value
Digital	Straight	Internal	DII	0.859	0.992
		External	DIE		
	Tilted	Internal	DII	0.916	0.989
		External	DIE		
Conventional direct	Straight	Internal	CDI	0.000$^{\times}$	0.000$^{\times}$
		External	CDE		
	Tilted	Internal	CDI	0.762	0.000$^{\times}$
		External	CDE		
Conventional indirect	Straight	Internal	CII	0.364	0.188
		External	CIE		
	Tilted	Internal	CII	0.001$^{\times}$	0.000$^{\times}$
		External	CIE		

$^{\times}P$ value is significant (<0.05).

The null hypothesis was rejected as results demonstrated that digital impression has significantly less angular and linear distortion than conventional methods. However, digital impression of straight implants with internal connection was more accurate than that of the direct technique although the difference was not significant. These results verified findings of other studies which show that the impression technique could affect the transfer accuracy [16, 23]. A study by Amin et al. compared the accuracy of digital implant impressions using CEREC Omnicam and 3M True Definition versus conventional impression techniques for a five-implant full-arch edentulous mandible [16]. The authors reported that digital implant impressions were more accurate than conventional direct splinted implant-level impressions. Another in vitro study by Papaspyridakos et al. compared the accuracy of digital implant impression using the 3Shape scanner with the conventional method and showed that the accuracy of digital impression was comparable to that of the conventional method [23]. Digital impressions of five mandibular implants resulted in similar accuracy to the splinted implant-level impressions, and both techniques were superior to the nonsplinted, implant-level impression technique [23]. The result of this study is somehow in contrast with our study that can be related to factors such as the impression material, impression technique, expansion of stone, pouring stone technique, and machine tolerance of the prosthetic component. Moreover, different scan bodies of two studies could be an additional factor for contrary results.

Table 5: The effect of implant angulation by comparing inaccuracy values for each group at the connection type and impression technique.

Impression method		Angulation	Group	Δr P value	ΔA P value
Digital	Internal	Straight Tilted	DII	0.401	0.144
	External	Straight Tilted	DIE	0.433	0.144
Conventional direct	Internal	Straight Tilted	CDI	0.030$^{\times}$	0.000$^{\times}$
	External	Straight Tilted	CDE	0.000$^{\times}$	0.390
Conventional indirect	Internal	Straight Tilted	CII	0.106	0.000$^{\times}$
	External	Straight Tilted	CIE	0.000$^{\times}$	0.000$^{\times}$

$^{\times}P$ value is significant (<0.05).

Differences in the method for accuracy measurement is another contributing factor. In this study, the CMM was used for scanning casts from conventional impression to use that data set file as the comparative value with data from digital impression. However, Papaspyridakos et al. [23] scanned all stone casts with a 6 μ precision scanner (IScan D103i; Imetric), and data in the STL format were used to be compared with data from digital impression. Moreover, one of the implants was used as a reference for superimposition of the scans while using an unstable reference for superimposition is not a reliable technique.

Other factors that could influence the accuracy of impressions are implant angulation and connection type although evidence is insufficient in this field [8]. The results of the current study showed that when angulation was increased up to 45 degrees, accuracy was not affected in digital (DII and DIE) groups. Logically, accuracy of digital impression should not be affected by the angulation of implants as the concern of impression material deformation during removal, or displacement of impression coping is not an issue in this technique. In the conventional direct group, results vary depending on the connection type; In the CDI group, straight implants were better than tilted implants, but surprisingly, in the CDE group, tilted implants had less linear distortion than straight implants. Also, in the CIE group, tilted implants showed better accuracy than straight implants which can be explained by the fact that, in conventional impressions, the operator may remove the tray unexpectedly in direction of the tilted implant to prevent distortion.

In contrast to our result, Lin et al. reported that the divergence between the two implants (0, 15, 30, and 45 degrees) did not affect the accuracy of the definitive cast created through traditional impression, but the divergence between the two implants significantly affected the accuracy of the milled cast through digital impression [31]. They found that, at lower levels of divergence (0 to 15 degrees), conventional impression was more accurate than digital impressions. However, at a higher divergence (30 to 45 degrees), the differences in accuracy between conventional and digital impressions became less noticeable, with conventional impression still being slightly more accurate. The source of these contradictory results may be using different scanners and software (Cadent iTero) and different scan bodies (Straumann). Moreover, in the Lin et al. [31] study, milled polyurethane casts were fabricated from digital data, and implant analogues were inserted manually which can be a source of error. Chia et al. reported that, in the presence of angulated implants, there is a little difference between the digital impression and conventional technique [10]. Direct comparison between the results of our study and Chia et al. [10] should be done with caution, as the model in that study was partially edentulous and was restricted to two implants and the most angled specimen had 20-degree angulation although in our study, it was 45 degrees. A clinical study showed that digital impression for the all-on-four system with two straight and two tilted implants resulted in accurate physical models and improved efficiencies for the dental team [32].

The type of connection can affect the stability of the implant-prosthesis interface [12]. The Branemark system was characterized by external hexagon connection; this configuration has some weakness because of limited height; it is not efficient when the off-axis load is applied to resist micromovements [33]. However, this configuration may become a privilege during impression as it allows easier removal of the tray. In internal connection, the impression coping has an intimate fit within the implant which may make removal of the impression more difficult and may generate a higher degree of distortion. Based on the results of the current study in the conventional impression group, external connection implants showed less distortion than the internal one. As in digital impression, removing the impression is not an issue, and the type of connection does not influence the accuracy. In confirmation with our result, Papaspyridakos et al. [12, 23] reported that the type of connection influenced the accuracy at implant-level impression.

Different IOSs were used in studies, and it has been shown that the accuracy of scanners differs from each other, either for tooth or implant impression [26, 34]. In a study by Vandeweghe et al. [35], four different IOSs were used to get the impression of an edentulous model of the mandible with six implants (Lava COS, 3M, CEREC Ominicam, and Trios 3Shape). Based on the results of this study, the 3M True

Definition and Trios scanner demonstrated the highest accuracy. However, the Lava COS was found to be not suitable for taking implant impressions for a cross-arch bridge in the edentulous jaw. This study did not have any conventional group as a control. In our study, Trios scanner had been used which uses the confocal optical imaging technology to generate digital point cloud surfaces.

Regarding the methodology of accuracy measurement, several methods have been employed including the coordinate-measuring machine, traveling microscope, computerized tomography, and optical scanning and digitization. Using digital scanners and the corresponding software represents an efficient method [5]. An industrial metrology 3D scanner (ATOS) with a precision of 4 microns was used in our study. Using the "best-fit algorithm" for superimposing the point cloud is a reliable technique [36].

A limitation of this study is lack of a gauge block for precisely defining the direction of *x*-, *y*-, and *z*-axes though the cylindrical index at the middle of the palate which can play somehow the same role. Moreover, measuring the accuracy of conventional impression and digital impression with two different methods could result in some error related to different precisions of each method. Correlating findings of this in vitro study to clinical situation should be done with caution as there are contributing factors in the oral environment including tissue undercuts, saliva, and limited access during scanning and restricted direction for tray removal.

5. Conclusion

With the limitations of this study, the following can be concluded:

(1) Digital impression is better than the direct technique in the edentulous arch with straight and tilted implants, and both of them are more accurate than the indirect technique.

(2) Type of connection does not have any effect on accuracy when a digital workflow was applied.

(3) Precision of implant position also is not affected by the angulation of implants in the digital impression group.

Data Availability

The data used to support the findings of this study were supplied by Marzieh Alikhasi under license and so cannot be made freely available. Requests for access to these data should be made to Marzieh Alikhasi (m_alikhasi@yahoo.com).

Conflicts of Interest

The authors declare that they have no conflicts of interest.

Acknowledgments

The authors wish to thank Fadak Sanat Company for their cooperation in scanning with ATOS Core 80, GOM. This study was funded and supported by the Dental Research Center, Dentistry Research Institute, Tehran University of Medical Sciences under Grant no. 94-03-104-29757.

References

[1] A. G. Wee, S. A. Aquilino, and R. L. Schneider, "Strategies to achieve fit in implant prosthodontics: a review of the literature," *International Journal of Prosthodontics*, vol. 12, no. 2, pp. 167–178, 1999.

[2] M. Karl, W. Winter, T. D. Taylor, and S. M. Heckmann, "In vitro study on passive fit in implant-supported 5-unit fixed partial dentures," *International Journal of Oral and Maxillofacial Implants*, vol. 19, no. 1, pp. 30–37, 2004.

[3] L. E. E. Al-Turki, J. Chai, E. P. Lautenschlager, and M. C. Hutten, "Changes in prosthetic screw stability because of misfit of implant-supported prostheses," *International Journal of Prosthodontics*, vol. 15, no. 1, 2002.

[4] T. Jemt and K. Book, "Prosthesis misfit and marginal bone loss in edentulous implant patients," *International Journal of Oral and Maxillofacial Implants*, vol. 11, no. 5, pp. 620–625, 1996.

[5] A. Ender and A. Mehl, "Accuracy of complete-arch dental impressions: a new method of measuring trueness and precision," *Journal of Prosthetic Dentistry*, vol. 109, no. 2, pp. 121–128, 2013.

[6] M. E. Brosky, I. J. Pesun, P. D. Lowder, R. DeLong, and J. S. Hodges, "Laser digitization of casts to determine the effect of tray selection and cast formation technique on accuracy," *Journal of Prosthetic Dentistry*, vol. 87, no. 2, pp. 204–209, 2002.

[7] B. Wöstmann, P. Rehmann, and M. Balkenhol, "Influence of impression technique and material on the accuracy of multiple implant impressions," *International Journal of Prosthodontics*, vol. 21, no. 4, pp. 299–301, 2008.

[8] P. Papaspyridakos, C.-J. Chen, G. O. Gallucci, A. Doukoudakis, H.-P. Weber, and V. Chronopoulos, "Accuracy of implant impressions for partially and completely edentulous patients: a systematic review," *International Journal of Oral and Maxillofacial Implants*, vol. 29, no. 4, pp. 836–845, 2014.

[9] K. Al-Abdullah, R. Zandparsa, M. Finkelman, and H. Hirayama, "An in vitro comparison of the accuracy of implant impressions with coded healing abutments and different implant angulations," *Journal of Prosthetic Dentistry*, vol. 110, no. 2, pp. 90–100, 2013.

[10] V. A. Chia, R. J. Esguerra, K. H. Teoh, J. W. Teo, K. M. Wong, and T. B. Tan, "In vitro three-dimensional accuracy of digital implant impressions: the effect of implant angulation," *International Journal of Oral and Maxillofacial Implants*, vol. 32, no. 2, pp. 313–321, 2017.

[11] B. Giménez, M. Özcan, F. Martínez-Rus, and G. Pradíes, "Accuracy of a digital impression system based on active wavefront sampling technology for implants considering operator experience, implant angulation, and depth," *Clinical Implant Dentistry and Related Research*, vol. 17, no. S1, pp. e54–e64, 2015.

[12] P. Papaspyridakos, H. Hirayama, C. J. Chen, C. H. Ho, V. Chronopoulos, and H. P. Weber, "Full-arch implant fixed prostheses: a comparative study on the effect of connection type and impression technique on accuracy of fit," *Clinical Oral Implants Research*, vol. 27, no. 9, pp. 1099–1105, 2016.

[13] M. Alikhasi, H. Siadat, and S. Rahimian, "The effect of implant angulation on the transfer accuracy of external-connection

implants," *Clinical Implant Dentistry and Related Research*, vol. 17, no. 4, pp. 822–829, 2015.

[14] E. Beyabanaki, A. R. Shamshiri, M. Alikhasi, and A. Monzavi, "Effect of splinting on dimensional accuracy of impressions made of implants with different subgingival alignments," *Journal of Prosthodontics*, vol. 26, no. 1, pp. 48–55, 2015.

[15] H. Lee, J. S. So, J. Hochstedler, and C. Ercoli, "The accuracy of implant impressions: a systematic review," *Journal of Prosthetic Dentistry*, vol. 100, no. 4, pp. 285–291, 2008.

[16] S. Amin, H. P. Weber, M. Finkelman, K. El Rafie, Y. Kudara, and P. Papaspyridakos, "Digital vs. conventional full-arch implant impressions: a comparative study," *Clinical Oral Implants Research*, vol. 28, no. 11, pp. 1360–1367, 2016.

[17] K. Basaki, H. Alkumru, G. De Souza, and Y. Finer, "Accuracy of digital vs. conventional implant impression approach: a three-dimensional comparative in vitro analysis," *International Journal of Oral and Maxillofacial Implants*, vol. 32, no. 4, pp. 792–799, 2017.

[18] M. Stimmelmayr, J.-F. Güth, K. Erdelt, A. Happe, M. Schlee, and F. Beuer, "Clinical study evaluating the discrepancy of two different impression techniques of four implants in an edentulous jaw," *Clinical Oral Investigations*, vol. 17, no. 8, pp. 1929–1935, 2013.

[19] F. Martínez-Rus, C. García, A. Santamaría, M. Özcan, and G. Pradíes, "Accuracy of definitive casts using 4 implant-level impression techniques in a scenario of multi-implant system with different implant angulations and subgingival alignment levels," *Implant Dentistry*, vol. 22, no. 3, pp. 268–276, 2013.

[20] F. A. Al Quran, B. A. Rashdan, A. A. Abu Zomar, and S. Weiner, "Passive fit and accuracy of three dental implant impression techniques," *Quintessence International*, vol. 43, no. 2, pp. 119–125, 2012.

[21] F. S. Andriessen, D. R. Rijkens, W. J. van der Meer, and D. W. Wismeijer, "Applicability and accuracy of an intraoral scanner for scanning multiple implants in edentulous mandibles: a pilot study," *Journal of Prosthetic Dentistry*, vol. 111, no. 3, pp. 186–194, 2014.

[22] T. Joda and U. Brägger, "Patient-centered outcomes comparing digital and conventional implant impression procedures: a randomized crossover trial," *Clinical Oral Implants Research*, vol. 27, no. 12, pp. e185–e189, 2016.

[23] P. Papaspyridakos, G. O. Gallucci, C. J. Chen, S. Hanssen, I. Naert, and B. Vandenberghe, "Digital versus conventional implant impressions for edentulous patients: accuracy outcomes," *Clinical Oral Implants Research*, vol. 27, no. 4, pp. 465–472, 2016.

[24] E. Gherlone, P. Capparé, R. Vinci, F. Ferrini, G. Gastaldi, and R. Crespi, "Conventional versus digital impressions for "all-on-four" restorations," *International Journal of Oral and Maxillofacial Implants*, vol. 31, no. 2, pp. 324–330, 2016.

[25] T. Abdel-Azim, K. Rogers, E. Elathamna, A. Zandinejad, M. Metz, and D. Morton, "Comparison of the marginal fit of lithium disilicate crowns fabricated with CAD/CAM technology by using conventional impressions and two intraoral digital scanners," *Journal of Prosthetic Dentistry*, vol. 114, no. 4, pp. 554–559, 2015.

[26] H. Kocaağaoğlu, H. I. Kılınç, and H. Albayrak, "Effect of digital impressions and production protocols on the adaptation of zirconia copings," *Journal of Prosthetic Dentistry*, vol. 117, no. 1, pp. 102–108, 2017.

[27] P. Seelbach, C. Brueckel, and B. Wöstmann, "Accuracy of digital and conventional impression techniques and workflow," *Clinical Oral Investigations*, vol. 17, no. 7, pp. 1759–1764, 2012.

[28] A.-M. Hadi, B. Yilmaz, E. McGlumphy, W. A. Brantley, and W. M. Johnston, "Distortion of CAD-CAM-fabricated implant-fixed titanium and zirconia complete dental prosthesis frameworks," *Journal of Prosthetic Dentistry*, vol. 119, no. 1, pp. 116–123, 2017.

[29] A. K. Garg, "Cadent iTero's digital system for dental impressions: the end of trays and putty?," *Dental Implantology Update*, vol. 19, no. 1, pp. 1–4, 2008.

[30] G. J. Christensen, "Impressions are changing: deciding on conventional, digital or digital plus in-office milling," *Journal of the American Dental Association*, vol. 140, no. 10, pp. 1301–1304, 2009.

[31] W.-S. Lin, B. T. Harris, E. N. Elathamna, T. Abdel-Azim, and D. Morton, "Effect of implant divergence on the accuracy of definitive casts created from traditional and digital implant-level impressions: an in vitro comparative study," *International Journal of Oral and Maxillofacial Implants*, vol. 30, no. 1, pp. 102–109, 2015.

[32] E. F. Gherlone, F. Ferrini, R. Crespi, G. Gastaldi, and P. Capparé, "Digital impressions for fabrication of definitive "all-on-four" restorations," *Implant Dentistry*, vol. 24, no. 1, pp. 125–129, 2015.

[33] L. A. Weinberg, "The biomechanics of force distribution in implant-supported prostheses," *International Journal of Oral and Maxillofacial Implants*, vol. 8, no. 1, pp. 19–31, 1993.

[34] S. B. Patzelt, A. Emmanouilidi, S. Stampf, J. R. Strub, and W. Att, "Accuracy of full-arch scans using intraoral scanners," *Clinical Oral Investigations*, vol. 18, no. 6, pp. 1687–1694, 2013.

[35] S. Vandeweghe, V. Vervack, M. Dierens, and H. De Bruyn, "Accuracy of digital impressions of multiple dental implants: an in vitro study," *Clinical Oral Implants Research*, vol. 28, no. 6, pp. 648–653, 2017.

[36] J.-F. Güth, C. Keul, M. Stimmelmayr, F. Beuer, and D. Edelhoff, "Accuracy of digital models obtained by direct and indirect data capturing," *Clinical Oral Investigations*, vol. 17, no. 4, pp. 1201–1208, 2013.